SOLUBILITY PHASE TRANSITION BEHAVIOR OF GOLD NANOPARTICLES IN COLLOIDAL SOLUTION

by

HAO YAN

B.S., Nanjing University, 1995
M.S., Peking University, 2001

AN ABSTRACT OF A DISSERTATION

submitted in partial fulfillment of the requirements for the degree

DOCTOR OF PHILOSOPHY

Department of Physics
College of Arts and Sciences

KANSAS STATE UNIVERSITY
Manhattan, Kansas

2009

Abstract

Nano-size materials are new materials in an intermediate state between the bulk and atomic or molecular states. Nanoparticles in colloidal solution and their assemblies have the great attention of researchers to investigate the novel fundamental properties and numerous applications. In this dissertation, we investigated the solubility phase transition behavior of gold nanoparticles in colloidal solution.

We used the nearly monodisperse gold nanoparticles synthesized by either the inverse micelle or the solvated metal atom dispersion methods followed by digestive ripening. The gold nanoparticles were ligated with alkyl chains, which were dodecanethiol, decanethiol, or octanethiol for individual samples. They dispersed in toluene or t-butyl toluene like large molecules at room temperature. In analogy to molecular solutions, the colloidal solution had thermally reversible phase transitions between a dissolved phase of dispersed single nanoparticles and dispersed-aggregation co-existing phase. A more polar solvent, 2-butanone, was added to the colloidal solution for changing the solubility of gold nanoparticles and adjusting the phase transition temperatures to accessible temperatures. Superclusters formed by the nanoparticles when the colloidal solutions were quenched from a one-phase regime at high temperature to a two-phase regime at low temperature. Solubility phase diagrams were obtained for gold nanoparticles with different ligands in the mixtures of different ratios of 2-butanone and toluene or t-butyl toluene. The explanation from classical ideal solution theory gave the fusion enthalpy of superclusters.

Temperature quenches from the one-phase to the two-phase regime yielded superclusters of the nanoparticle solid phase with sizes that depended on the quench depth. Classical nucleation theory was used to describe these sizes using a relative small value of the surface tension for the nanoparticle solid phase. This value is consistent with molecule size scaling of the surface tension. In total these results show that the solubility behavior of nanoparticles in colloidal solution is similar to the behavior in molecular solutions.

SOLUBILITY PHASE TRANSITION BEHAVIOR OF GOLD NANOPARTICLES IN COLLOIDAL SOLUTION

by

HAO YAN

B.S., Nanjing University, 1995
M.S., Peking University, 2001

A DISSERTATION

submitted in partial fulfillment of the requirements for the degree

DOCTOR OF PHILOSOPHY

Department of Physics
College of Arts and Sciences

KANSAS STATE UNIVERSITY
Manhattan, Kansas

2009

Approved by:

Major Professor
Christopher M. Sorensen

Abstract

Nano-size materials are new materials in an intermediate state between the bulk and atomic or molecular states. Nanoparticles in colloidal solution and their assemblies have the great attention of researchers to investigate the novel fundamental properties and numerous applications. In this dissertation, we investigated the solubility phase transition behavior of gold nanoparticles in colloidal solution.

We used the nearly monodisperse gold nanoparticles synthesized by either the inverse micelle or the solvated metal atom dispersion methods followed by digestive ripening. The gold nanoparticles were ligated with alkyl chains, which were dodecanethiol, decanethiol, or octanethiol for individual samples. They dispersed in toluene or t-butyl toluene like large molecules at room temperature. In analogy to molecular solutions, the colloidal solution had thermally reversible phase transitions between a dissolved phase of dispersed single nanoparticles and dispersed-aggregation co-existing phase. A more polar solvent, 2-butanone, was added to the colloidal solution for changing the solubility of gold nanoparticles and adjusting the phase transition temperatures to accessible temperatures. Superclusters formed by the nanoparticles when the colloidal solutions were quenched from a one-phase regime at high temperature to a two-phase regime at low temperature. Solubility phase diagrams were obtained for gold nanoparticles with different ligands in the mixtures of different ratios of 2-butanone and toluene or t-butyl toluene. The explanation from classical ideal solution theory gave the fusion enthalpy of superclusters.

Temperature quenches from the one-phase to the two-phase regime yielded superclusters of the nanoparticle solid phase with sizes that depended on the quench depth. Classical nucleation theory was used to describe these sizes using a relative small value of the surface tension for the nanoparticle solid phase. This value is consistent with molecule size scaling of the surface tension. In total these results show that the solubility behavior of nanoparticles in colloidal solution is similar to the behavior in molecular solutions.

Table of Contents

List of Figures

List of Tables

Acknowledgements

I would like to show my deepest gratitude to my advisor Dr. Christopher M. Sorensen. What I learned from him are not only the physics theory and the experimental techniques used to complete this dissertation, but also the attitude and the method to work as an independent scientist. He has been like a father and also a friend with his education and encouragement through my academic program and many difficult times.

I would like to thank all the members in our NIRT program for the discussions in every week group meeting. Special appreciations go to Dr. Amit Chakrabarti for his theory support and very helpful suggestions, Dr. Kenneth Klabunde for his help with gold nanoparticles synthesis, Dr. Bruce Law for his valuable advice and experimental apparatus, and Dr. Christer Aakeröy for his sample support. All the samples in my experiments were synthesized by Dr. Al Smetana, and Sreeram Cingarapu. I would like to thank them for their help.

I cannot forget to thank all the members in Sorensen group for those happy laboratory days. Especially I would like to thank Dr. Tahereh Mokhtari and Dr. Rajan Dhaubhadel for their help with light scattering work.

I thank my parents, my brother and my sister for their everlasting love, support and encouragement throughout my life. I would like to express thanks to my loving wife Chunxia for her love, inspiration and companionship during all the times with happiness and tears.

Dedication

I dedicate this dissertation to my parents and my wife.

CHAPTER 1 - Introduction

Nanomaterials with size ranging from 1nm to 100nm, also known as nanocrystals, nano clusters and nanoparticles, can be found both in nature and man-made materials [1]. Materials reduced to the nanometer scale can show very different properties compared to what they exhibit on a macro scale. Material such as gold, which is one of the most chemical inert elements in nature, can serve as a potent chemical catalyst at nanoscales [2].

From the fundamental point of view, nanomaterials provide an intermediate domain to study the transition from atomic properties to bulk properties. Quantum mechanical calculations have shown that particles with size range 1-10nm have unique electronic band structures [3]. Therefore nanomaterials have many unique physical properties that are directly related to the discrete electronic band structures, comparing with bulk materials. Another significant difference between bulk materials and nanomaterials is that nanomaterials have a much higher surface to volume ratio. Hence, many properties of these materials are determined by the surface atoms rather than the interior atoms. Melting points for both semiconductor and metal nanoparticles are significantly lower than the corresponding bulk materials [4,5]. This is caused by the surface free energy of the nanocrystals. The large influence of the particle surface also opens up the possibility to modify the surface or interface of the nanomaterials to control their properties.

The first truly scientific study of gold nanoparticles was conducted by Michael Faraday in 1857 in which he reported the reduction of a solution of $AuCl_4^-$ resulted in a red solution of

gold colloid [6]. During the time of Faraday, engineering the particles to have specific properties was proved very difficult due to the polydispersity of the particle sizes. The new discovered techniques such as digestive ripening allow us to control the size of gold nanoparticles during their synthesis with narrow size distributions. These techniques enabled material scientists to systematically study the properties of gold nanoparticle colloidal solutions.

The near monodispersity is the analogue to compound stoichiometry. For example, a typical dodecanethiol ligated gold nanoparticle with a 5.0nm diameter can be expressed as a large molecule

$$Au_{3850}(C_{12}SH)_{350}$$

In the chemical formula, the standard deviation on the atoms number is about 10%. This is close to the uniformity in mass of most compounds given the variety of sable isotopes. The analogy suggests that those gold nanoparticle systems can be treated as a new kind of stoichiometric particle compounds. The size of disperse components in a colloidal solution can vary from molecular size to micron size. The colloidal solutions display a series phase transitions between gas, liquid and solid phases [7]. The phase transition of colloidal solutions with molecular species and micron size particles as disperse components have been investigated wildly while the important intermediate size region with nanosize stoichiometric particle compounds has not been studied.

The new nanoparticle materials bridge the size gap between solutions and traditional colloids. The synthetic control of the particles and their ligands also allows for control of the

phase behavior of the nanoparticle colloidal solution at a much higher and detailed level than in the other systems.

Nanoparticles are usually surface ligated with any of a variety of organic compounds and these ligands cause colloidal solutions of the nanoparticles to be stable against irreversible aggregation. Often these colloidal solutions act as solutions with the nanoparticles displaying reversible temperature and solvent dependent solubility [8]. In many cases when the nanoparticles are highly uniform, the precipitating solid is a two- or three-dimensional superlattice of the nanoparticles. Thus there is strong analogy to the phase behavior of molecular solutions, and it is then reasonable to ask what controls the phase behavior of nanoparticle solutions and what is the nature of nucleation and growth of the insoluble phase? Such questions are not only of inherent intellectual interest but are also very useful, for with an understanding of this science, we will be able to control the self-assembly of nanoparticles into superlattices, ramified aggregates, gels, and films on surfaces. There are recent studies of the growth of clusters of the solid precipitate phase from solutions destabilized by either ligand exchange [9] or synthesis in a poor solvent [10]. Still lacking are phase diagram measurements and nucleation studies.

In this dissertation work, we investigated the solubility phase transition behavior of gold nanoparticles in colloidal solution.

In chapter 2, we give an introduction to the concept of colloidal solution and classical solubility theory for ideal solution and regular solution. Classical nucleation theory is also

introduced for the explanation of cluster growth. In chapter 3, techniques of synthesizing nanoparticles, inverse micelle method and solvated metal atom dispersion method followed with digestive ripening, are reviewed. And the super structure formed by the nanoparticles is briefly described. The static and dynamic light scattering theory and the experimental setup are given in chapter 4. In chapter 5, we described the optical properties of gold nanoparticles and superclusters, and the theory and the experimental method of concentration measurement by UV-Vis spectroscopy. We then present our experimental results of studies on the solubility phase diagram of gold nanoparticles in chapter 6, followed by the study on the nucleation of gold nanoparticle superclusters in chapter 7. In chapter 8, we give a conclusion of our work.

CHAPTER 2 - Solubility Phase Behavior of Solids in Liquids

2.1 Solution, Suspension and Colloidal Solution

Based on distinct properties, the mixtures of solids and liquids can be classified into solution, suspension and colloidal solution. This classification is necessary to understand the concept of colloidal solutions and distinguish it from rest of the types.

As we all know, a solution is a homogeneous mixture of two or more substances in which the substance (the solute) dispersed to molecules or ions in the solvent has the particle size of less than 10^{-9} m or 1 nm. A simple solution of sugar in water is an example of a true solution. Particles of a solution cannot be filtered out by filter papers and are not visible to naked eye.

A suspension is a heterogeneous mixture in which particle size of one or more components is greater than a few microns. When mud is dissolved in water and stirred vigorously; particles of mud are distributed evenly in water. After some time, the particles of this solution settle under water due to the influence of gravity. Contrary to a solution, particles of a suspension are big enough to scatter light or even be seen with naked eye.

The term colloid was coined by Thomas Graham (1861) for glue-like materials which appeared to consist of only one phase when viewed under the microscope [11,12]. A colloidal solution is a mixture in which the particle size of a substance is intermediate between a solution and a suspension i.e. between 1nm-1μm. The smoke from a fire is an example of a colloidal system in which tiny particles of solid float in air. Just like solutions, colloidal particles are small

enough and cannot be seen through naked eye. They easily pass through filter paper. But colloidal particles are big enough to be blocked by animal membrane. The particles in a colloid are larger than in a solution. They are small enough to be dispersed evenly and maintain a homogeneous appearance, but large enough to scatter light.

The differences between solution, suspension and colloidal solution are summarized in Table 2.1.

In physics, a colloidal solution is a very interesting model system for atoms. Colloidal particles are large enough to be observed by many optical techniques such as light scattering and confocal microscopy. Many of the forces that govern the structure and behavior of matter, such as excluded volume interactions or electrostatic forces, govern the structure and behavior of colloidal solutions. For example, the same techniques used to model ideal gases can be applied to model the behavior of a hard sphere colloidal solution. Phase transitions in colloidal solutions can be studied in real time using optical techniques, and are analogous to phase transitions in solutions.

Table 2.1 Difference between Solution, Suspension and Colloidal Solution

Property	Solution	Colloidal Solution	Suspension
Size of the particles	<1nm	1nm-1μm	>1μm
Dispersion	Monodisperse	Monodisperse	Polydisperse
Visibility	Particles of solution are not visible to naked eye	Colloidal particles are not seen to naked eye but can be studied through ultra microscope.	Suspension particles may be seen by naked eye.
Light Scattering	Solution does not scatter light	Colloidal solution scatters light	Suspension scatters light
Stability	Stable	Stable	Unstable
Appearance	Transparent	Transparent or Translucent	Opaque

2.2 Solubility Phase Behavior in Solution

At a certain temperature, when a solid (solute) is mixed with a liquid (solvent) to form a solution, the molecules or ions on the solid surface will leave the surface and disperse uniformly into the liquid. At the same time, the solute molecules or ions are moving in the solvent. And when they touch the solid surface, they will be absorbed back on the surface. If the speeds of those two processes are equal, the concentration of the solution stays in a constant. That concentration is the solubility of the solute in the solvent at that temperature and the solution is in solubility equilibrium. Solubility equilibrium is a type of chemical equilibrium relationship

between solid and dissolved phases of a compound at saturation. The solution in solubility equilibrium is called saturated solution.

The factors that affect the solubility equilibrium, under normal circumstances, are temperature and solution concentration. By changing the conditions of the sample, the equilibrium is broken and the particles transit between the solid phase and the dissolved phase to form a new equilibrium. The solubility phase transition of solutions is well studied for decades while the solubility phase transition of nanoparticle colloidal solutions is a new area to be investigated.

2.2.1 Classical Solubility Theory

The solubility of solids dispersed in liquids varies enormously. A solid solute may form a highly concentrated solution in a solvent in some cases and the solubility may be rarely detectable in other cases. The solubility depends on the activity coefficient of the solute, which is a function of the intermolecular forces between solute and solvent. In the absence of specific chemical effects, intermolecular forces between chemically similar species lead to a smaller endothermic enthalpy of solution than those between dissimilar species. The well-known guide "like dissolves like" is just an empirical statement indicating that. Since dissolution must be accompanied by a decrease in the Gibbs energy, a low endothermic enthalpy is more favorable than a large one. However, factors other than intermolecular forces between solvent and solute also play a large role in determining the solubility of a solid. The solubility also depends on the fugacity of the standard state to which that activity coefficient refers and on the fugacity of the pure solid.

We can start with the equality of the solute fugacities in each phase. If we assume the solid phase fugacity of the solute is that of the pure solid, we have the single equilibrium relation

$$f_1^S = f_1^F \tag{2.1}$$

where the superscripts S and F refer to the solid and fluid phases respectively and we denote the solute by the subscript 1. For liquid mixtures, the fugacity of the solute is

$$f_1^F = x_1 \gamma_1 f_1^L \tag{2.2}$$

where x_1 is the saturation mole fraction, or the solubility, of the solid solute in the solvent, γ_1 is the activity coefficient of solute and f_1^L is the fugacity of the pure solute as a liquid. Combining equation (2.1) and (2.2) gives

$$x_1 = \frac{f_1^S}{\gamma_1 f_1^L} \tag{2.3}$$

So the solubility depends on not only the activity coefficient but also on the ratio of fugacities of the pure solute as a solid and as a liquid. Those two fugacities depend only on the properties of the solute; they are independent of the nature of the solvent.

The molar Gibbs free energy change of fusion $\Delta G_{fus}(T)$ is related to the fugacity ratio by [13,14]

$$\Delta G_{fus}(T) = RT \ln \frac{f_1^L}{f_1^S} \tag{2.4}$$

2.2.2 Ideal Solution

An ideal solution or ideal mixture is a solution in which the enthalpy of dissolution (or "enthalpy of mixing") is zero [13]. The closer to zero the enthalpy of dissolution is, the more "ideal" the behavior of the solution becomes.

Ideality of solutions is analogous to ideality for gases, with the important difference that intermolecular interactions in liquids are strong and can not simply be neglected as they can for ideal gases. Instead we assume that the mean strength of the interactions is the same between all the molecules of the solution. Just as the law of the ideal gas is to describe the behavior of actual gases as, so the law of the ideal solution is the first approximation to describe actual solutions within certain limits.

Since the enthalpy of mixing (solution) is zero, the change in Gibbs free energy on mixing is determined solely by the entropy of mixing. The total entropy of mixing N_i moles of particles of components is given by

$$\Delta S_{total} = k_B \sum_i N_i \ln \frac{\sum_j N_j}{N_i} \qquad \textbf{(2.5)}$$

This leads to the molar entropy ΔS of

$$\Delta S = -R \sum_i x_i \ln x_i \qquad \textbf{(2.6)}$$

where x_i is the mole fraction of component i. Hence the molar Gibbs free energy of mixing is

$$\Delta G = -T\Delta s = RT \sum_i x_i \ln x_i \qquad \textbf{(2.7)}$$

Note that this free energy of mixing is always negative (since each x_i is positive and $x_i < 1$, each $\ln x_i$ must be negative) i.e. ideal solutions are always completely miscible. The equation above can be expressed in terms of chemical potentials of the individual components

$$\Delta G = \sum_i x_i \Delta \mu_i \qquad \textbf{(2.8)}$$

where $\Delta \mu_i$ is the change of chemical potential of i on mixing, defined as

$$\Delta \mu_i = RT \ln x_i \qquad \textbf{(2.9)}$$

Thus the chemical potential of the solute in the saturated solution μ_{solute} is

$$\mu_{solute} = \mu_{liquid} + \Delta\mu_1 = \mu_{liquid} + RT \ln x_1 \quad \textbf{(2.10)}$$

where μ_{liquid} is the chemical potential of the pure liquid solute, x is the mole fraction of solute in saturated solution. In solid-solution equilibrium, the chemical potential of the pure solid solute μ_{solid} is equal to the chemical potential of the solute in the saturated solution.

$$\mu_{solid} = \mu_{solute} \quad \textbf{(2.11)}$$

From the equations (2.10) and (2.11), we have

$$\ln x_1 = -\left(\mu_{liquid} - \mu_{solid}\right)/RT = -\Delta G_{fus}(T)/RT \quad \textbf{(2.12)}$$

Compare equations (2.4) and (2.12) and notice equation (2.3), we can determine the activity coefficient of solute $\gamma_1 = 1$ when the solution is an ideal solution.

$\Delta G_{fus}(T)$ can be computed by separately calculating the enthalpy of fusion $\Delta H_{fus}(T)$ and the entropy of fusion $\Delta S_{fus}(T)$, and then using the relation

$$\Delta G_{fus}(T) = \Delta H_{fus}(T) - T\Delta S_{fus}(T) \quad \textbf{(2.13)}$$

Clearly, $\Delta G_{fus}(T_m) = 0$ at melting point T_m. In most case, we assume the heat capacities of pure solid and pure liquid are equal, $\Delta C_p = 0$, then we have

$$\Delta H_{fus}(T) = \Delta H_{fus}(T_m) \quad \textbf{(2.14)}$$

and

$$\Delta S_{fus}(T) = \Delta S_{fus}(T_m) = \frac{\Delta H_{fus}(T_m)}{T_m} \quad \textbf{(2.15)}$$

Substitute equations (2.14) and (2.15) into equation (2.13), we have

$$\Delta G_{fus}(T) = \Delta H_{fus}(T_m) - T\frac{\Delta H_{fus}(T_m)}{T_m} = \Delta H_{fus}(T_m)\left(1 - \frac{T}{T_m}\right) \quad \textbf{(2.16)}$$

Combining equations (2.12) and (2.16), we obtain

$$-\ln x_1 = \frac{\Delta H_{fus}(T_m)}{RT}\left(1 - \frac{T}{T_m}\right) \quad \textbf{(2.17)}$$

If $\Delta C_p \neq 0$, an additional term will be added as the following [15],

$$-\ln x_1 = \frac{\Delta H_{fus}(T_m)}{RT}\left(1 - \frac{T}{T_m}\right) - \frac{\Delta C_p}{R}\left[1 - \frac{T_m}{T} + \ln\frac{T_m}{T}\right] \quad \textbf{(2.18)}$$

We can deduce some qualitative rules from equation (2.18),

1) The solubility of a given solid is greater the higher the temperature if the enthalpy of fusion is greater than the heat of mixing, which is true fore most cases. . The change rate depends on the heat of fusion of the solute.
2) A solid having a higher melting temperature is less soluble at a given temperature than one having a lower melting temperature.

2.2.3 Regular Solution

By combining equations (2.3), (2.4), and (2.16), we have the solubility equation for any solutions

$$-\ln x_1 = \ln\gamma_1 + \frac{\Delta H_{fus}(T_m)}{RT} - \frac{\Delta H_{fus}(T_m)}{RT_m} = \ln\gamma_1 + \frac{\Delta H_{fus}(T_m)}{RT}\left(1 - \frac{T}{T_m}\right) \quad \textbf{(2.19)}$$

Whenever there is a significant difference in the nature and size of the solute and solvent molecules, the solution is no longer ideal and we may expect that the activity coefficient γ_1 is

not equal to one. In nonpolar solutions, where only dispersion forces are important, γ_1 is generally larger than one (and thus the solubility is less than that corresponding to ideal behavior), but in cases where polar or specific chemical forces are important, the activity coefficients may well be less than one with correspondingly higher solubilities. Such enhanced solubilities, for example, have been observed for unsaturated hydrocarbons in liquid sulfur dioxide [14].

There is no general method for predicting activity coefficients of solids solutes in liquid solvents. The regular solution theory, first given by Hildebrand [16,17], has an alternative way to estimate the activity coefficient with the Scatchard-Hildebrand equation

$$RT \ln \gamma_1 = V_1 (\delta_1 - \delta_2)^2 \Phi_2^2 \qquad \textbf{(2.20)}$$

where V_1 is the molar volume of the pure liquid solute, δ_1 and δ_2 are the solubility parameters of solute and solvent, and

$$\Phi_2 = \frac{x_2 V_2}{x_1 V_1 + x_2 V_2} \qquad \textbf{(2.21)}$$

is the volume fraction of solvent. When x_1 is small, $\Phi_2 \approx 1$. So a good approximation of solubility equation for regular solution is

$$-\ln x = \frac{\Delta H_{fus}(T_m)}{RT}\left(1 - \frac{T}{T_m}\right) + \frac{V_1(\delta_1 - \delta_2)^2}{RT} \qquad \textbf{(2.22)}$$

The solubility parameters δ can be computed by

$$\delta = \left(\frac{\Delta U_{vap}}{V}\right)^{1/2} \qquad \textbf{(2.23)}$$

if the vaporization energy ΔU_{vap} and the molar liquid volume V are given.

2.3 Classical Nucleation Theory

When a saturated solution in solubility equilibrium, i.e. the concentration of the solution equals the solubility of the solute in the solvent, is quenched to a lower temperature, the system is not in an equilibrium state any more, but in a metastable state, e.g., super-saturated system or super-cooled system. The Gibbs free energy is the minimum when system is in an equilibrium state and all the phases in the system have the same chemical potential. The metastable phase tends to change to stable phase because of the energy benefit. The particles tend to aggregate and form the crystal lattice or superlattice if the particles are monodisperse. However, the condition of super-saturation or super-cooling alone is not sufficient cause for a system to begin to aggregate or crystallize. Before the solid phase can develop there must exist in the solution a number of minute solid bodies, embryos, nuclei or seeds, which act as centers of aggregation or crystallization. Nucleation may occur spontaneously (homogeneous nucleation) or it maybe induced artificially (heterogeneous nucleation).

2.3.1 Homogeneous nucleation

Exactly how a stable crystal nucleus is formed within a homogeneous fluid is not known with any degree of certainty. A stable nucleus could hardly result from the simultaneous collision of the required number of molecules since this would constitute an extremely rare event. More likely, it could arise from a sequence of bimolecular additions according to the scheme [18]:

$A + A \Leftrightarrow A_2$

$A_2 + A \Leftrightarrow A_3$

$A_{n-1} + A \Leftrightarrow A_n$ (critical cluster)

Ions or molecules in a solution can interact to form short-lived clusters. Short chains may be formed initially or flat monolayers, and eventually a crystalline lattice structure is built up. The construction process, which occurs very rapidly, can only continue in local regions of very high super-saturation and many of the embryos or "sub-nuclei" fail to achieve maturity; they simply redissolve because they are extremely unstable. Recently, Gebauer et al. demonstrated the presence of large, well-defined clusters before nucleation of one of the phases of calcium carbonate [19,20]. If, however, the nucleus grows beyond a certain critical size, it becomes stable under the average conditions of super-saturation obtaining in the bulk of the fluid.

Nucleation is often slow because of a free-energy barrier originating from the interface between the nucleus and its surroundings. As the nuclei grow, their Gibbs free energy increases, until a free energy maximum is reached at the critical size. Beyond the critical size, the nuclei are stable and release energy during growth. The free energy changes associated with the process of homogeneous nucleation may be considered as the following.

The overall excess Gibbs free energy ΔG between a small solid cluster of solute and the solute in solution comes from two contributions. One is the surface excess free energy ΔG_S, i.e. the excess free energy between the surface of the cluster and the bulk of the cluster, another is the volume excess free energy ΔG_V, i.e. the excess free energy between a very large cluster and the solute in solution. ΔG_S is a positive quantity, the magnitude of which is proportional to the surface area of the cluster. In a super-saturated solution, G_V is a negative quantity proportional to the volume of the cluster. Simply assuming the cluster is a sphere of radius *r*, we have

$$\Delta G = \Delta G_S + \Delta G_V$$

$$= 4\pi r^2 \gamma + \frac{\frac{4}{3}\pi r^3}{v} \Delta g \qquad \textbf{(2.24)}$$

where and γ is the interfacial tension between the developing cluster surface and the supersaturated solution in which it is located, *v* is the volume occupied by a monomer in the cluster (not in the solution), and Δg is the Gibbs free energy change of the transformation from solution to cluster for each particle. The two terms on the right-hand side of equation (2.24) are of opposite sign and depend differently on *r*, so the Gibbs free energy of formation passes through a maximum, as shown in Figure 2.1. This maximum value ΔG_c corresponds to the critical nucleus r_c. For a spherical cluster is obtained by maximizing equation (2.24), setting $d\Delta G / dr = 0$:

$$\frac{d\Delta G}{dr} = 8\pi r_c \gamma + 4\pi r_c^2 \Delta g / v = 0 \qquad \textbf{(2.25)}$$

thus

$$r_c = \frac{-2v\gamma}{\Delta g} \qquad \textbf{(2.26)}$$

And the maximum free energy is

$$\Delta G_c = \frac{16\pi v^2 \gamma^3}{3\Delta g^2} = \frac{4\pi\gamma r_c^2}{3} \qquad \textbf{(2.27)}$$

The behavior of a newly created crystalline lattice structure in a supersaturated solution depends on its size; it can either grow or redissolve, but the process which it undergoes should result in the decrease in the free energy of the particle. The critical size r_c, therefore, represents

the minimum size of a stable nucleus. Particles smaller than r_c will dissolve because only in this way can the particle achieve a reduction in its free energy. Similarly, particles larger than r_c will continue to grow.

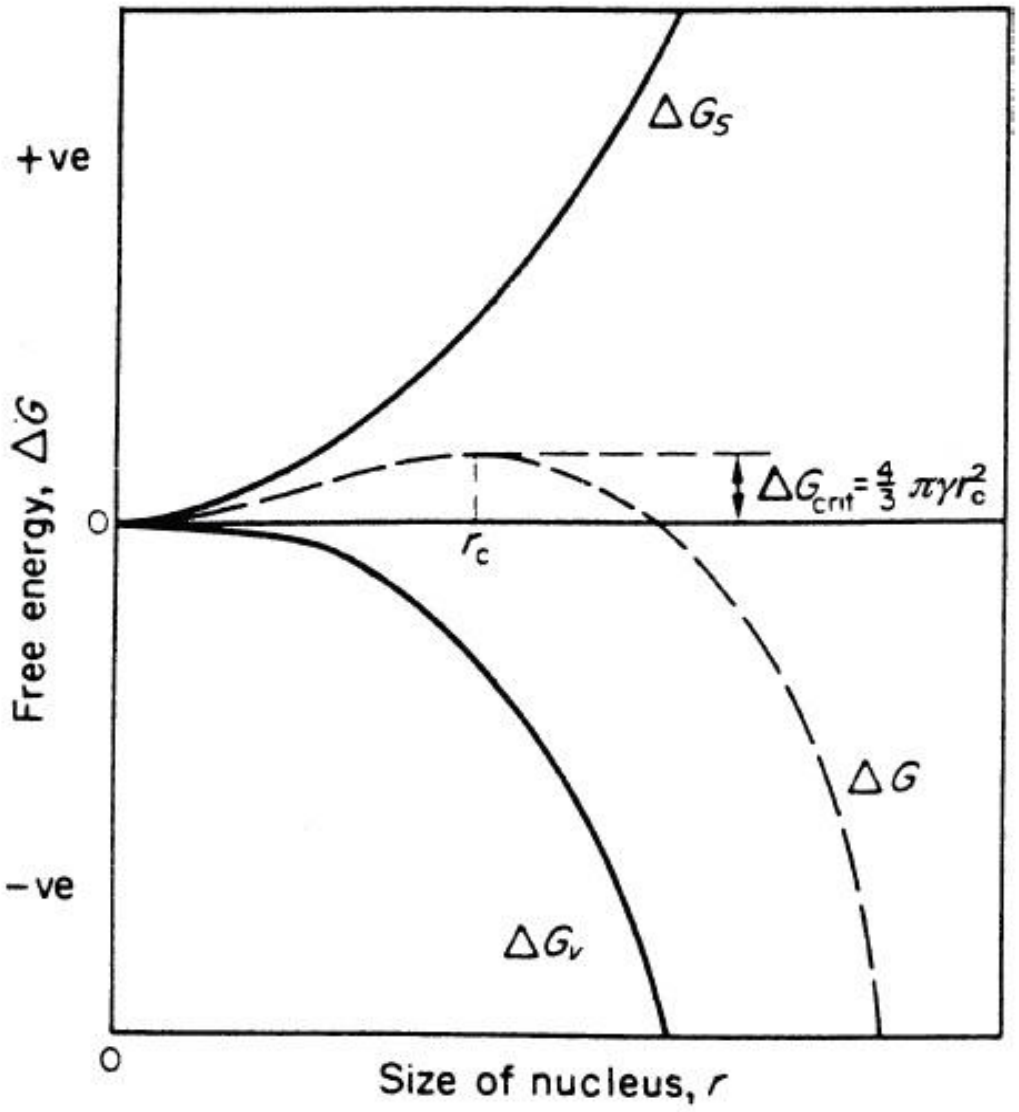

Figure 2.1 Gibbs free energy diagram for nucleation explaining the existence of the energy barrier and a critical nucleus **[18]**.

The chemical potential of solute in solution is

$$\mu = g + RT \ln x \tag{2.28}$$

where g is the chemical potential of pure solute and x is the molar fraction of the solute in solution. The second term of the chemical potential comes is the mixing term from equation (2.9), as we discussed in section 2.2.2. The chemical potential of solute in clusters should equal the chemical potential of solute in a saturated solution, hence

$$\mu = g + RT \ln x_1 \tag{2.29}$$

where x_1 is molar fraction in the saturated solution, i.e. solubility of the solute in solvent. So the chemical potential difference of solute in cluster and solute in solution is

$$\Delta\mu = -RT \ln(x / x_1) = -RT \ln s \tag{2.30}$$

where s is the saturation ratio defined by $s = x / x_1$, or expressed by the ratio of concentration C in mg/ml and solubility C^* in mg/ml as $s = C / C^*$, mostly used in our study.

Similarly, the Gibbs free energy change of the transformation from solution to cluster for each particle is

$$\Delta g = -k_B T \ln s \tag{2.31}$$

Substitute equation (2.31) into equations (2.26) and (2.27), the critical nucleus radius and the critical free energy change are

$$r_c = \frac{2v\gamma}{k_B T \ln s} \tag{2.32}$$

and

$$\Delta G_c = \frac{16\pi v^2 \gamma^3}{3k_B^2 T^2 (\ln s)^2} \tag{2.33}$$

The number density of the growable nuclei is given by the simple Boltzmann expression

$$n_c = n_0 \exp\left(-\frac{\Delta G_c}{k_B T}\right) = n_0 \exp\left[-\frac{16\pi v^2 \gamma^3}{3k_B^3 T^3 (\ln s)^2}\right] \quad \textbf{(2.34)}$$

where n_0 is initial number density of monomers in supersaturated solution, which can be computed from the initial concentration x, the volume v occupied by a monomer in the cluster (not in the solution), and the mass density ρ of clusters

$$n_0 = \frac{C}{\rho v} \quad \textbf{(2.35)}$$

And the induction time of nuclei formation can be given by [21]

$$t_{ind} = B \exp(\Delta G_c / k_B T) = B \exp\left[\frac{16\pi v^2 \gamma^3}{3k^3 T^3 (\ln s)^2}\right] \quad \textbf{(2.36)}$$

where B is a pre-exponential factor depends on the circumstances.

2.3.2 Cluster Growth

As soon as stable nuclei, i.e. clusters larger than the critical size have been formed in a supersaturated or supercooled system, they keep growing after they overcame the energy barrier.

LaMer and Dinegar gave a growth model by assuming a short nucleation burst followed by diffusional growth of the nuclei [22]. In that model, the growth of each nucleus is influenced only by the monomers in an impermeable spherical shell, centered on the nucleus, with the volume $1/n_c$, where n_c is the number density of the growable nuclei given by equation (2.34). We can define the radius of the spherical shell as

$$h = \left(\frac{3}{4\pi n_c}\right)^{\frac{1}{3}} \quad \textbf{(2.37)}$$

The radius of growing cluster R changes with time t as [22]

$$\frac{dR}{dt} = D\left(\frac{C - C^*}{\rho R} - \frac{R^2}{h^3}\right) \tag{2.38}$$

The diffusion constant D is given by the Stokes-Einstein relation

$$D = \frac{k_B T}{6\pi\eta r} \tag{2.39}$$

where η is viscosity of the solvent and r is the radius of monomers.

Equation (2.38) can be integrated to obtain the analytical expression between R and t if $C - C^*$ is considered independent of time. The final result is

$$t = t_0 \cdot f\left(\frac{R}{R_{\max}}\right) \tag{2.40}$$

The function $f(x)$ is defined as

$$f(x) = \frac{1}{6}\ln\left(1 + x + x^2\right) - \frac{1}{3}\ln(1 - x) - \frac{1}{\sqrt{3}}\tan^{-1}\frac{2x+1}{\sqrt{3}} + \frac{1}{\sqrt{3}}\tan^{-1}\frac{1}{\sqrt{3}} \tag{2.41}$$

And two parameters t_0 and $R_{\max}$ are given by

$$t_0 = \frac{1}{D}\left[\frac{9\rho}{16\pi^2 n_c^2\left(C - C^*\right)}\right]^{1/3} \tag{2.42}$$

and

$$R_{\max} = \left[\frac{3\left(C - C^*\right)}{4\pi m_c \rho}\right]^{\frac{1}{3}} \tag{2.43}$$

Equation (2.43) is easy to understand. It gives the maximum size of the clusters. That size is determined by the amount of the excess monomers, i.e. the difference $\left(C - C^*\right)$ between the original solution concentration and solubility, the number density n_c of clusters and the mass

density ρ of clusters. Time parameter t_0 can be regarded as growth critical time. When time $t = t_0$, $R = 0.965R_{\max}$, as shown in Figure 2.2.

Combining equations (2.34), (2.35) and (2.43), we have

$$\frac{4\pi}{3} R_{\max}^3 == v(1-\frac{1}{s}) \exp\left[\frac{16\pi v^2 \gamma^3}{3k_B^3 T^3 (\ln s)^2} \right] \tag{2.44}$$

and

$$t_0 = \frac{6\pi\eta r \rho R_{\max}^2}{k_B T (C - C^*)} \tag{2.45}$$

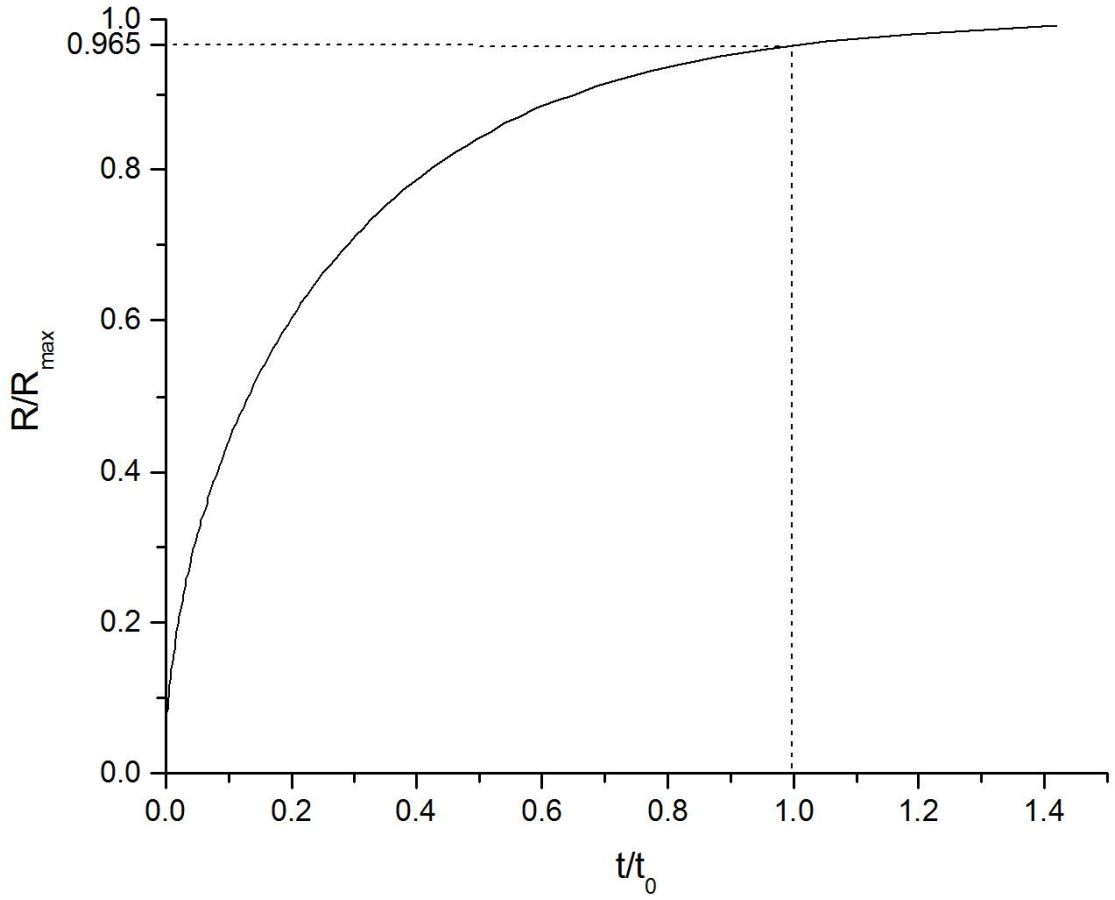

Figure 2.2 The classical nucleation theory result of cluster growth.

CHAPTER 3 - Gold Nanoparticles in Colloidal Solution

3.1 Synthesis of Gold Nanoparticles

Nearly monodisperse gold nanoparticles (AuNPs) were synthesized with a digestive ripening technique. The digestive ripening technique was discovered in our group as a simple but efficient route to convert polydisperse nanoparticles into nearly monodisperse ones by refluxing the colloidal solution in the presence of an excess stabilizing ligand [23]. The pre-digestive ripened nanoparticles were prepared with two methods, the solvated metal atom dispersion (SMAD) method and the inverse micelle method.

3.1.1 Solvated Metal Atom Dispersion Method

The Solvated Metal Atom Dispersion (SMAD) synthesis technique is a batch process that allows for gram quantities of nanoparticles to be produced in a single experiment. The Klabunde group has utilized this technique for an assortment of materials including metal, semiconductor, and organometallic products [23-26].

The driving theory behind the SMAD synthesis is the evaporation of the gold to individual atoms/clusters, separation of the atoms from one another by solvent molecules, and halting their aggregation as soon as possible.

The method involves a reactor composed of a 3000mL elongated glass vessel with 1/2″ walls, as shown in Figure 3.1. Through two opposite outlets water cooled copper electrodes are introduced into the reaction chamber and sealed with Teflon O-rings. The gold is placed in an

aluminum oxide coated tungsten crucible held by the electrodes. The temperature of the crucible is controlled by adjusting the current flow through the electrodes.

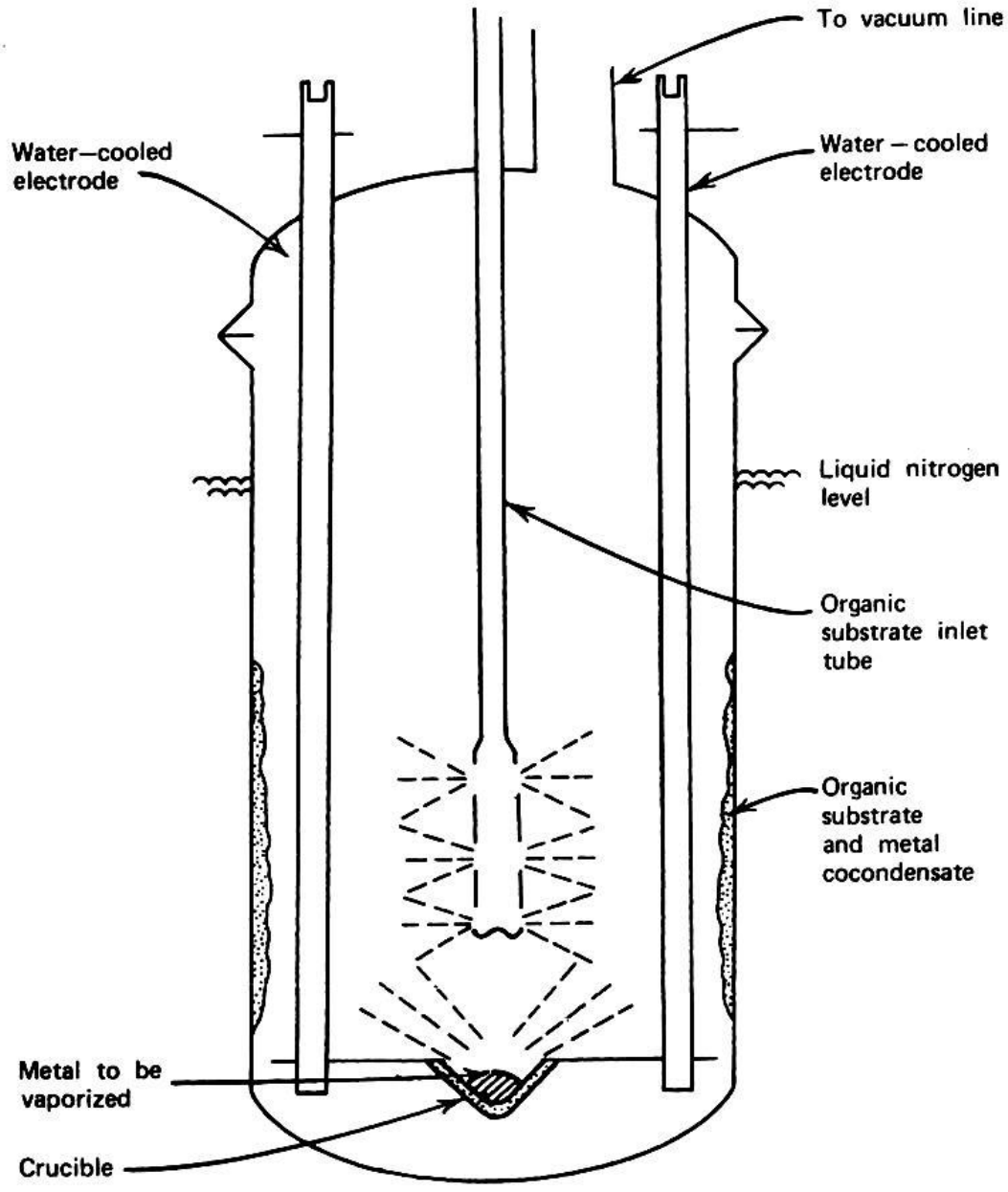

Figure 3.1 Schematic assembly of SMAD reactor.

The center outlet is fitted with a long glass tube sealed on the reactor end and placed directly over the crucible. This end has approximately thirty 1mm holes in it designed to disperse the solvent (acetone) evenly throughout the reactor. The other end is fitted with a ground glass joint that attaches well to a Schlenk tube containing the desired solvent for reaction. A heating element for the solvent shower is placed around the tube. The solvent shower is typically placed 3.5 - 4.0 cm above the crucible for optimal evaporation. Lowering the solvent shower with respect to the crucible will cause it to be coated with excess metal atoms, while raising it higher than 4 cm leads to poor coverage of the solvent on the bottom of the reactor.

The capping agents (ligand) and the solvent (toluene or t-butyl toluene) are placed in the bottom of the reactor with a stir bar. The whole reactor is submerged in liquid nitrogen and evacuated to a minimum of 1×10^{-3} Torr pressure in order for the gold to be evaporated at a temperature low enough that the solvent does not decompose.

After the above apparatus has been assembled it is placed under vacuum for a minimum of 2 hours. The acetone is slowly (roughly 1 hr) deposited on the walls of the reactor forming a bed of frozen solvent. During this time the crucible iss slowly heated to the evaporation temperature of gold. This is typically slightly higher than the melting point of the metal itself. The flow of solvent is slightly increased and the crucible temperature is maintained throughout the reaction. Then the evaporated gold atoms condense onto the walls on top of the layer of solvent. Afterwards, more acetone is released resulting in highly reactive nanoparticles sandwiched between two layers of organic solvent.

After all gold and acetone are co-evaporated and deposited on the wall of the vessel as the frozen purple matrix, the liquid nitrogen is removed and the vessel is allowed to warm under a static vacuum. The gold-acetone matrix melts and mixes with dodecanethiol and toluene or t-butyl toluene at the bottom of the reactor. The frozen pool of solvent and ligand is heated back to a liquid phase. The highly reactive nanoparticles come into contact with the dissolved capping ligand and are surface ligated.

The flask containing the product is then flushed 4 times alternating argon gas and vacuum to remove any traces of oxygen that might have entered during transfer. Acetone is then slowly evaporated under vacuum from the as prepared product mixture overnight, leaving a dispersion containing only toluene (or t-butyl toluene), gold, and capping agent. The particles are relatively small but are non-uniform in shape and size. The prepared product at this stage is not of sufficient quality to study with any accuracy due to the large difference in properties such a wide range of particles would have.

3.1.2 Inverse Micelle Method

The inverse micelle method involves the reduction of a gold metal salt to slowly grow nanocrystals in an inverse micelle environment.

Surfactants are chemical compounds that contain both hydrophobic and hydrophilic groups in their structure (schematically shown in Figure 3.2a). In nonpolar solvents, such compounds aggregate (above a concentration called the critical micelle concentration, CMC) in a way that the hydrophobic groups point towards the solvent and the hydrophilic moieties cluster

together to form the central core of the aggregate (Figure 3.2b) [27]. Such aggregates are called inverse micelles because the spatial arrangement of the surfactant molecules is the opposite of that in water. A major characteristic of inverse micelle systems is their ability to solubilize water and other polar or ionic compounds (for example metal salts) which are not soluble or even slightly soluble in non-polar solvents.

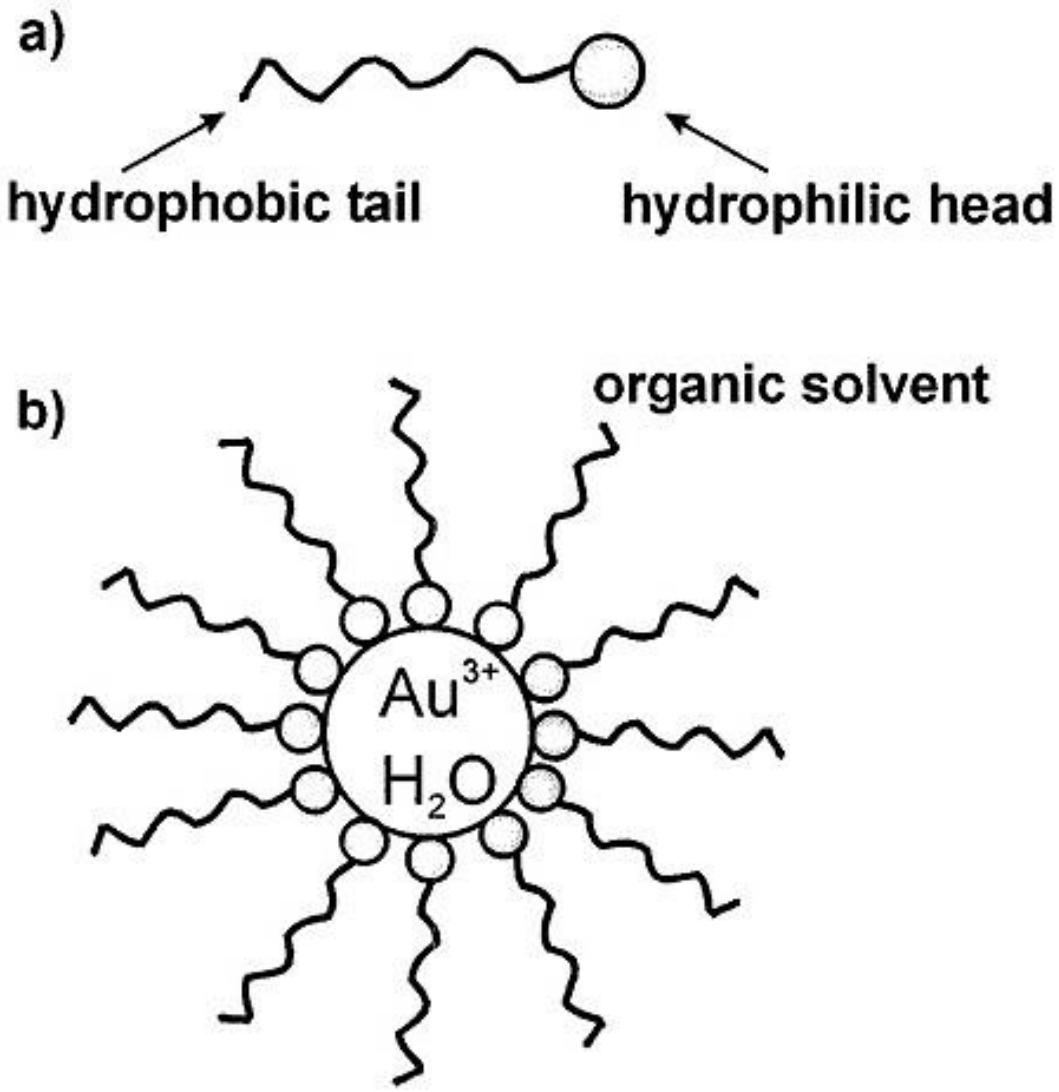

Figure 3.2 Schematic representation of a) surfactant molecule and b) inverse micelle system.

The standard experimental procedure of inverse micelle method in our group is described as the following [28].

All reactions were carried out under Ar atmosphere and all solvents were bubbled with dry Ar gas for 2 hours prior to use. In a typical experiment, 0.104g didodecyldimethylammonium bromide (DDAB) was dissolved in 10 ml toluene to form a 0.02 M inverse micelle solution. At this point no water was added to the system. After half an hour, 0.034 g $AuCl_3$ (99.99%+) was dissolved in the DDAB-toluene solution by sonication. At the end of the sonication process a clear deep orange-red colored $AuCl_3$-DDAB-toluene solution was obtained. After sonication the solution was stirred for several minutes to ensure it reached ambient temperature (the temperature of the solution usually slightly increased after sonication). Freshly prepared aqueous $NaBH_4$ solution (40 μl, 9.4 M) was then added dropwise to the $AuCl_3$-DDAB-toluene solution while vigorously stirring with a magnetic stirrer. The color of the solution changed from orange-red to purple-red within a minute and the stirring was continued for 15 minutes to ensure completion of the reaction.

The 'as-prepared' Au colloid was split into 2.5 ml portions. Stabilizing ligand was added to each portion in molar ratio n(Au)/n(ligand)=1:30. After about 5 minutes agitation, the ligand-stabilized Au colloid in each vial was precipitated by the addition of 7.5 ml ethanol (200 proof, Fisher) in order to purify the system from excess reducing agent, DDAB and the reduction side products. The solution was vigorously agitated and left undisturbed overnight. A purple precipitate formed in each case. The material which settled on the bottom of the vial was isolated from the supernatant by decanting followed by vacuum drying. After vacuum drying 2.5 ml

toluene was injected to the waxy solid in each sample vial obtained. For digestive ripening, another dose of the respective ligands with the same molar ratio n(Au)/n(ligand)=1:30 was added to the samples with shaking. At this stage, the Au particles were not completely re-dispersed in the solvent. We can see the gold particles before digestive ripening are polydisperse from the TEM picture in Figure 3.3.

The stoichiometric equations of the reduction process are presented in Figure 3.4.

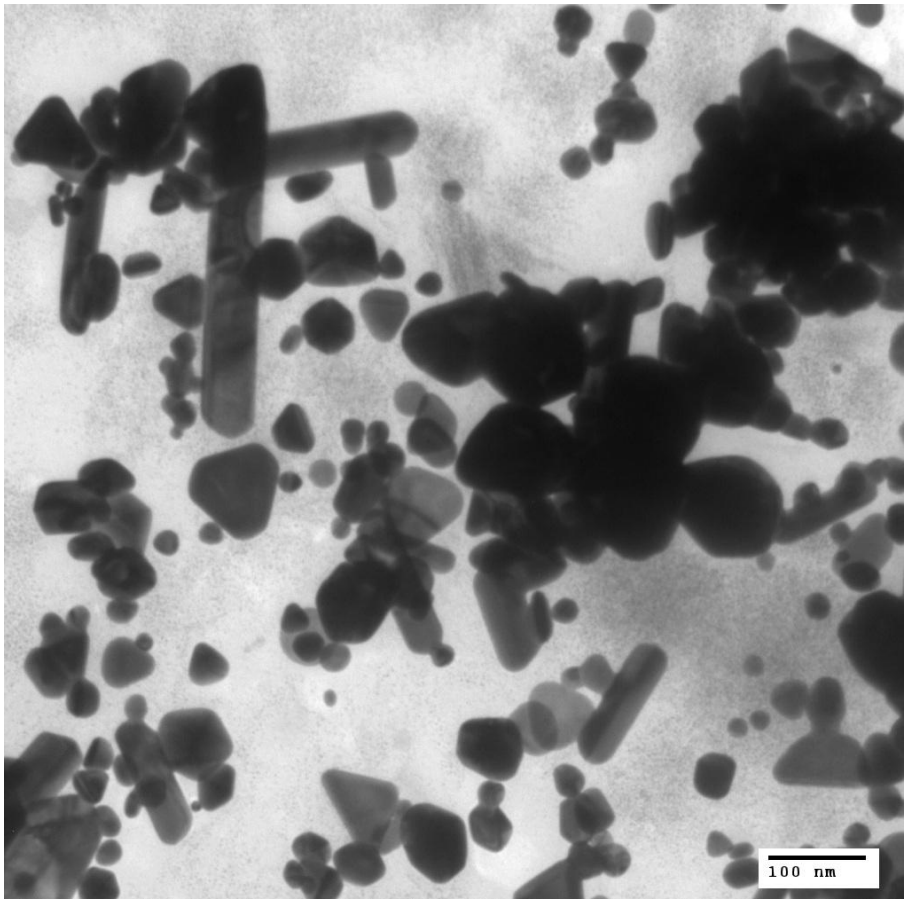

Figure 3.3 TEM picture of dodecanethiol ligated gold nanoparticles in toluene prepared with inverse micelle method before digestive ripening **[29]**.

$$BH_4^- + 4\,H_2O \longrightarrow B(OH)_3 + OH^- + 4H_2$$

$$4H_2 - 8e^- \longrightarrow 8H^+$$

$$BH_4^- + 3\,H_2O - 8e^- \longrightarrow B(OH)_3 + 7H^+$$

$$Au^{3+} + 3e^- \longrightarrow Au$$

$$BH_4^- + 3\,H_2O - 8e^- \longrightarrow B(OH)_3 + 7H^+$$

Therefore:

$$8Au^{3+} + 3BH_4^- + 9H_2O \longrightarrow 8Au + 3B(OH)_3 + 21H^+$$

$$8AuCl_3 + 3NaBH_4 + 9\,H_2O \longrightarrow 8Au + 3B(OH)_3 + 21HCl + 3NaCl$$

Figure 3.4 Stoichiometric equations of the reduction of $AuCl_3$ with $NaBH_4$.

3.1.3 Digestive Ripening

For the nanoparticles to be useful for any systematic study or size-dependent application, they must be monodisperse in size distribution. Digestive Ripening is a term used to describe the refinement process of nanoparticles in solution through heating, first described by Lin and coworkers [23]. In contrast to the well-known Ostwald ripening process, where larger particles grow at the expense of smaller ones, 'digestive ripening' achieves an 'intermediate' thermodynamically stable particle size with still poorly understood reason, typical for the colloidal system. During this technique the atoms and ligands are in flux with the environment and the particles are able to exchange atoms until an equilibrium size is obtained. After heating the colloids for a few hours to a few days the polydisperse as prepared SMAD colloid becomes a uniform solution of spherical particles.

The procedure for digestive ripening is simple. A container that will exclude air during heating is integral to the success of the reaction. To accomplish this, an adapter with a rubber septum is fitted on the Schlenk tube, a process that again is conducted under positive argon pressure and can be fitted in 1-2 seconds. To this an inlet for argon is introduced through a needle and the gas outlet is passed through a bubbler to prevent backflow of air. A constant flow of argon over the reaction seems beneficial to the quality of the final product. The product from the SMAD or the Inverse Micelle preparation is heated in the original Schlenk flask under a flow of argon to reflux at 190 °C. The nanoparticle dispersion is refluxed for 90 minutes under an inert atmosphere. The colloids are then transferred into sample vials and left undisturbed overnight at room temperature. TEM picture of the gold colloid is obtained after the digestive ripening, as shown in Figure 3.5, which shows the highly monodispersion of the nanoparticles.

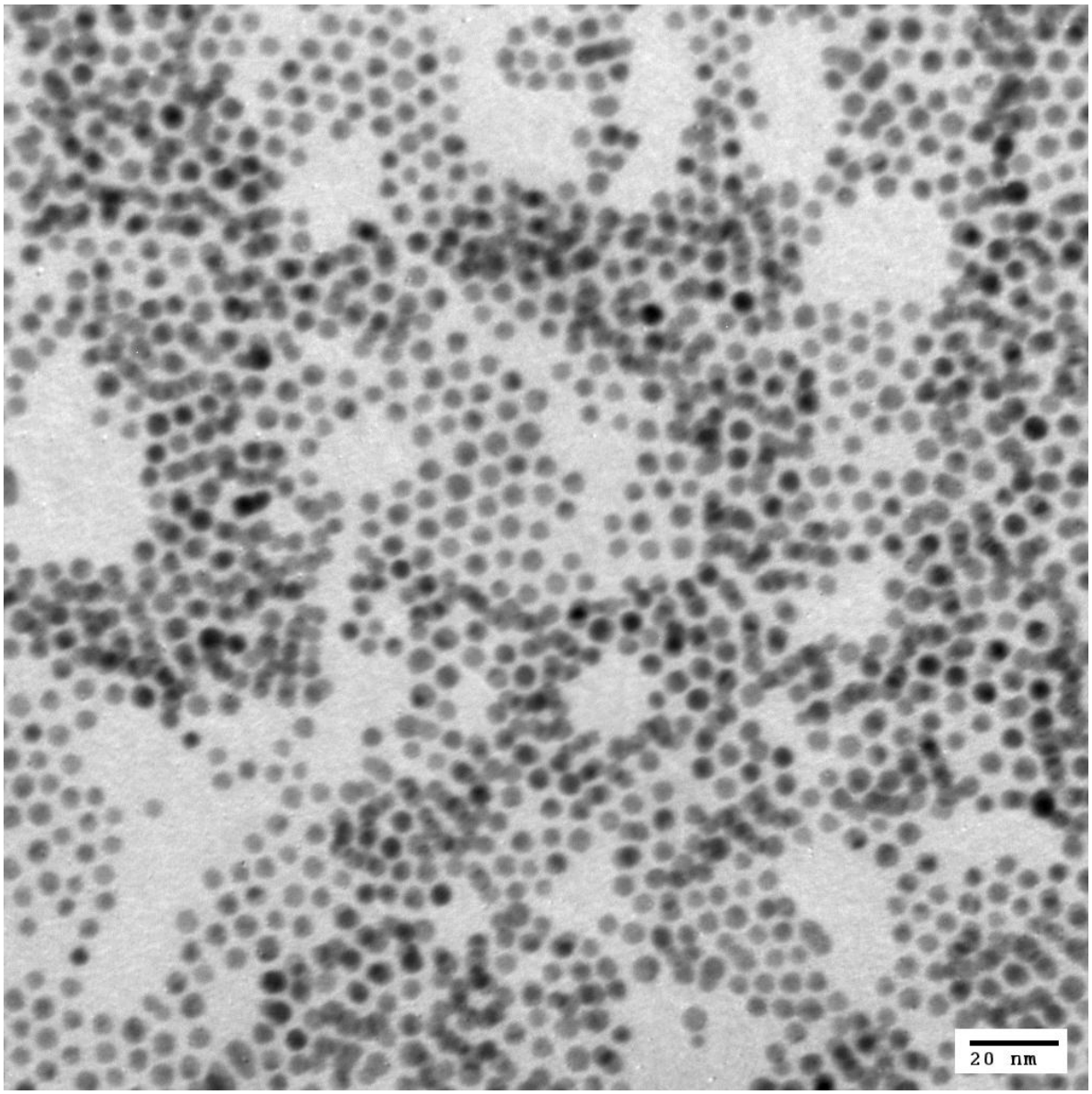

Figure 3.5 TEM picture of dodecanethiol ligated gold nanoparticles in t-butyl toluene after digestive ripening.

The entire synthetic process described above is schematically illustrated in Figure 3.6. The gold nanoparticles produced by those methods were soluble in toluene. The resulting sample was a dark wine red colloidal solution at room temperature.

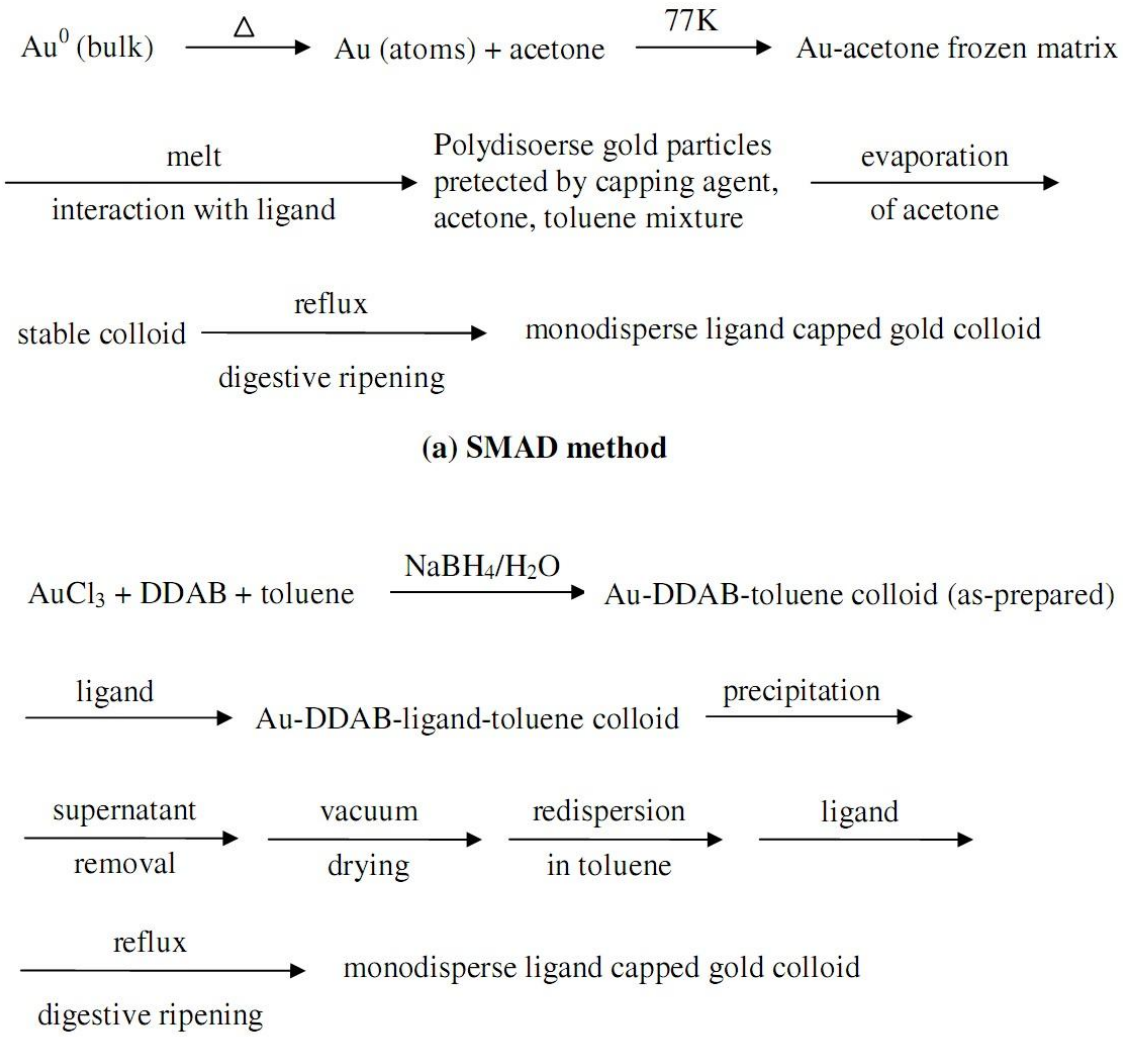

Figure 3.6 Synthetic steps for preparation of monodisperse gold nanoparticles by (a) the SMAD method and (b) the inverse micelle method.

3.2 Superlattice Formation

The spontaneous ordering of nano-materials is becoming a huge area of research recently. The synthesis of nanoparticles that display self-assembly is absolutely essential for the easy fabrication of practical devices incorporating small particles. Constructing these arrays by individual particle placement would be impossible considering the size needed for advanced materials. This is especially true for spherical nanoparticles as the formation of superlattices is an important precursor to the application of nanoparticles as novel optical and electrical materials.

Au colloidal solutions obtained by inverse micelle and SMAD methods with digestive ripening have a strong tendency toward superlattice formation due to the uniformity in size and shape of the nanoparticles present in both systems. Nanocrystal superlattices could be formed by a deposition of Au colloidal solution on a support at ambient conditions. Figure 3.7 is a TEM picture of a sample prepared by placing a 3μl drop of the gold colloidal solution onto a carbon-coated Formvar copper grid [30]. The grids were allowed to dry in a dust-free area for several hours before taking the picture. This nanocrystal superlattice is remarkable in the perfect arrangement of practically monodisperse Au nanoparticles. The packing structure is FCC imaged in $[110]_{SL}$ projection (the subscript "SL" designates planes and directions in the nanocrystal superlattice).

It is fascinating that the nanoparticles construct the exact same packing features as their composite atoms. Nanoparticle superlattice ordering is merely an order of magnitude larger in spatial dimensions. The ordering of both the atoms in the particles and the nanoparticles themselves is cubic close packed. This packing style allows for a maximum amount of nearest

neighbors in a hard sphere model, with components of a similar size. Superlattice formation is somewhat curious in this respect because the particles are by no means perfect spheres. The particles typically have many flat faces to them, and are surrounded by ligands that protrude at an angle from these surfaces.

Besides the formation of nanocrystal superlattice by drying the colloidal solution on a support, we also tried to form the superlattice, coexisting with the nanoparticle monomers, in a solution. Toluene and t-butyl toluene are the good solvents for the gold nanoparticles so the nanoparticles remain in dissolved state at room temperature. To shift the phase transition temperature to an accessible temperature above room temperature, 2-butanone, a poor solvent that is miscible with toluene, was mixed the gold nanoparticles in toluene. Remarkable phase transition phenomena happened after 2-butanone was added. However, attempts to picture the aggregated phase with TEM were foiled because during TEM slide preparation, the bad solvent (2-butanone) evaporated faster than the good solvent (toluene) so that the aggregated phase redissolved on the TEM grid. A term “supercluster” hence is used for a cluster of nanoparticles to replace “superlattice” in subsequent sections and chapters.

The ligands used in this research consisted of hexadecanethiol, dodecanethiol, decanethiol and octanethiol. The synthesis processes for each colloid with different ligand are very similar.

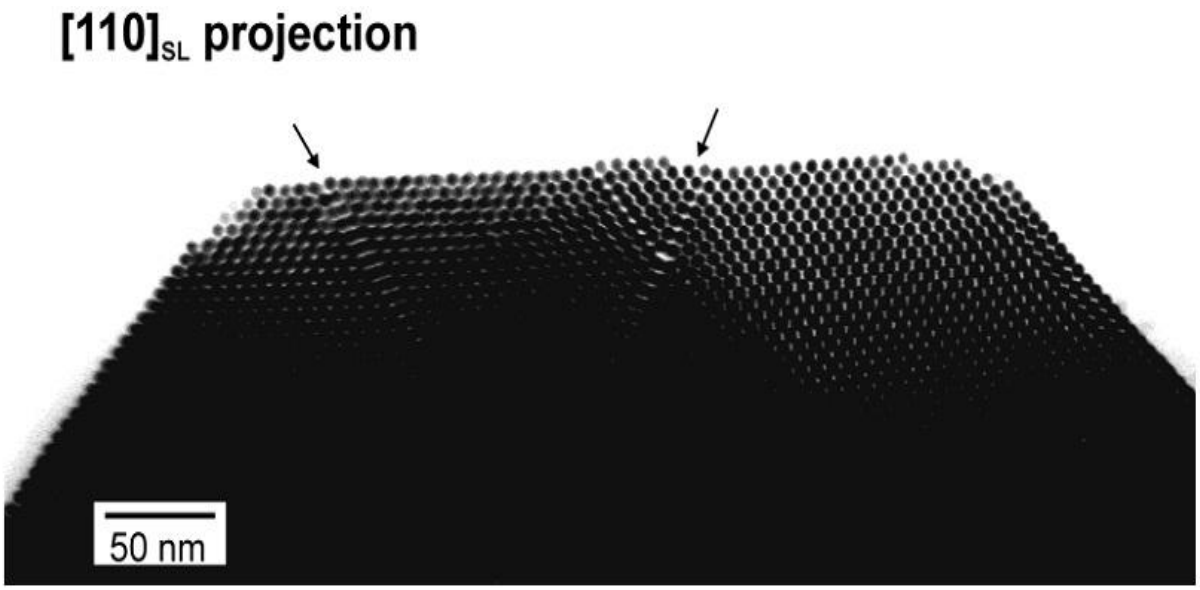

Figure 3.7 TEM micrograph of nanocrystal superlattice of gold nanoparticles prepared by the inverse micelle method **[30]**.

The ligand molecules influence the properties of the gold nanoparticles. The interparticle separation of the gold nanoparticles through the alkyl chain length critically controls their solubility behavior and also leads to the formation of exclusive 2D or 3D superlattices or a combination of them. The propensity to form 3D lattices and their sizes are usually greater in the Au-C_8SH and Au-C_{10}SH cases compared toAu-C_{12}SH. The majority of Au-C_{16}SH colloid forms only 2D monolayers [31]. Theoretical work in our group shows that the depth of the effective interaction potential between two gold nanoparticles becomes shallower as the ligand length is increased [32].

CHAPTER 4 - Light Scattering Theory and Experimental Method

When an electromagnetic wave falls on an object, one may think of the atoms or molecules of that object to absorb and promptly reemit radiations [33,34]. The reemission of radiation can be at the same or different wavelength. Scattering with no change in wavelength is called elastic scattering and otherwise called inelastic scattering [35]. For the scattering technique we describe here, no or negligible change in the wavelengths (elastic or quasi-elastic scattering) is assumed. The superposition of the reemitted electromagnetic waves by all the atoms or molecules of the object forms a distinct scattered intensity pattern [36]. It is possible to extract information on the geometry of the scatterer (size and dimension) from its scattering pattern. From the behavior of evolving scattering pattern we can obtain information on the kinetics of an aggregating system as well.

4.1 Scattering Wave Vector

Let us consider the light scattering at an angle θ upon a small particle at $\vec{r}$ as in Figure 4.1. The incident field with wave vector $\vec{k}_i$ at position $\vec{r}$ is

$$E_i \propto \exp(i\vec{k}_i \cdot \vec{r}) \qquad \textbf{(4.1)}$$

where we keep track of phase information only. The field scatters toward the detector in the direction $\vec{k}_s$, where $\vec{k}_s$ is the scattered wave vector. Thus the field at the detector, at the position $\vec{R}$, is

$$E(R) \propto E_i \exp[i\vec{k}_s \cdot (\vec{R} - \vec{r})] \qquad \textbf{(4.2)}$$

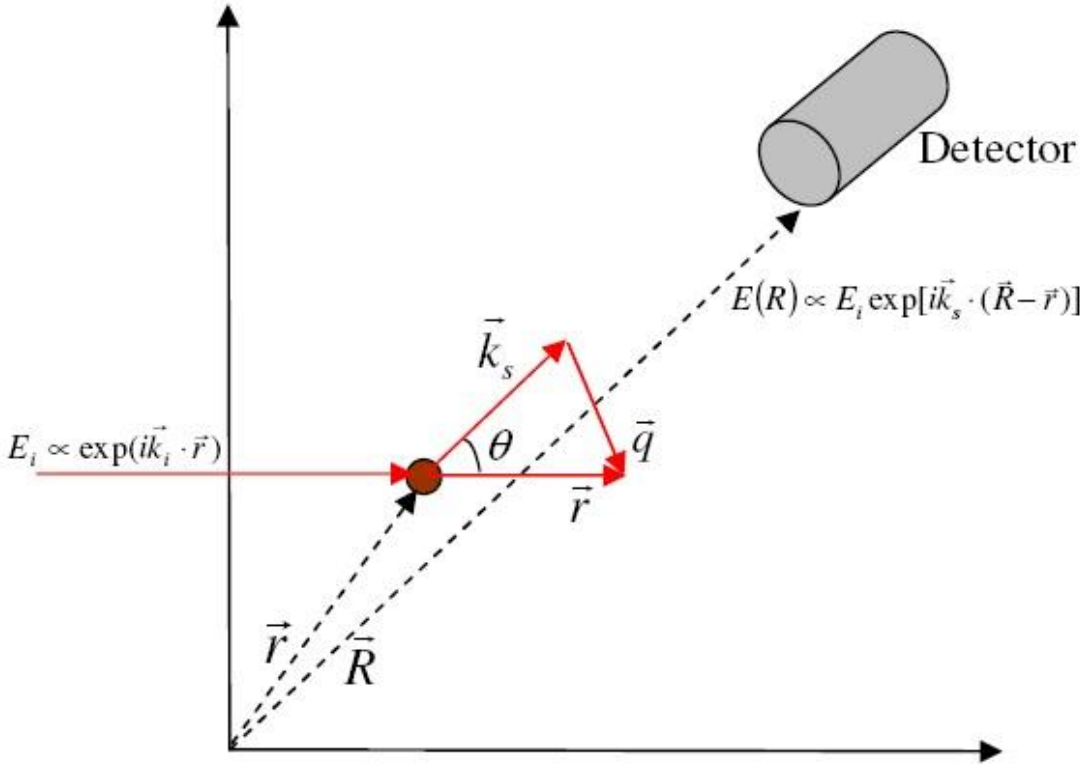

Figure 4.1 The incident field is scattered from a particle at $\vec{r}$ toward the detector at a scattering angle θ. The scattering wave vector is defined as $\vec{q} = \vec{k}_i - \vec{k}_s$.

Substitution equation (4.1) into equation (4.2), we get

$$E(R) \propto \exp(i\vec{k}_s \cdot \vec{R}) \exp[i(\vec{k}_i - \vec{k}_s) \cdot \vec{r}] \qquad \textbf{(4.3)}$$

Define the scattering wave vector $\vec{q}$ as

$$\vec{q} = \vec{k}_i - \vec{k}_s \qquad \textbf{(4.4)}$$

Consider only elastic scattering, hence

$$\left|\vec{k}_i\right| = \left|\vec{k}_s\right| = k \qquad \textbf{(4.5)}$$

The direction of $\vec{q}$ is in the scattering plane from $\vec{k}_s$ to $\vec{k}_i$ as shown in Figure 4.1. The magnitude of $\vec{q}$ can be calculated.

$$q = 2k\sin(\theta/2) = 4\pi\lambda^{-1}\sin(\theta/2) \tag{4.6}$$

where λ is the wavelength of the light.

The second term in equation (4.3) shows that the phase at the detector is a function of the position of the scattering element $\vec{r}$ and the scattering wave vector $\vec{q}$

$$E(R) \propto \exp(i\vec{q}\cdot\vec{r}) \tag{4.7}$$

4.2 Rayleigh Scattering

The scattering of light, or electromagnetic radiation in general, by particles much smaller than the wavelength λ can be explained by Rayleigh scattering theory. The particles are so small that the field to which a particle is exposed is approximately uniform over the region occupied by the particle. Moreover the field inside the particle is uniform as well [33]. To satisfy those conditions, we need

$$\begin{cases} \alpha << 1 \\ m\alpha << 1 \end{cases} \tag{4.8}$$

Here the size parameter α is defined as $\alpha = 2\pi a/\lambda$, a is the characteristic length of the particle, and m is the relative index of refraction of the particle, $m = n_{particle}/n_{medium}$.

In Rayleigh scattering, all elements of the scatterer reradiate in phase. This results in the scattering amplitude to become proportional to the scatterer's volume, and hence the detector detects scattered intensity going as the square of the scatterer's volume. Light scattering by gas

molecules is an example of Rayleigh scattering since gas molecules are far smaller than any wavelength in the light spectrum.

The differential scattering cross section $d\sigma_{scat}/d\Omega$, which is the power scattered per unit solid angle Ω per unit incident intensity I_0, for Rayleigh scattering on the scattering plane is given by

$$\frac{d\sigma_{scat}}{d\Omega} = k^4 a^6 F(m) \tag{4.9}$$

where $F(m)$ is the Lorentz term, defined as

$$F(m) = \left| \frac{m^2 - 1}{m^2 + 2} \right|^2 \tag{4.10}$$

The scattered intensity per unit area of detection is

$$I_{scat} = I_0 \frac{d\sigma_{scat}}{d\Omega} \frac{1}{R^2} \tag{4.11}$$

Thus

$$I_{scat} = \frac{I_0 k^4 a^6 F(m)}{R^2} \tag{4.12}$$

The angular independence of I_{scat} in equation (4.12) indicates isotropic Rayleigh scattering in all direction on the scattering plane. The k^4 factor in equation (4.12) shows a strong dependence in the wavelength λ; smaller wavelengths being scattered a lot more. This briefly explains why sky has blue color in day time.

Considering a case when there is a uniform distribution of *n* scatterers per unit volume, we have the total scattered intensity I_{scat}

$$I_{scat} \propto na^6 = na^3 a^3 \propto (nV_{scat})V_{scat} \tag{4.13}$$

where V_{scat} is the volume of the scatterer. Mass conservation will require nV_{scat} to be constant. Hence we find

$$I_{scat} \infty V_{scat} \tag{4.14}$$

Equation (4.14) shows that the scattered intensity for a system of scatterers is proportional to the volume of each scatterer. If this system is an aggregating system the scattered intensity will increase linearly with the increasing volume of each scatterer. This effect is known as the Tyndall effect.

The total scattering cross section σ_{scat} is obtained by integrating equation (4.9) over whole solid angle. One must include the factor $\sin^2 \phi$ in equation (4.9) to account for the differential scattering cross section at points other than those on the scattering plane. After integration we obtain

$$\sigma_{scat} = \frac{8\pi}{3} k^4 a^6 F(m) \tag{4.15}$$

Besides scattering, particles also absorb a part of the incident radiation if the refractive index has an imaginary part. The absorption cross section of a Rayleigh particle is given as

$$\sigma_{absp} = -4\pi k a^3 E(m) \tag{4.16}$$

where $E(m)$ is the imaginary part of $[(m2 - 1)/(m2 + 2)]$, i.e.,

$$E(m) = \mathrm{Im}\left(\frac{m^2 - 1}{m^2 + 2} \right) \tag{4.17}$$

Real m makes $E(m) = 0$, hence no absorption occurs.

4.3 Dynamic Light Scattering

Dynamic Light Scattering (DLS), also known as Photon Correlation Spectroscopy (PCS) or Light Beating Spectroscopy, is a technique that relies upon temporal fluctuations in the light scattered from an ensemble of particles to determine their motion. This method is also sometimes called quasi-elastic light scattering (QELS) since the scattered wave usually has a very small change in frequency compared to the incident frequency [37].

The scattered light by the particles (scatterers) can undergo either constructive or destructive interference; thus, within this intensity fluctuation, information is contained about particles' movements. Usually the motion is random Brownian diffusion which is quantified by a size dependent diffusion coefficient. The DLS method measures the decay of the temporal fluctuations in the scattered light, which is related to their diffusion which, in turn, is related to their size. Thus a size measurement can be made.

If the particle moves a small distance relative to q^{-1} by the time τ, there is no phase change. Whereas if the particle moves a large distance relative to q^{-1} by the time τ, there is large phase change, and hence there are intensity fluctuations. The scattered field $E(t+\tau)$ will be at random phase comparing to $E(t)$. To obtain the information on the particle dynamics, we can quantify a fluctuating variable by comparing the phase at two different times and average over all these comparisons with a so-called correlation function as the following

$$g^{(1)}(\tau) = \frac{\langle E(t)E^*(t+\tau)\rangle}{\langle E(t)E^*(t)\rangle} \qquad \textbf{(4.18)}$$

where <…> means a time or equivalently, for ergodic medium, an ensemble average. Substitute equation (4.7) into equation (4.18), it reduces to

$$g^{(1)}(\tau) = \left\langle \exp\left\{ i\vec{q} \cdot \left[\vec{r}(t+\tau) - \vec{r}(t) \right] \right\} \right\rangle = \left\langle \exp\left(i\vec{q} \cdot \Delta\vec{r} \right) \right\rangle \tag{4.19}$$

where $\Delta\vec{r} = \vec{r}(t+\tau) - \vec{r}(t)$ is the displacement of the particle in time τ.

In the most common situation the particle moves via random Brownian motion, then the motion with the diffusion constant *D* can be described by the Gaussian probability distribution as

$$P(\Delta\vec{r}, \tau) \propto \exp\left(-\frac{\Delta r^2}{4D\tau} \right) \tag{4.20}$$

The diffusion constant *D* is given by equation (2.39) in section 2.3.2. We also write it here for convenience,

$$D = \frac{k_B T}{6\pi\eta a} \tag{4.21}$$

where k_B is the Boltzmann constant, *T* is the absolute temperature, η is the suspending medium shear viscosity, and *a* is the particle's radius, assumed spherical. Performing the average of equation (4.19) with the probability distribution of equation (4.20), we have

$$g^{(1)}(\tau) = \int_{-\infty}^{\infty} \exp\left(-\frac{\Delta r^2}{4D\tau} \right) \exp\left(i\vec{q} \cdot \Delta\vec{r} \right) d\Delta\vec{r}$$

$$= \exp\left(-Dq^2\tau \right) \tag{4.22}$$

Equation (4.22) says that the scattered field correlation function decays with a decay time of $\frac{1}{Dq^2}$.

In experiment we cannot detect the field strength directly with detectors. Instead we detect the light intensity *I*. So we will measure the correlation function of the scattered intensity. The intensity correlation function is given by

$$g^{(2)}(\tau) = \frac{\langle I(t) I(t+\tau) \rangle}{\langle I(t) \rangle^2} \tag{4.23}$$

The intensity correlation function given in Equation (4.23) is a stationary process meaning that the measurements can be performed at any time and yield the same results. Moreover, $g^{(2)}(\tau)$ should be measured over a sufficiently long time compared with the period of fluctuation to yield reliable information about the dynamical properties about the system. The correlation function $g^{(2)}(\tau)$ is a measure of the similarity between two signals $I(t)$ and $I(t+\tau)$. When $\tau = 0$ these two signals are completely in phase with each other, and $\langle I(t) I(t+\tau) \rangle$ is large; as τ increases, $I(t)$ and $I(t+\tau)$get out of phase with one another, and the correlation function $\langle I(t) I(t+\tau) \rangle$ is small [38]. Thus, it would appear that the correlation function either remains equal to its initial value for all times τ, in which case the intensity *I* is a constant of the motion, or decays from its initial maximum value [38].

$$\langle I(t)^2 \rangle \geq \langle I(t) I(t+\tau) \rangle \tag{4.24}$$

For large times compared to the characteristic time for the fluctuation of intensity, $I(t)$ and $I(t+\tau)$ are expected to become totally uncorrelated [38]; thus,

$$\lim_{T \to \infty} \langle I(t) I(t+\tau) \rangle = \langle I(t) \rangle \langle I(t+\tau) \rangle = \langle I \rangle^2 \tag{4.25}$$

Therefore, the intensity correlation function decays from $\langle I^2 \rangle$ to $\langle I \rangle^2$ (i.e., the background or the noise level). This is shown in Figure 4.2 where *t* is set to zero. The inset of Figure 4.2 shows the time dependence of the scattered intensity which generally resembles a noise pattern.

The Siegart equation [39,40] relates the second order correlation function, equation (4.23), with the first order correlation function, equation (4.18).

$$g^{(2)}(\tau) = B\left(1 + \beta \left| g^{(1)}(\tau) \right|^2 \right) \qquad \textbf{(4.26)}$$

where *B* is the baseline and β is the coherence factor which is an adjustable parameter in the data analysis procedure.

For the Siegart equation to be valid, the scattered electric field must be a Gaussian process [39]. The Siegart equation is violated for cases such as experiments with a small number of particles in the scattering volume, experiments with strongly interacting particles, and scattering from non-ergodic systems such as gels and glasses where the time averaged intensity correlation function of scattered light is different from the ensemble averaged function [39].

For monodisperse particles, $g^{(2)}(\tau)$ is an exponential decay function,

$$g^{(2)}(\tau) = \langle I \rangle^2 + \left(\langle I^2 \rangle - \langle I \rangle^2 \right) \exp\left(-\tau / \tau_c\right) \qquad \textbf{(4.27)}$$

where τ_c is the correlation time of the diffusing particle in the solution. For spherical particles the correlation time is related to the size of particles by

$$\tau_c = \frac{1}{2Dq^2} = \frac{3\eta\lambda^2 a}{16\pi^2 k_B T \sin^2(\theta/2)} \qquad \textbf{(4.28)}$$

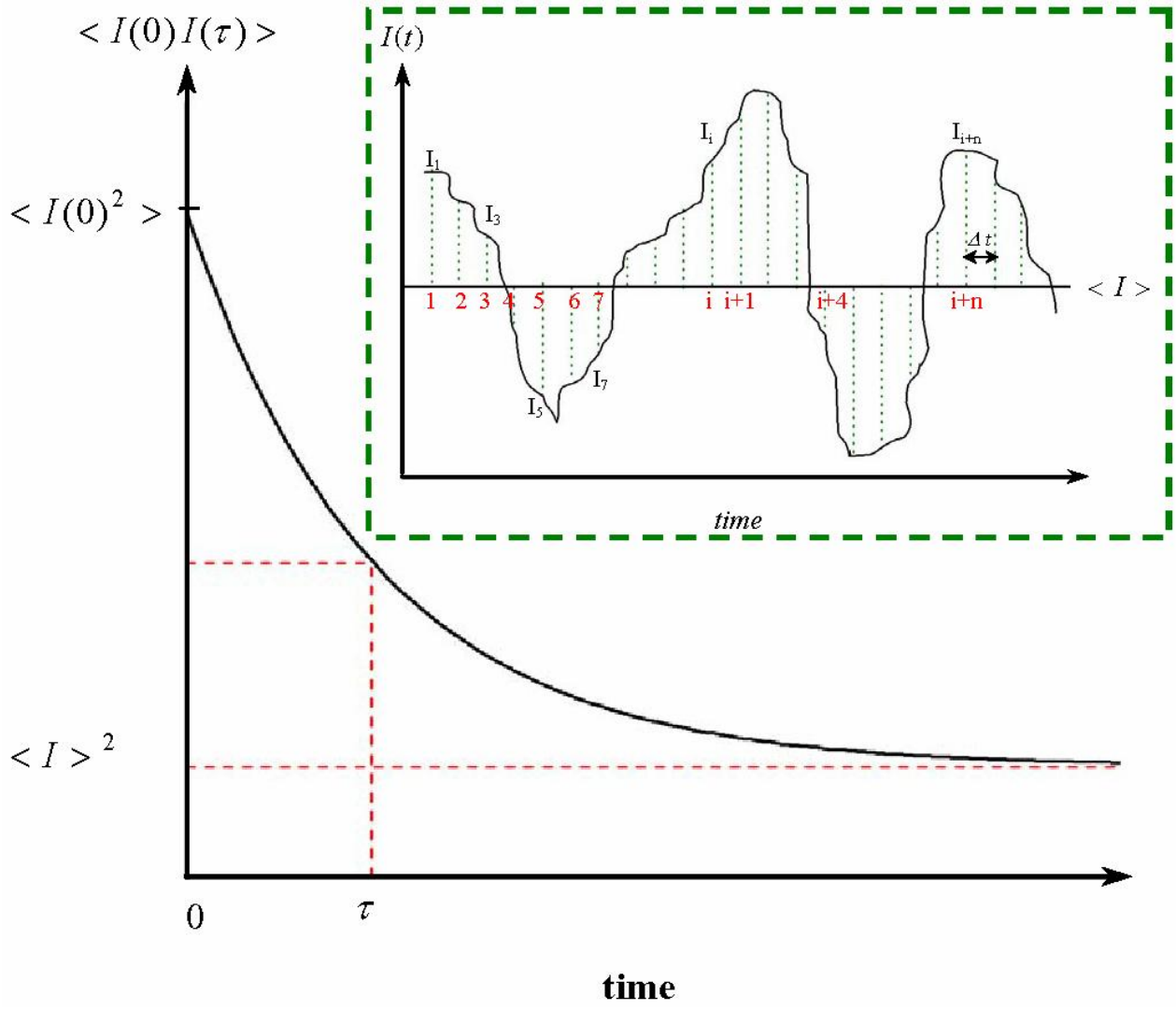

Figure 4.2 The time correlation function $\langle I(0)I(\tau)\rangle$ versus time is plotted. $\langle I(0)I(\tau)\rangle$ decays initially from $\langle I(0)^2\rangle$ to $\langle I\rangle^2$ for times large compared to the correlation time. The inset graph shows the intensity fluctuations (noise pattern) in times. The time axis is divided into discrete time intervals Δt.

At a given q, long correlation time indicates slow diffusion rate and vice versa. Physically, larger scatterers have longer correlation time. By measuring the correlation function $g^{(2)}(\tau)$ and fitting it with equation (4.27) to obtain the correlation time τ_c, we can find the size of scattering particle by

$$a = \frac{16\pi n^2 k_B T \sin^2(\theta/2)}{3\eta\lambda^2} \cdot \tau_c \qquad \textbf{(4.29)}$$

For the convenience of later calculations, here we illuminate all the parameters again: n is the index of refraction of the solution, k_B is the Boltzmann constant, T is the temperature, θ is the scattering angle, η is the viscosity of the solution, λ is the light wavelength and τ_c is the correlation time.

Here we only presented the simplest form; however, the correlation function can have various forms depending on the shape of the particles, polydispersity, absorption, and other parameters [38,39].

In dynamic light scattering the fluctuation in the intensity can be measured via homodyne (self-beating) or heterodyne techniques. In the heterodyne technique, which is much less used in practice, it is the field correlation function, $g^{(1)}(\tau)$, that is measured. This technique involves optical mixing of the scattered light with a ca. 30 times more intense local oscillator (e.g., wall glare) [39]. The field correlation function can also be obtained from the intensity correlation function (Siegart equation). In the homodyne technique, the intensity correlation function is measured via the scattering from the sample.

4.4 Dynamic Light Scattering from Polydisperse Samples

Equation (4.27) is good for a single scatterer or a system of monodisperse scatterer. However, real system is usually characterized by polydispersity in size (and shape) of the scatterers. Hence DLS provides an intensity weighted average decay rate instead of a pure decay rate. The homodyne intensity correlation function for a polydisperse scattering system can thus be given as

$$g^{(2)}(\tau) = A + B\sum_i c_i \exp\left(-\tau / \tau_{ci}\right) \tag{4.30}$$

where $\tau_{ci} = \left(2D_i q^2\right)^{-1}$ is the correlation time for the i^{th} particle in the scattering volume, and the factors A and B represent signal noise and spatial incoherency in the scattered field at the detector. The coefficient c_i is the amplitude of the decay rate for the i^{th} particle such that

$$\sum_i c_i = 1 \tag{4.31}$$

If the scattering system is monodisperse, the plot of $\ln\left\{\left[g^{(2)}(\tau) - A\right]/B\right\}$ versus correlation time τ yields a constant slope of τ_c^{-1}. However, for polydisperse scattering system, this plot is no longer a straight line. The degree of non-linearity of the plot gives a measure of the polydispersity of the scattering system. The summation appearing in equation (4.30) is approximated with a cumulant fit to simplify the fitting of the experimentally measured correlation function [41]. This cumulant fit is given as

$$g^{(2)}(\tau) \approx A + B\exp\left(-\mu_1\tau + \frac{\mu_2}{2}\tau^2\right) \tag{4.32}$$

where μ_n is the n^{th} cumulant given by

$$\mu_n = \lim_{t\to 0}(-1)^n \frac{d^n}{dt^n} \ln\left[g^{(2)}(\tau) - A\right] \tag{4.33}$$

Equation (4.33) gives

$$\mu_1 = \sum_i c_i (1/\tau_{ci}) \tag{4.34}$$

and

$$\mu_2 = \sum_i c_i (1/\tau_{ci})^2 - \left[\sum_i c_i (1/\tau_{ci})\right]^2 \tag{4.35}$$

The second cumulant μ_2 gives a measure of the polydispersity of the system. Equation (4.34) also infers that the first cumulant is the average inverse characteristic correlation time $\langle \tau_c^{-1} \rangle$ for the polydisperse system. If $\langle D \rangle$ be the scattered intensity weighted average diffusion coefficient, we can write

$$\mu_1 = \langle \tau_c^{-1} \rangle = 2q^2 \langle D \rangle \tag{4.36}$$

In the above discussion we assumed translational diffusion of the scatterers is dominant and thus is the only responsible factor for the effective intensity fluctuation. This assumption is good for spherically symmetric particles. Also when q^{-1} is greater than the hydrodynamic radius of the scattering particles, the rotation dynamics will bring negligible phase shift in the scattered field. Hence the assumption is also good for such case. However, for other cases rotational diffusion does produce a significant contribution in the decay rate of the correlation function. The first cumulant given by equation (4.36) gets modified for these cases as

$$\mu_1 = 2\left(q^2 D + D_R\right) \tag{4.37}$$

where $\overline{D}_R$ is the mean rotational diffusion coefficient for the system.

4.5 Equipment Setup

A coherent light source is required for dynamic light scattering. The advent of the laser, as such a source, enabled the technique to be developed in the 1960's. Most common laboratory lasers such as Helium-Neon, argon ion, Nd:YAG, etc have enough coherence to be useful for dynamic light scattering.

Equation (4.27) is for the perfect coherence and the realistic formula in experiments is

$$g^{(2)}(t) = B + A\exp\left(-2Dq^2 t\right) \qquad \textbf{(4.38)}$$

Where A is the signal strength and B is the background. As coherence declines, the signal to noise, A/B, declines. Coherence is a complex topic and will not be discussed here. Standard texts such as Hecht, 1987, or Born and Wolf, 1975 can be consulted. Here it is useful to know that both longitudinal coherence, related to the spectral band width of the light, and transverse coherence are necessary. The former is fixed by the laser you use. The latter is also a strong function of the laser but can be improved by spatial filtering transverse to the direction of the beam. Thus good transverse coherence can be gained if the laser is operating in the TEM_{00} mode (transverse electromagnetic). This mode is characterized by a Gaussian beam profile.

Absorption occurs when the energy of the incident light matches an absorption band of the colloidal particles. Strong absorption induces local heating in the path of the laser beam, which in turn causes a change of optical index of refraction of the medium and a divergence of the beam. A simple method to check the divergence is when this diverging beam passing through the medium is projected onto a screen, a broad interference ring pattern appears in the first few secons. This phenomenon is normally called thermal blooming or thermal lensing effect [42]. A

right wavelength of the laser should be chosen to prevent divergence of the laser beam through the sample in experiment.

From the UV-Vis spectrum of our gold nanoparticles monomers and superclusters ligated with dodecanethiol, Figure 5.3 in section 5.2, the absorbing peaks of our sample are from about 530nm to 550nm. A linear polarized cylindrical Helium-Neon laser with a wavelength of 632.8nm was used in the experiment. The beam diameter of the laser is 0.98mm, the power is 17.0mW and the mode structure is TEM_{00} (>99%).

Figure 4.3 is a picture of the dynamic light scattering experimental apparatus in our lab. The incident beam is narrowed by a convex focusing lens in front of the laser. Laser light scattered from a sample in the sample holder is collected by an imaging lens. This lens forms a real image of the laser beam as it passes through the scatters from the sample onto either an adjustable slit or iris diaphragm (slits are used here because irises rarely close to less than 1 mm). In this way the slit can spatially filter the light and thereby select the portion of the scattering beam to pass on to the detector. Usually the laser beam is horizontal and the slit is vertical, hence the resulting scattering volume is defined in these two directions. An observer can look through the short working distance telescope with the reflex mirror adjusted to a 45^{o} angle and see this image masked by the slit. In this way the observer knows exactly what part of the scattering sample will pass on to the detector when the reflex mirror is lowered out of the path. The detector we used is a photomultiplier amplifier connected with a ALV-5000 multiple tau digital correlator in a computer. The beam is narrowed by the focusing lens in the incident beam so that the slit can be narrower to achieve better coherence on the detector. The entire detection side of

this apparatus can be placed on an optical rail to pivot around the scatterer to different angles, hence different q value.

The dynamic light scattering setup was checked with test experiments. The size of a commercial polystyrene micro sphere-suspension was measured firstly by dynamic light scattering. The correlation function obtained for the polystyrene sample is shown in Figure 4.4. By fitting the data with equation (4.27), the correlation time is $\tau_c = 0.15ms$. Giving the temperature is $T = 19°C$, the viscosity of water is $\eta = 1.027mPa \cdot s$, the refractive index of water is $n = 1.333$, the scattering angle is 90°, and the wavelength of laser is $\lambda = 632.8nm$, we can calculate the radius of the polystyrene from equation (4.29) is 21.9nm, and the radius given by the manufacturer is 21nm.

The temperature of the sample holder is wrapped by a heating tape controlled by a Conductus LTC-10 temperature controller. The range of the temperature variation is from room temperature to 100°C. The sample container is a round glass test tube with a 10 mm diameter. The volume of the sample in the test tube was 1 ml. Sample holder is able to hold several test tubes. More samples at the same temperature can be measured at the same time to speed the experiment.

The characteristic time of the temperature quench for the sample was also measured by a test experiment with polystyrene suspension. One microliter of polystyrene suspension was heated to 65°C, and then put in the sample holder at 25°C. Dynamic light scattering

measurement started immediately. The correlation time changing with time is plotted in Figure 4.5. We can see the characteristic time (1/e) of the temperature quench was about 100 seconds.

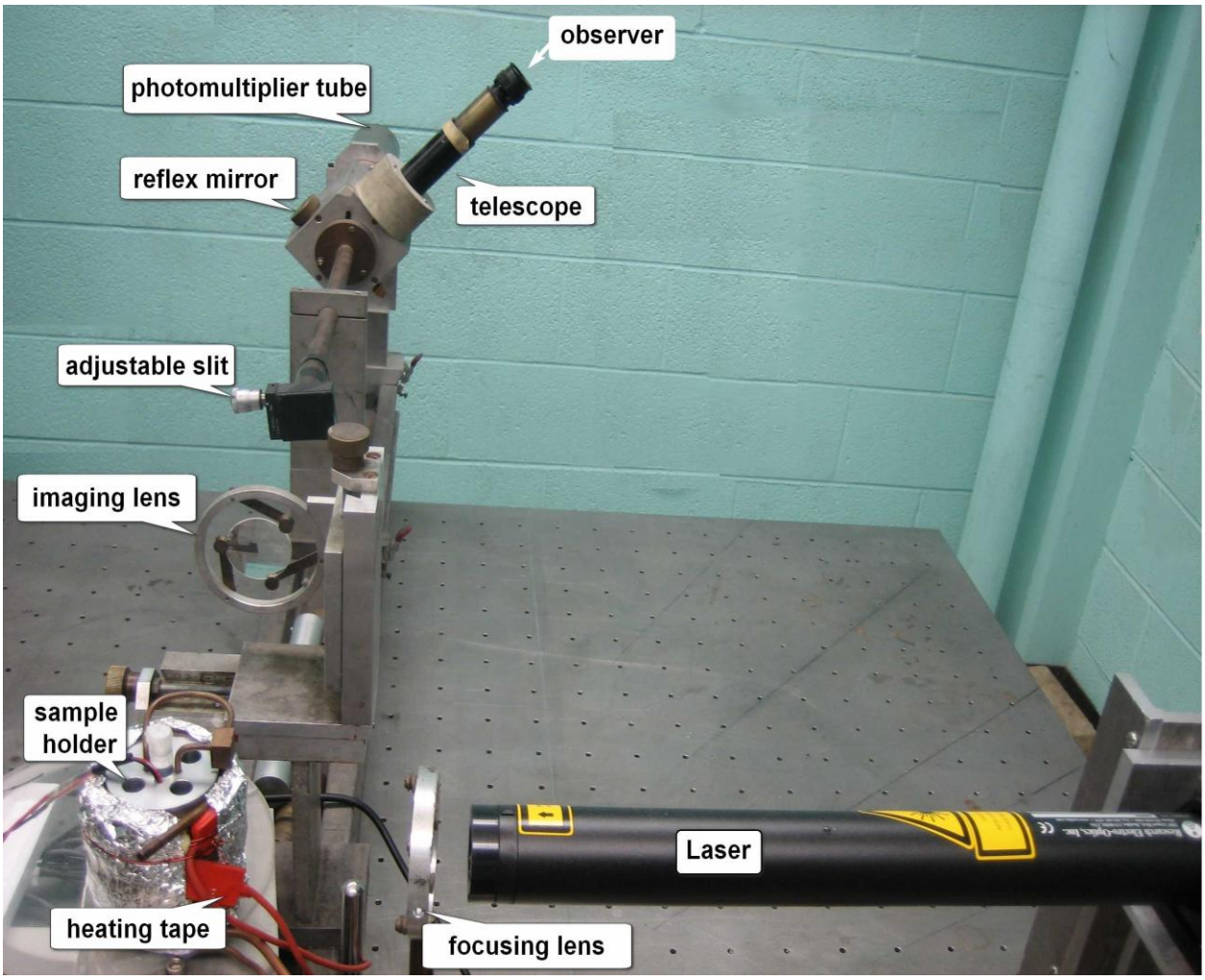

Figure 4.3 Dynamic light scattering apparatus with adjustable slit and telescopic reflex observation and the temperature controllable sample holder.

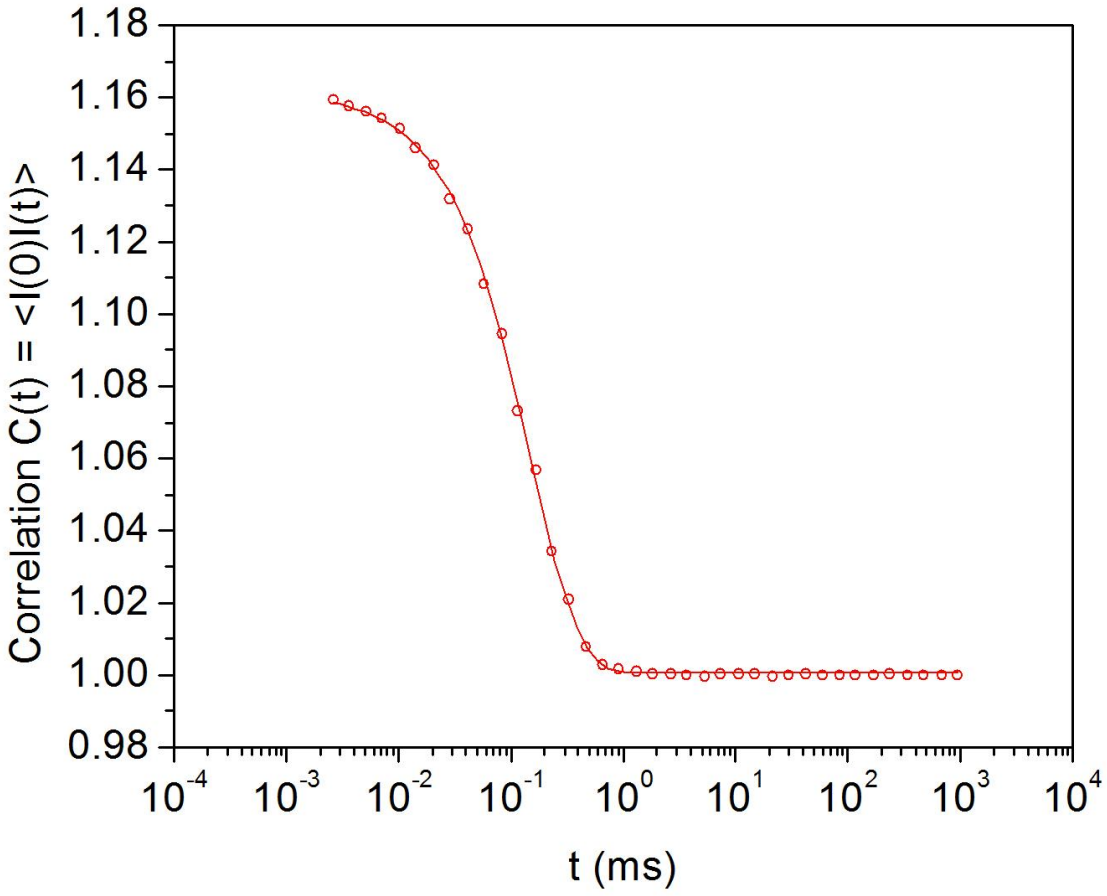

Figure 4.4 Correlation function obtained from a 42nm in diameter commercial polystyrene micro sphere-suspension in water at 19°C

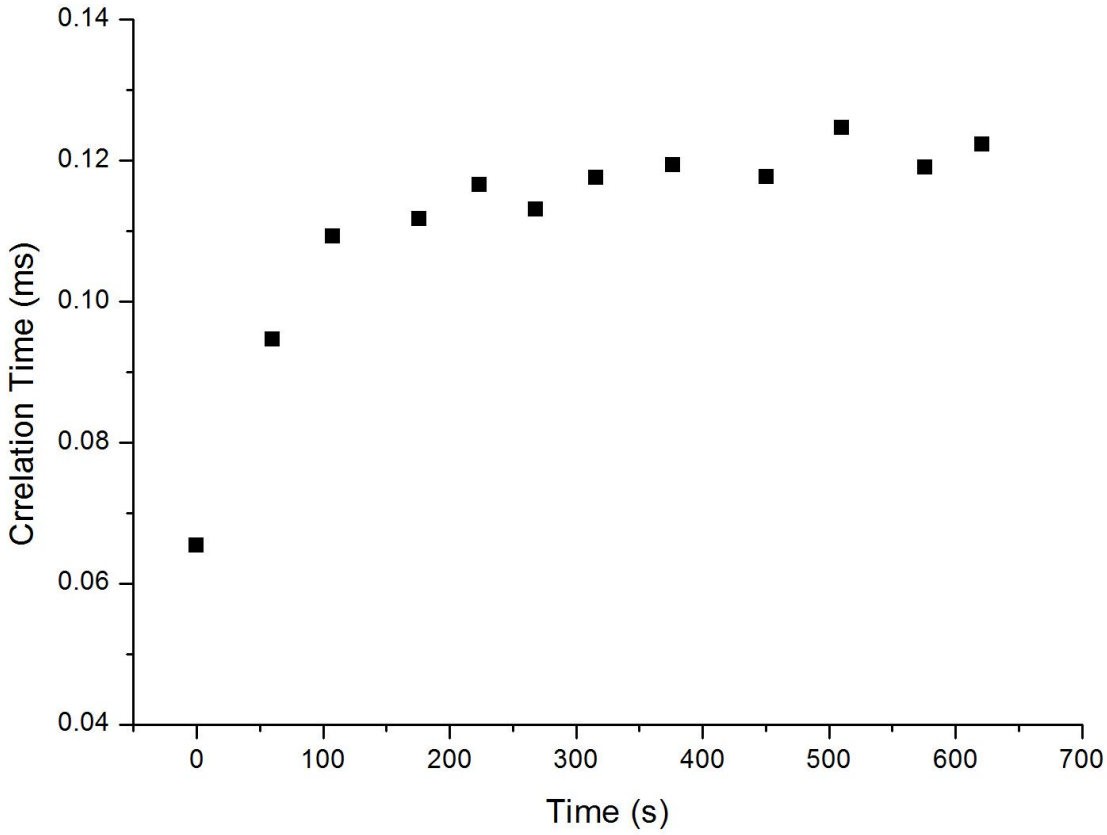

Figure 4.5 The characteristic time of the temperature quench from 65°C to 25°C.

CHAPTER 5 - UV-Visible Spectroscopy

Optical absorption spectroscopy is an important tool to determine the properties of the gold colloidal solution. Gold nanoparticles and aggregations of gold nanoparticles have an intense color which is absent for the bulk gold material or for the individual gold atoms. The absorbance, position and shape of the ultraviolet-visible spectrum were found to depend on many factors such as particles sizes and their distribution, particle shapes, concentrations of gold, refractive index of the solvent, temperature, and etc [43]. The UV-Vis spectroscopy was used in our study to monitor the synthesis process of gold nanoparticles, to observe the degree of gold supercluster formation, and to measure the concentrations of gold colloidal solution.

5.1 Optical Properties of Gold Nanoparticles

The optical response of noble metal nanoparticles is a very unique phenomenon. It is confined to a select number of elements that display free electron behavior in particles under 100 nm in size. Despite these restrictions this property has been utilized for hundreds of years as the coloration of decorative glasses. Scientific study of this phenomenon was first accomplished by Michael Faraday at the turn of the 19^{th} century as he attributed this optical response to small gold clusters in solution [44]. Mie was the first to investigate the origin of these colors mathematically as he solved Maxwell's equations of light for small spherical particles of metal [45]. These calculations are widely used today to predict the absorbance features of various metal particles, and mimics experimental observations very closely.

The absorption of light in this instance is typically termed a surface plasmon resonance (SPR). The phenomenon is described as the response of the electron gas (free electrons in a metal particle) to the presence of an electromagnetic wave in the vicinity of the particles [45-48]. This wave of light causes an oscillation of the free electrons. The frequency of oscillation is determined by the density of electrons, the effective electron mass, and the shape and size of the charge distribution. This translates into a very product specific property. The absorption will be dependent on the specific characteristics and the local environment of the particle.

As the size of the particle is increased a greater number of electrons are involved, and will have lesser displacement from the nuclear framework. If the shape of the particle is altered from spherical there will be separate responses of the electrons for different directions of electron oscillation. When the composition of a metal particle is altered, once again the free electrons will have a different affinity for the particle and will also cause a shift the position of λ-max. Likewise for particles with heterogeneous compositions (more than one metal domain), a complex spectra will be observed.

The optical response of the particles is also very sensitive to its surroundings. The absorbance is highly dependent on the refractive index of the solution, which is amplified for molecules very near, or bonded to the surface of the metal particle. Exciting new sensor devices have been developed using this property allowing detection of numerous entities including protein recognition. Binding of molecules to the nanoparticles will have an added effect based on the electron donation/withdrawing properties of the bonded functional group affecting the conduction electrons.

Experimentally the SPR is found to be dependent on the size, shape, and environment of the particles. It can therefore be used as a gauge of the size dispersity of the particles in solution. A strong narrow absorption is representative of very similar particles, while a broad, weaker band will be the result of the contribution of many particles over a large size distribution. The SPR may also be used as an indicator of the size of the particles, as long as the composition of the nanoparticle is held constant. A blue shift of the peak maximum generally denotes a smaller particle size.

UV-Vis spectra of gold colloidal solution with dodecanethiol ligands before and after digestive ripening are given in Figure 5.1. The UV-Vis peak is considerably narrower after digestive ripened, which reflects the greatly reduced size distribution that occurs during this process. The UV-Vis peak is also getting stronger. The probable reason is that more and more gold nanoparticles are dissolved from the precipitate. The digestively ripened solution has a plasmon peak maximum at 530nm. This band is due to plasmon absorption of single dispersed Au particles with sizes about 5nm in solution as determined by TEM, shown in Figure 3.5.

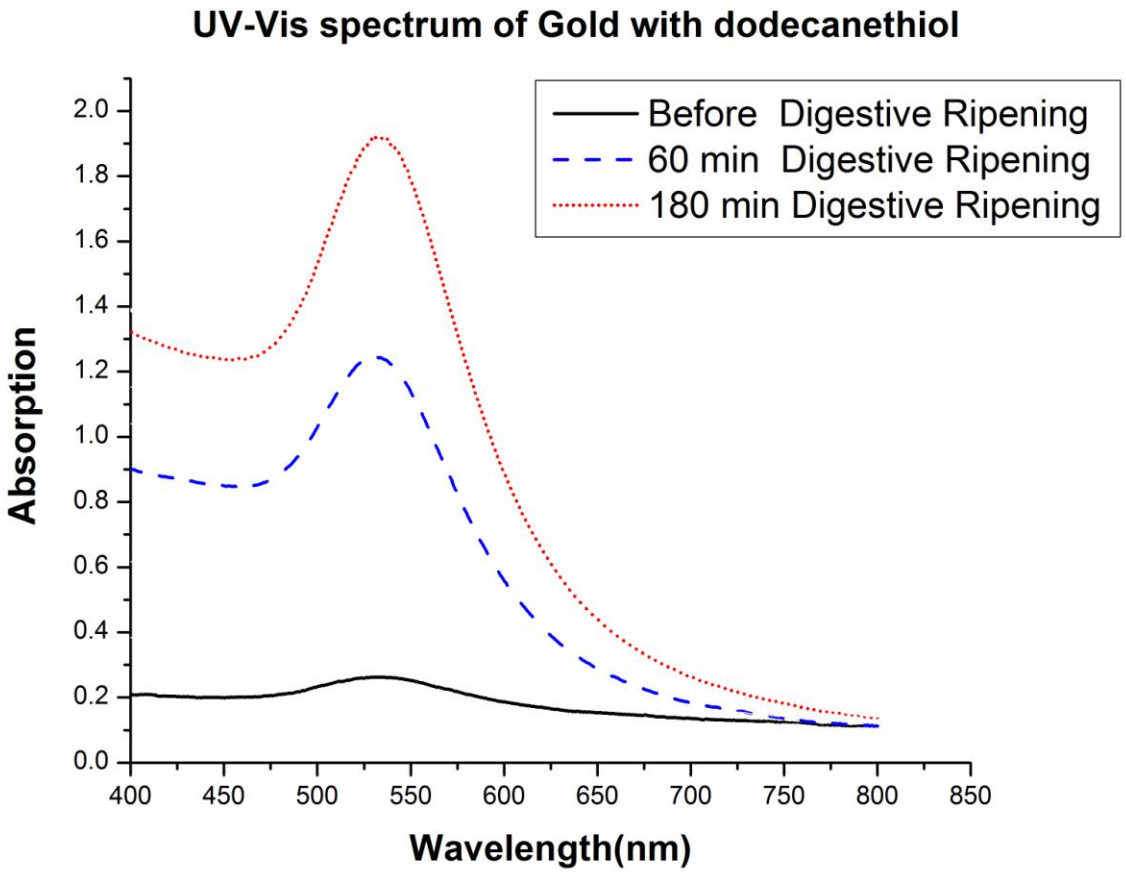

Figure 5.1 UV-Vis spectrum of $AuC_{12}SH$ before and after digestive ripening **[29]**.

5.2 Supercluster Formation

We discussed the formation of supercluster in section 3.2. One obvious phenomenon of the supercluster formation process is the color changing from red-wine color to purple, see Figure 5.2. That implies UV-Vis spectroscopy is also a good method to monitor the monomer-supercluster phase transition of gold nanoparticles.

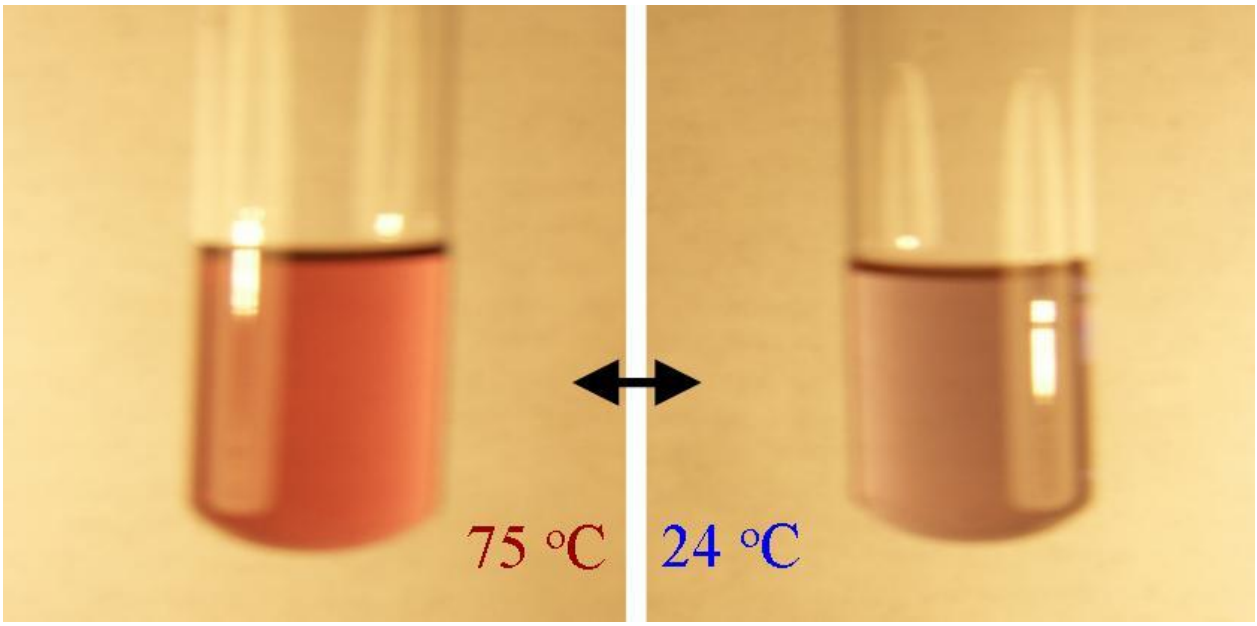

Figure 5.2 Reversible monomer-supercluster phase transition of gold-dodecanethiol in the mixture of t-butyl toluene and 2-butanone by changing the sample temperature.

Figure 5.3 shows a typical UV-Vis spectrum of a system proceeding a supercluster formation. Au-$C_{12}SH$ nanoparticles were dissolved in a mixture of 64%butanone and 36%t-butyltoluene at 72°C. The narrow plasmon peak and the peak position at 72°C indicate the particles were monodisperse and they were all monomers. The system was in one-phase regime at that temperature. When the temperature was cooled, the UV-Vis peak was shifted to a larger

wavelength and a shoulder was arising, which means the monomers were aggregating and forming the superclusters. The peak also became broader because the superclusters formed from monomers were no more so monodisperse.

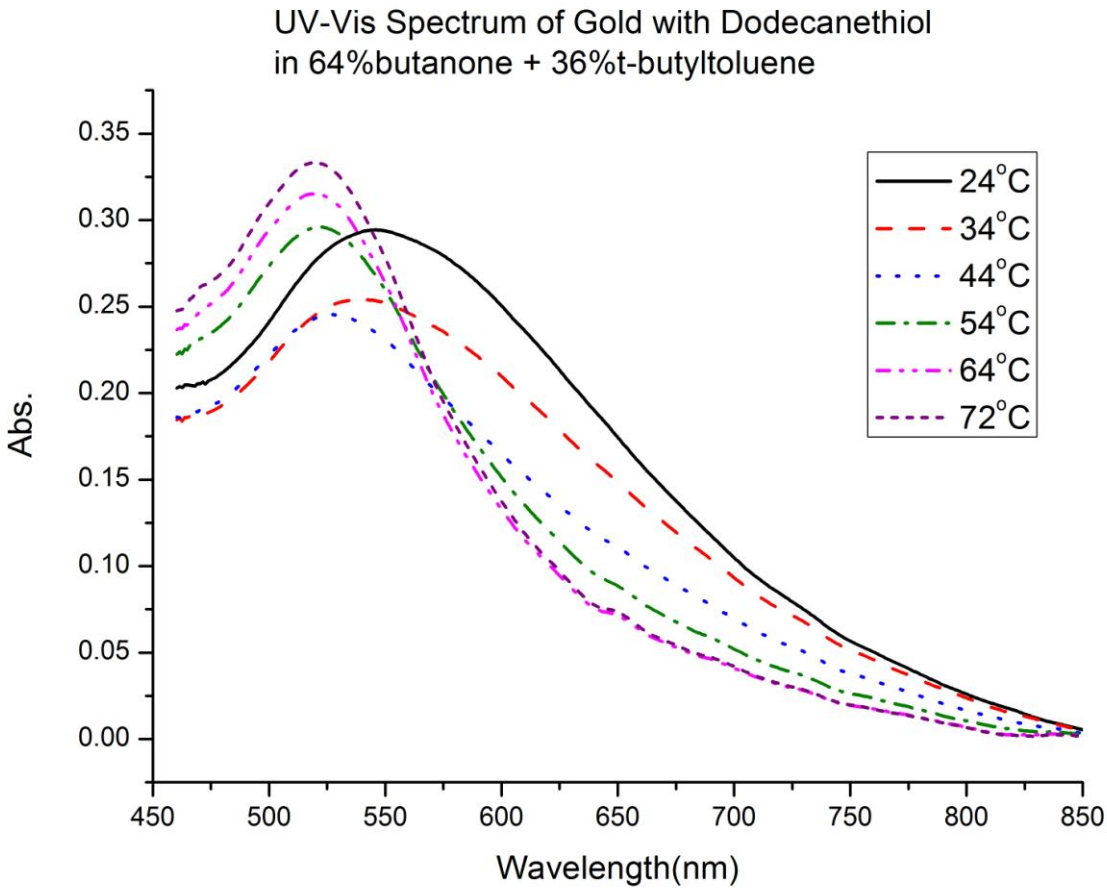

Figure 5.3 UV-Vis spectrum of gold with dodecanethiol in 64%butanone+36%t-butyltoluene cooled from 72°C to 24°C.

5.3 Concentration Measurement

The UV-Vis spectroscopy is often used in a quantitative way to determine concentrations of an absorbing species in solution by using the Beer-Lambert law. The Beer-Lambert Law in optics gives the relation between the absorption of light and the concentrations of the material through which the light is traveling. When a system is in a two-phase state, the UV-Vis spectrum will be a mixing effect from both phases. We can use centrifugation to separate them and measure the concentration of the sample in one-phase.

5.3.1 Beer–Lambert law

The Beer-Lambert Law states that the transmissivity T of light through a liquid material, defined by the ratio of the intensity I of the transmission light and the intensity I_0 of incident light, depends on the distance L the light travels through the liquid material and the absorption coefficient α as

$$T = \frac{I}{I_0} = e^{-\alpha \cdot L} \tag{5.1}$$

The absorption coefficient α can be written as a product of the molar absorptivity ε of the absorber and the molar concentration c of absorbing species in the material, $\alpha = \varepsilon \cdot c$.

The transmissivity is expressed in terms of an absorbance which for liquids is defined as

$$A = -\ln T \tag{5.2}$$

So the absorbance is linear with the concentration according to

$$A = \varepsilon L c \tag{5.3}$$

The molar absorptivity coefficient ε is a fundamental particle property in a given solvent, at a particular temperature and pressure. As long as we keep the molar absorptivity coefficient ε and

the path length L constants, we can determine the concentration of a solution with the simple linear relationship by measuring the absorbance A.

5.3.2 Settling Velocity of Gold Superclusters

To obtain the concentration of gold monomers in a monomers-superclusters co-existing sample, i.e., a sample in the two-phase regime, the sample must be centrifuged to separate monomers from superclusters. Then the supernatant sample containing the monomers was measured with UV-Vis spectrophotometer. The centrifuging time was determined by the settling velocity of particles.

If the particles are falling in the viscous fluid by their own weight due to gravity, then a terminal velocity, also known as the settling velocity, is reached when this frictional force combined with the buoyant force exactly balance the gravitational force. The resulting settling velocity (or terminal velocity) can be derived from Stokes' Law [49].

The weight for the particle is

$$G = \frac{4\pi}{3} r^3 \rho_p g \qquad \textbf{(5.4)}$$

where r is the radius of the particle, ρ_p is the density of the particle and g is the gravity acceleration. And the buoyancy on the particle is

$$F = \frac{4\pi}{3} r^3 \rho_l g \qquad \textbf{(5.5)}$$

where ρ_l is the density of the fluid. The Stokes' Law gives the frictional force exerted on spherical objects with very small Reynolds numbers (e.g., very small particles) in a continuous viscous fluid as [50]

$$f = 6\pi\eta r v \tag{5.6}$$

where η is the viscosity of the fluid and v is terminal velocity. When the particle achieves the terminal velocity, the net force on the particle should be zero, i.e.

$$\frac{4\pi}{3} r^3 \rho_p g - \frac{4\pi}{3} r^3 \rho_l g - 6\pi\eta r v = 0 \tag{5.7}$$

Rearrange equation (5.7) we have

$$v = \frac{2}{9} \frac{(\rho_p - \rho_l) g r^2}{\eta} \tag{5.8}$$

The Relative Centrifugal Force (RCF in 'g's) replaces the gravity acceleration when the sample is being centrifuged. The radius of particles can be obtained with the dynamic light scattering method as discussed in the light scattering chapter. The mass density of gold superclusters can be computed by assuming the gold cores in monomers have the mass density of bulk gold and the superclusters have FCC superlattice structure as discussed in section 3.2.

5.4 Equipment setup

Temperature controlling is the most delicate part in the monomer-supercluster phase transition experiment. To keep the temperature stable during the UV-Vis measurement and to change the temperature quickly when it is needed, a temperature controllable work chamber was designed and made, see Figure 5.4. The chamber was thermally isolated from surrounding by foam plastic. The rotor of a Thermo Scienfific Sorvall Legend 14 Centrifuge was raised up and placed in the chamber. A SpectraSuite UV-Vis Spectrometer was used in the experiment. The

sample holder for UV-Vis measurement was also placed in the chamber and connected with the spectrometer with two optics fiber. Copper tubes coiled round the rotor and the sample holder. An Endocal Refrigerated Circulating Bath pumped the antifreeze coolant fluid at a specified temperature to run through the copper tubes. The range of temperature variation of the circulating bath was from -10°C to 100°C. Two thermocouples, attached on the sample holder and the rotor, were used to monitor the temperatures. When the centrifuge was turned on, the rotating rotor could stir the air in the chamber to an equilibrium temperature rapidly.

The sample was prepared at high temperature (e.g. 65°C) in another temperature controlled sample holder. Then the sample was quenched to a certain temperature, same as pre-set temperature of the chamber. The gold nanoparticles started to aggregate and form superclusters, checked with light scattering. Then we transferred the sample into the cuvette in the centrifuge rotor and centrifuged it. The centrifuging time was calculated by the settling velocity of gold superclusters. The next step is loading the supernatant into a Starna Quartz Micro Cell of 10mm path length in the sample holder. Absorbance data were taken three times consecutively per sample.

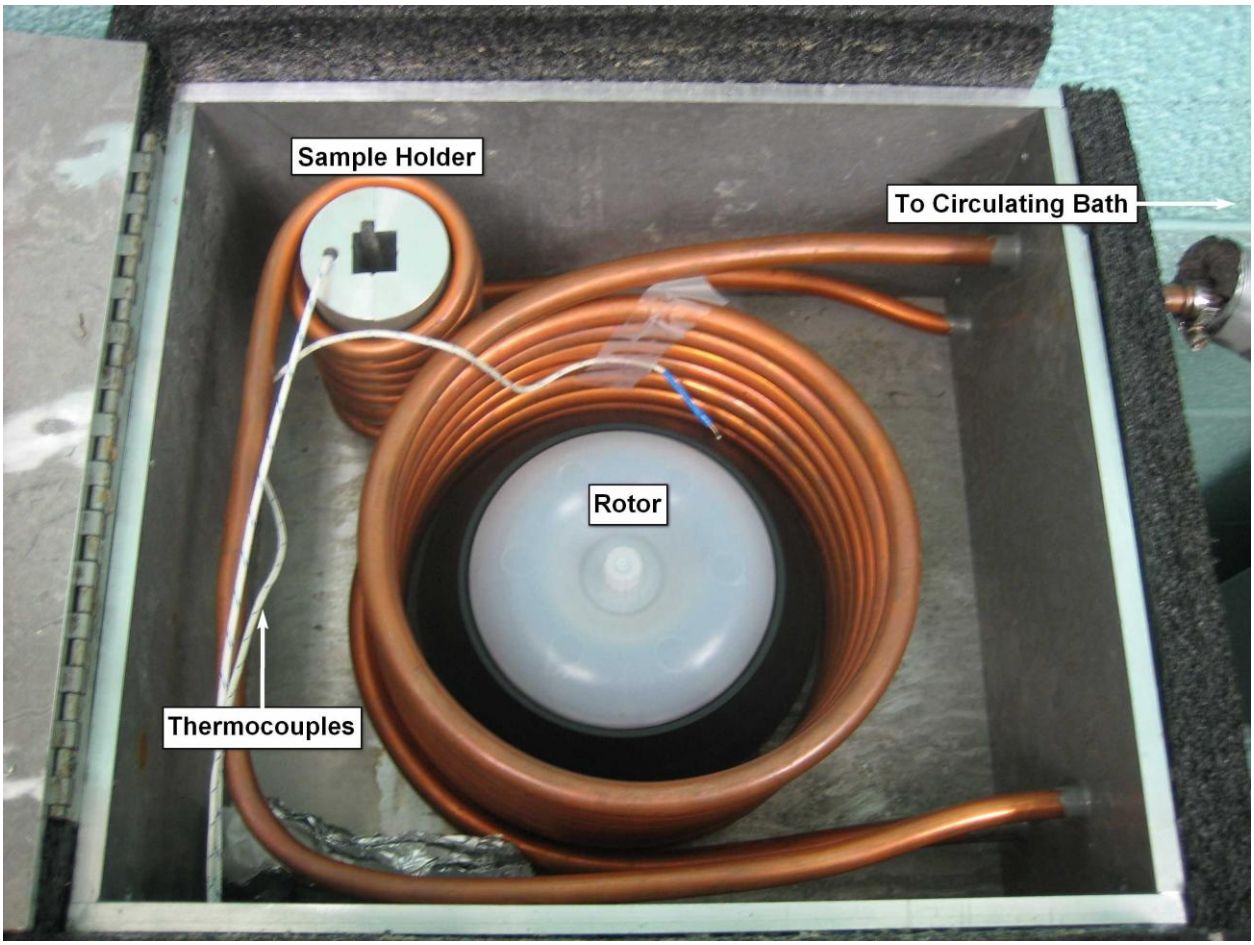

Figure 5.4 The temperature controllable chamber, used for concentration measurement.

CHAPTER 6 - Solubility Phase Diagram of Gold Nanoparticles

6.1 Introduction

Nanoparticles can assembly into very interesting and applicable structures when the interactions between nanoparticles are at the level of a few times the average thermal energy in the system such that the particles can sample an ensemble of states [51]. Suspensions display phase behavior similar to that seen in molecular solution systems after the system reaches an equilibrium state [52]. The phases in the system can be manipulated through the interactions between the solute particles and the interactions between the solutes and the solvents. The dispersed/aggregated phase transitions referred to as fluid/crystal transitions. To describe phase transitions, the thermodynamic variables used in single component molecular systems are density, temperature, and pressure. However, the variables are density, temperature, concentration, and strength of interaction in colloidal systems. Hence the phase diagram of a solution or a colloidal solution can be plotted in temperature vs. concentration as shown in Figure 6.1. The strength of interaction distinguishes colloidal suspensions most strongly from molecular systems. For example, because the strength of interaction can be tuned by solution properties, at fixed temperature, one can map out an entire phase diagram [52]. As the range and strength of attractions and repulsions can be varied over an enormous range with colloidal particles, suspensions of nanoparticles offer a unique test bed for treatments of molecular phase behavior.

Our weakly interacting nanoparticles have the interactions on the order of thermal energy [31]. That means our nanoparticle systems can sample an ensemble of states and are subject to undergoing phase transitions. The discussion in section 3.2 and section 5.2 showed that our gold nanoparticles could form superclusters when they were quenched from a dispersed phase at a high temperature. Those phase transitions were thermally reversible. The superclusters would redissolve to nanoparticles monomers when the temperature was increased.

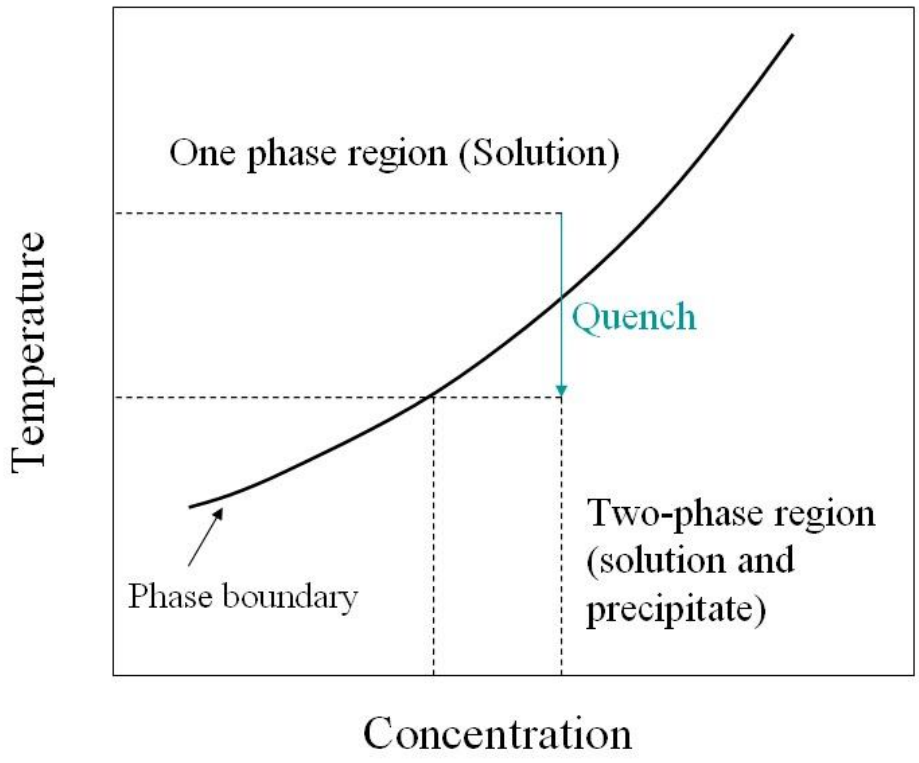

Figure 6.1 Phase diagram and the solubility phase transition of a solution or a colloidal solution

In this chapter, we will describe our work on the solubility phase diagrams of gold nanoparticles ligated with dodecanethiol, decanethiol, and octanethiol in the mixture of toluene

(or t-butyl toluene) and 2-butanone were obtained with UV-Vis spectroscopy. The classical ideal solution theory and regular solution theory will be used to analysis the phase diagrams.

6.2 Experimental Methods

The entire solubility measurement process has the following steps,

1) A highly concentrated (the concentration was known) sample of gold nanoparticles in toluene (or t-butyl toluene) was mixed with a mixture of toluene (or t-butyl toluene) and 2-butanone which was preheated to a high temperature (e.g. 65°C) at which the nanoparticles stay in monomers state checked by dynamic light scattering.
2) The sample was kept at high temperature for the brief time then was quenched to lower temperatures (e.g. 24°C).
3) The in situ measurement with dynamic light scattering of the quenched sample started immediately untill both the intensity of the scattered light and the size of superclusters stopped increasing, which means the system came to a monomers-superclusters co-existing equilibrium state.
4) The sample was transferred to a centrifuge cuvette at the same temperature (e.g. 24°C) and was centrifuged. The centrifuge time was calculated as described below.
5) The supernatant of the sample was transferred to a quartz UV-Vis cell at the sample temperature and the absorbance of the supernatant was measured.
6) The absorbance was converted to concentration. That concentration is the solubility of that gold nanoparticles sample in that solvent at that temperature.

6.2.1 Calibration of Concentration

The relationship between the concentration and the absorbance for our gold monomers was measured by our cooperator Ben Scott [53], shown in Figure 6.2. As we discussed before, Beer's Law is a linear relationship of absorbance with increasing solution concentration. However, as the system's turbidity increases the linear relationship breaks down. Figure 6.2 illustrates this phenomenon at concentrations greater than $1.5\times10^{-3} mol/L$. So the linear relationship from the calibration data is valid for concentrations up to $1.5\times10^{-3} mol/L$, and for absorbances up to about 2.5. The absorbances in our study are clearly in that linear range of validity. The fitted linear equation from Ben Scott's data is

$$c = \frac{Abs_{Ben} + 0.027}{1719} mol/L = 0.115 Abs_{Ben} + 3.09\times10^{-3} mg/mL \qquad (6.1)$$

Even for a same sample, the absorbance measured with Ben Scott's UV-Vis spectrometer was different from the absorbance measured with our UV-Vis spectrometer because of the varied light path length and the experimental error. A correlation equation between those absorbances was obtained by a calibration experiment.

$$Abs = 1.17 Abs_{ben} + 2.27\times10^{-2} \qquad \textbf{(6.2)}$$

Substitute (6.2) into (6.1), we have the linear relation between concentration and absorbance of our gold nanoparticle monomers

$$c = 9.79\times10^{-2} Abs + 5.32\times10^{-3} (mg/mL) \qquad \textbf{(6.3)}$$

After each gold nanoparticle colloidal solution was prepared with digestive ripening process, the stock concentration was measured with above equation.

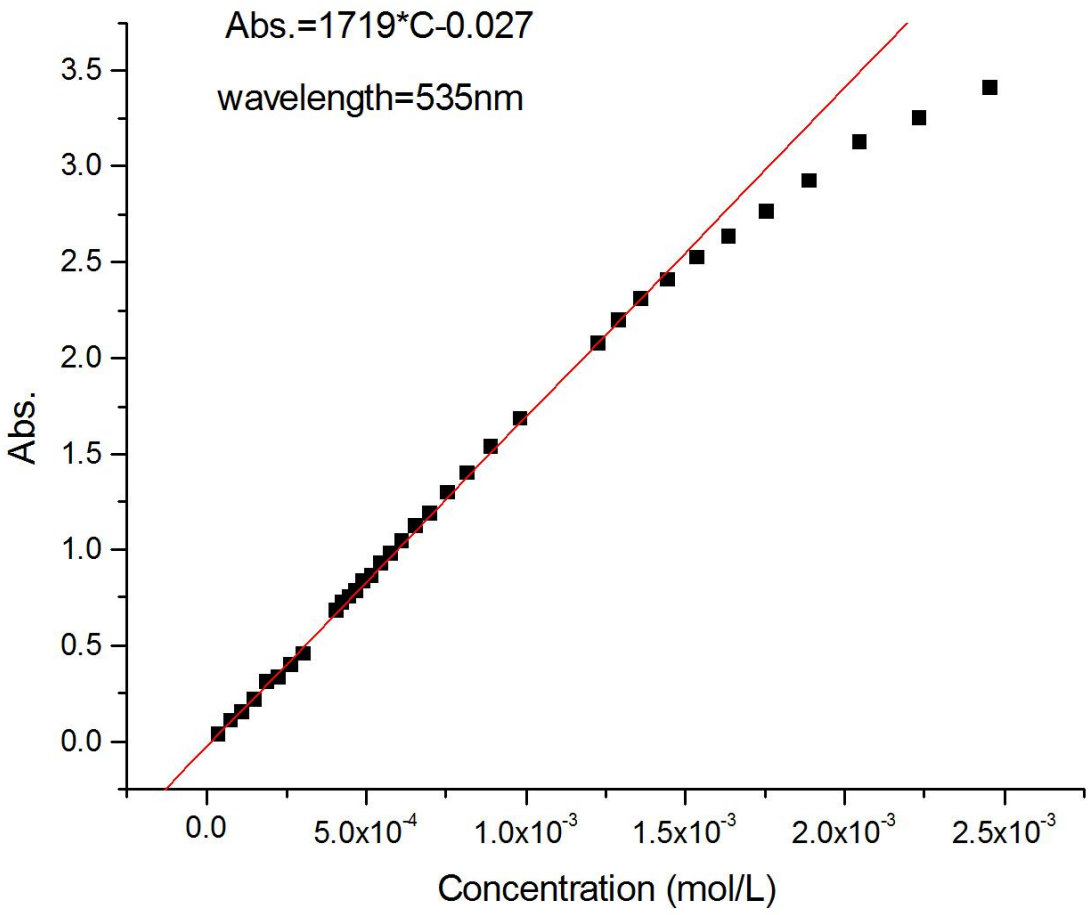

Figure 6.2 Calibration curve for absorbance and concentration in mol Au atoms/L **[53]**.

6.2.2 Settling Velocity of Gold Superclusters

The settling velocity of gold superclusters must be estimated before we set the centrifuge time. The calculation formula was given in equation (5.8). Here we just give a typical example of gold supercluster ligated with dodecanethiol.

The diameter of the gold core in one Au-$C_{12}SH$ nanoparticle is 4.9nm, measured by TEM picture. With twice the dodecanethiol ligand length, which is 1.7 nm, added, the total diameter of a gold-$C_{12}SH$ nanoparticle is 8.3nm.

The atomic radius of gold is 0.144nm, and the crystal structure of gold is FCC lattice, so the volume of each gold atom in the lattice is

$$v = \frac{d^3}{\sqrt{2}} = \frac{(2*0.144)^3}{\sqrt{2}} = 0.0169nm^3 \quad \textbf{(6.4)}$$

So the number of gold atoms in a gold-$C_{12}SH$ nanoparticle is

$$N_{Au} = \frac{\pi(4.9nm)^3/6}{0.0169nm^3} = 3645 \quad \textbf{(6.5)}$$

The ligands ligated on the gold core have a surface density of 21.5Å^2 per chain [32,54]. So the number of ligands on a gold nanoparticle surface is

$$N_{ligand} = \frac{\pi(4.9nm)^2}{0.215nm^2} = 351 \quad \textbf{(6.6)}$$

The atomic weight of gold is $197g/mol$ and the molecular weight of $C_{12}SH$ is $202g/mol$. The mass of a nanoparticle is

$$m = \frac{(3645\times197 + 351\times202)g/mol}{6.02\times10^{23}mol^{-1}} = 1.31\times10^{-18}g \quad \textbf{(6.7)}$$

As discussed in section 3.2, we can assume the supercluster also has the FCC lattice super-crystal structure, and then the volume occupied by one nanoparticle in the supercluster is (not the volume of one free nanoparticle)

$$V = \frac{D^3}{\sqrt{2}} = \frac{(8.3nm)^3}{\sqrt{2}} = 404nm^3 \tag{6.8}$$

So the mass density of the supercluster is

$$\rho_p = \frac{m}{V} = \frac{1.31\times10^{-18}g}{404nm^3} = 3.24g/cm^3 \tag{6.9}$$

For pure butanone solvent, the mass density is $\rho_l = 0.805g/cm^3$, and the viscosity is $\eta = 0.4054\times10^{-3}Pa\cdot s$. Substitute the densities and the viscosity into equation (5.8), we have the settling velocity of the $AuC_{12}SH$ superclusters

$$\begin{aligned} v &= \frac{2(\rho_p - \rho_l)gr^2}{9\eta} \\ &= \frac{2\times(3.24-0.805)g/cm^3\times9.8N/kg}{9\times0.4054\times10^{-3}Pa\cdot s}\cdot r^2 \\ &= 1.31\times10^7 m^{-1}s^{-1}\cdot r^2 \\ &= 4.72\times10^{-6}cm/hr\cdot(r/nm)^2 \end{aligned} \tag{6.10}$$

The settling velocity (in cm/hour) depending on the radius of supercluster (in nm) is plotted in Figure 6.3. When the sample is centrifuged with the $RCF = 14500g$, the settling velocity equals 14500 times the settling velocity in Figure 6.3 consequently. Typically, the radius of superclusters is about 200nm, measured with dynamic light scattering. Hence the settling velocity of superclusters is

$$14500\times4.72\times10^{-6}cm/hr\times200^2 = 0.76cm/s \tag{6.11}$$

The radius of nanoparticles monomers is 4.15nm, hence the settling velocity of monomers is

$$14500\times4.72\times10^{-6}cm/hour\times4.15^2 = 1.18cm/hour \tag{6.12}$$

The typical height of our sample in the centrifugal cuvette is about 1cm. So it takes a few seconds to precipitate the superclusters and about one hour to precipitate the monomers. We

usually centrifuged our samples five minutes to separate the superclusters from the monomers before the UV-Vis measurements.

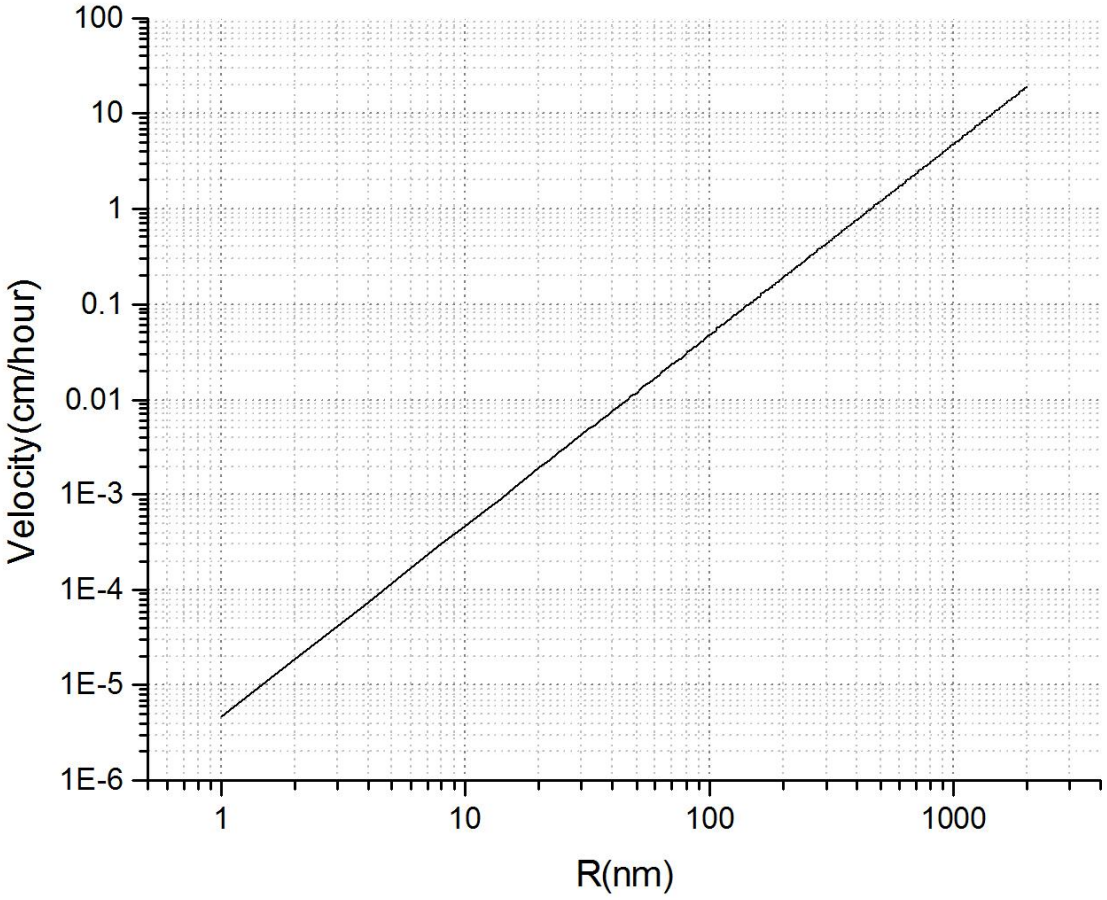

Figure 6.3 Settling Velocity of Au-C12SH superclusters in 2-butanone

6.3 Results and Discussions

Three types of gold nanoparticles were used in our work. They are ligated with dodecanethiol, decanethiol and octanethiol individually. For gold nanoparticles ligated with dodecanethiol, we synthesized them in two kinds of solvent, t-butyl toluene and toluene. All gold nanoparticles ligated with decanethiol and octanethiol were synthesized to disperse in toluene.

6.3.1 Gold Nanoparticles in Mixtures of t-butyl Toluene and 2-butanone

The concentration of stock $AuC_{12}SH$ in t-butyl toluene colloidal solution was measured with UV-Vis spectrometer and a TEM picture was taken as shown in Figure 3.5. The concentration of stock colloidal solution is 0.893mg/ml.

To adjust the phase transition temperature to an experimental accessible temperature, a bad solvent, 2-butanone, was added to the colloidal solution. Experiment showed that t-butyl toluene and 2-butanone are totally miscible. Mixtures with different ratios of t-butyl toluene and 2-butanone were tried. The result we show here is for the solvent of 4% t-butyl toluene and 96% 2-butanone.

960 micro liters of 2-butanone were preheated at 65°C, where the resulting systems were one phase, 40 microliters of stock $AuC_{12}SH$ in t-butyl toluene colloidal solutions were then mixed. The samples were kept there for the brief time before they were quenched to lower temperatures.

After the samples were quenched to lower temperatures and the light scattering experiments were done. The solutions were centrifuged at 300 g at the quenched temperature for 15 minutes. This time is about an order of magnitude greater than the settling time indicated by the Stokes drag calculation of settling velocities for the superclusters. Then the concentrations of the supernatants were measured with UV-Vis measurements. Moreover, subsequent UV-Vis measurements at longer centrifuge times showed no further spectrum change indicating that all the precipitate was at the bottom. The concentrations of the supernatants, i.e., the solubilities of $AuC_{12}SH$ particles in 4% t-butyl toluene and 96% 2-butanone were plotted in Figure 6.4. The linear fitted line in Figure 6.4 is

$$c(\mu g / mL) = (T(^{\circ}C) + 150)/7.99 \qquad \textbf{(6.13)}$$

The temperature dependence is rather modest, a 15% change over a temperature range of 35°C.

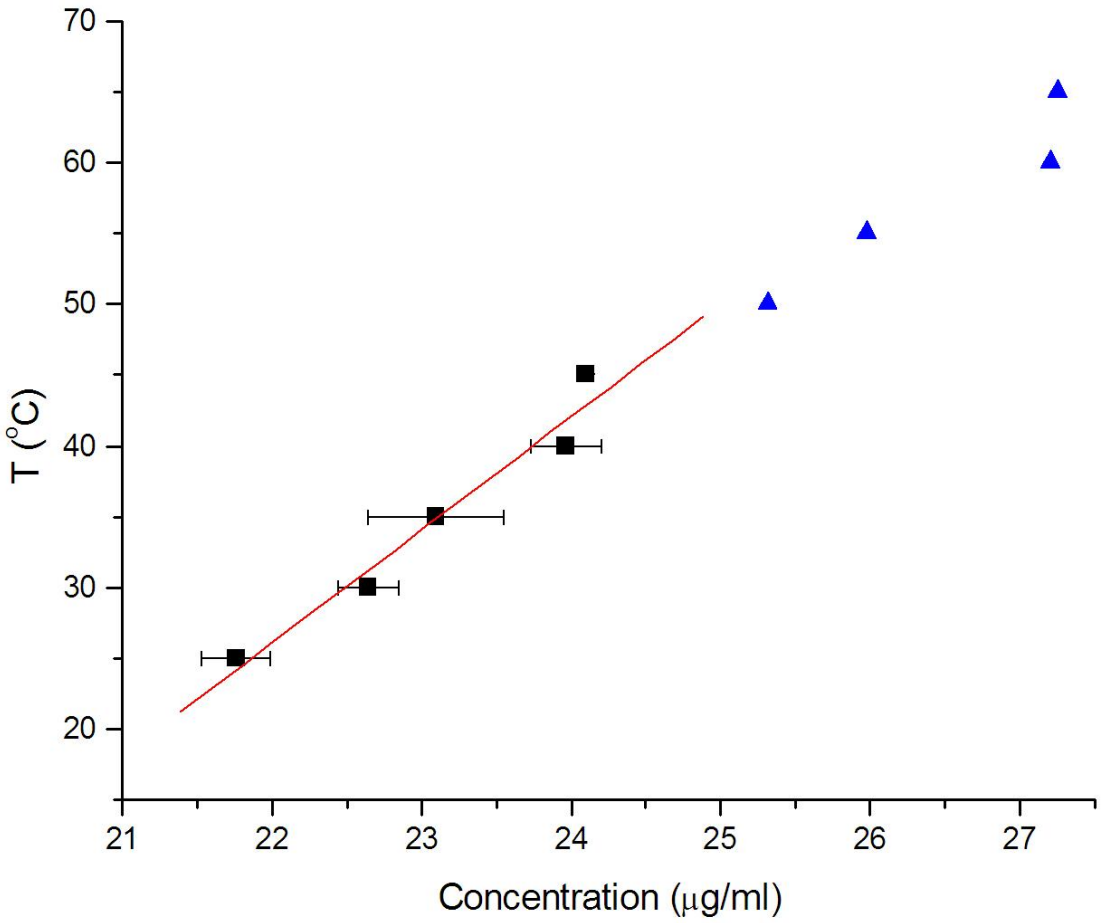

Figure 6.4 Phase diagram of $AuC_{12}SH$ nanoparticles in 4% t-butyl toluene + 96% 2-butanone. The data marked by square points were measured after 15-minute centrifuging, linearly fitted with the straight line. The triangle points were measured, without centrifuging, 30 minutes after the quench and may have less accuracy.

6.3.2 Gold Nanoparticles in Mixtures of Toluene and 2-butanone

Similar experiments were done with $AuC_{12}SH$, $AuC_{10}SH$ and AuC_8SH in mixture of toluene and 2-butanone. Also we varied the ratio of toluene and 2-butanone as the solvents. The typical UV-Vis absorbance spectra of gold nanoparticles ligated with decanethiol dispersed in 60% 2-butanone + 40% toluene was plotted in Figure 6.5. The peak absorbances were converted to concentrations by using the calibration equation (6.3).

Figure 6.6 shows the phase diagrams of $AuC_{12}SH$ in mixtures of toluene and 2-butanone. Figure 6.7 shows the phase diagrams of $AuC_{10}SH$ in mixtures of toluene and 2-butanone. And Figure 6.8 shows the phase diagrams of AuC_8SH in mixtures of toluene and 2-butanone. From all the phase diagrams we can deduce that the solubilities of gold nanoparticles are larger with more toluene in the solvent, for the sample gold nanoparticles solutes. That is reasonable and quite obvious because toluene is a good solvent of the gold nanoparticles and 2-butanone is a relative bad solvent.

Figure 6.9 compares the phase diagrams of gold nanoparticles with different ligands in the same solvent. The nanoparticles ligated with dodecanethiol have the largest solubilities. The nanoparticles ligated with decanethiol have the second large solubilities and the nanoparticles ligated with octanethiol have the least solubilities. An easy-understood explanation is the effective interaction potential between two gold nanoparticles becomes stronger as the ligands length is decreased [32]. The nanoparticles ligated with shorter alkyl chains have the greater propensity to aggregate to form supercluster, rather than to disperse in solvent.

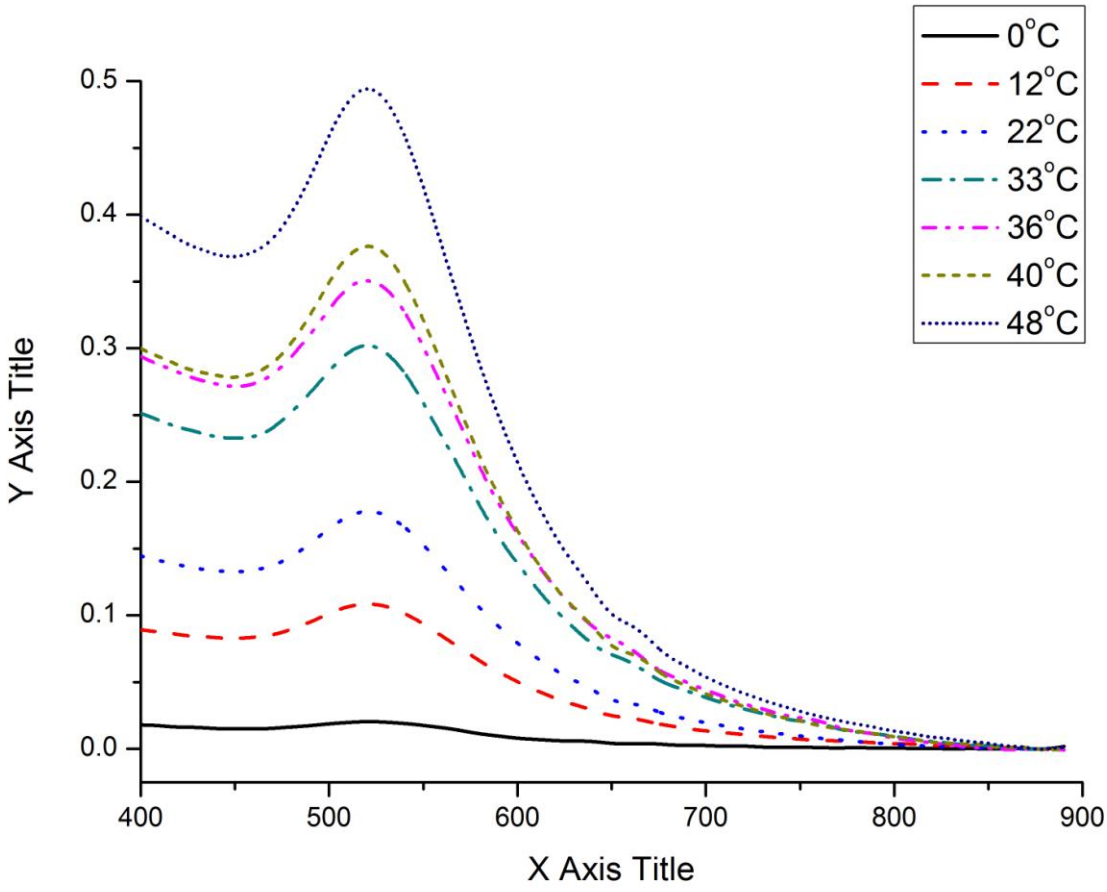

Figure 6.5 UV-Vis absorbance spectra of gold nanoparticles ligated with decanethiol dispersed in 60% 2-butanone + 40% toluene.

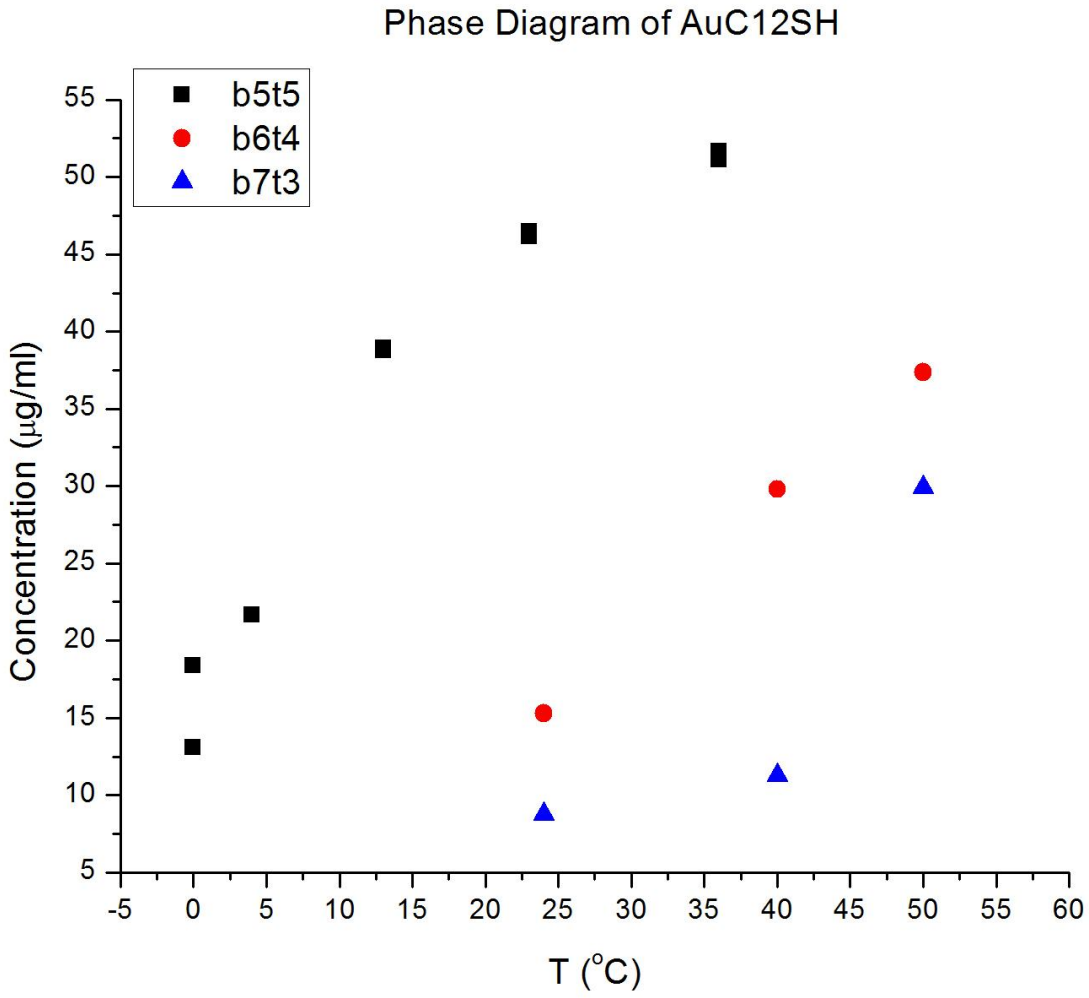

Figure 6.6 Phase diagrams of $AuC_{12}SH$ in mixtures of toluene and 2-butanone. Legends in the figure: b5t5 means 50% 2-butanone + 50% toluene, b6t4 means 60% 2-butanone + 40% toluene, and b7t3 means 70%2-butanone + 30% toluene. The similar legends are also used in subsequent figures.

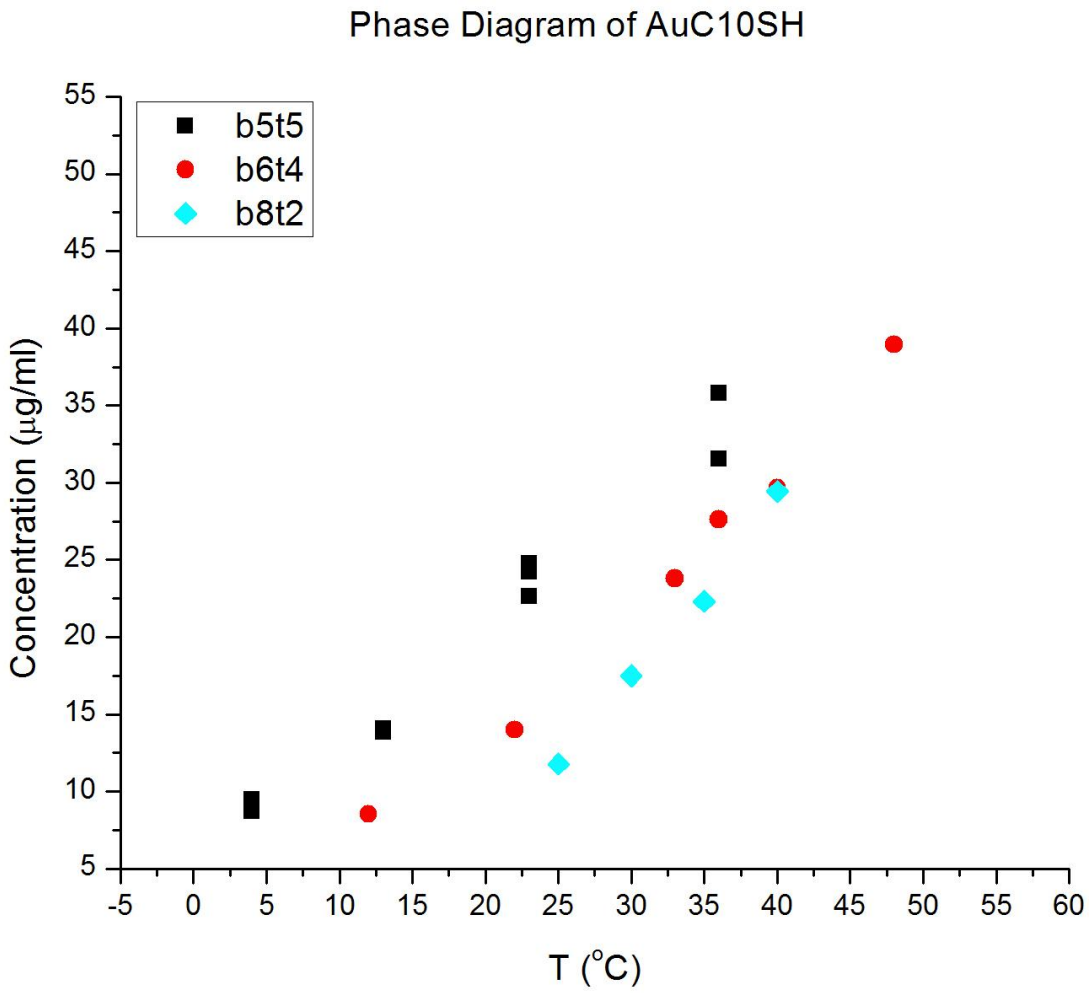

Figure 6.7 Phase diagrams of $AuC_{10}SH$ in mixture of toluene and 2-butanone. See Figure 6.6 for the legends meaning.

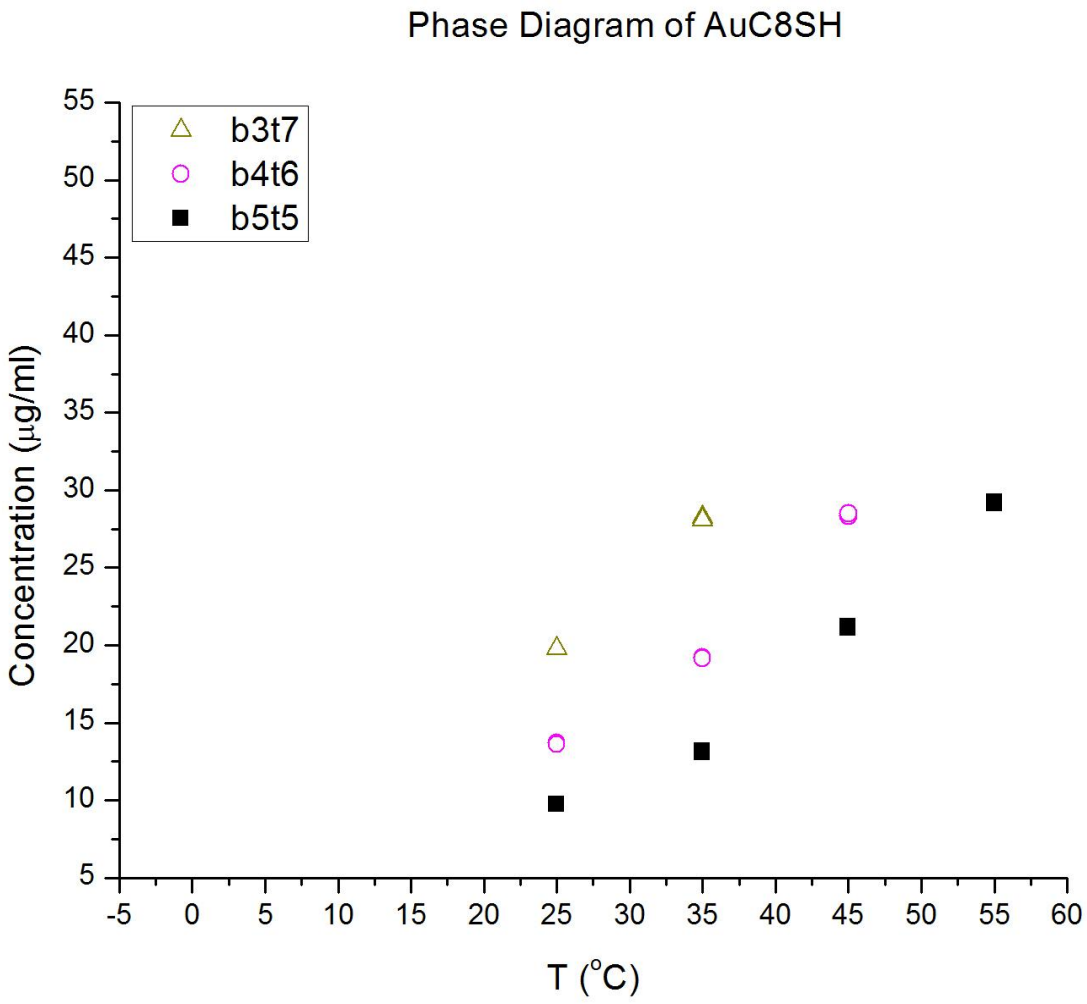

Figure 6.8 Phase diagrams of AuC_8SH in mixture of toluene and 2-butanone. See Figure 6.6 for the legends meaning.

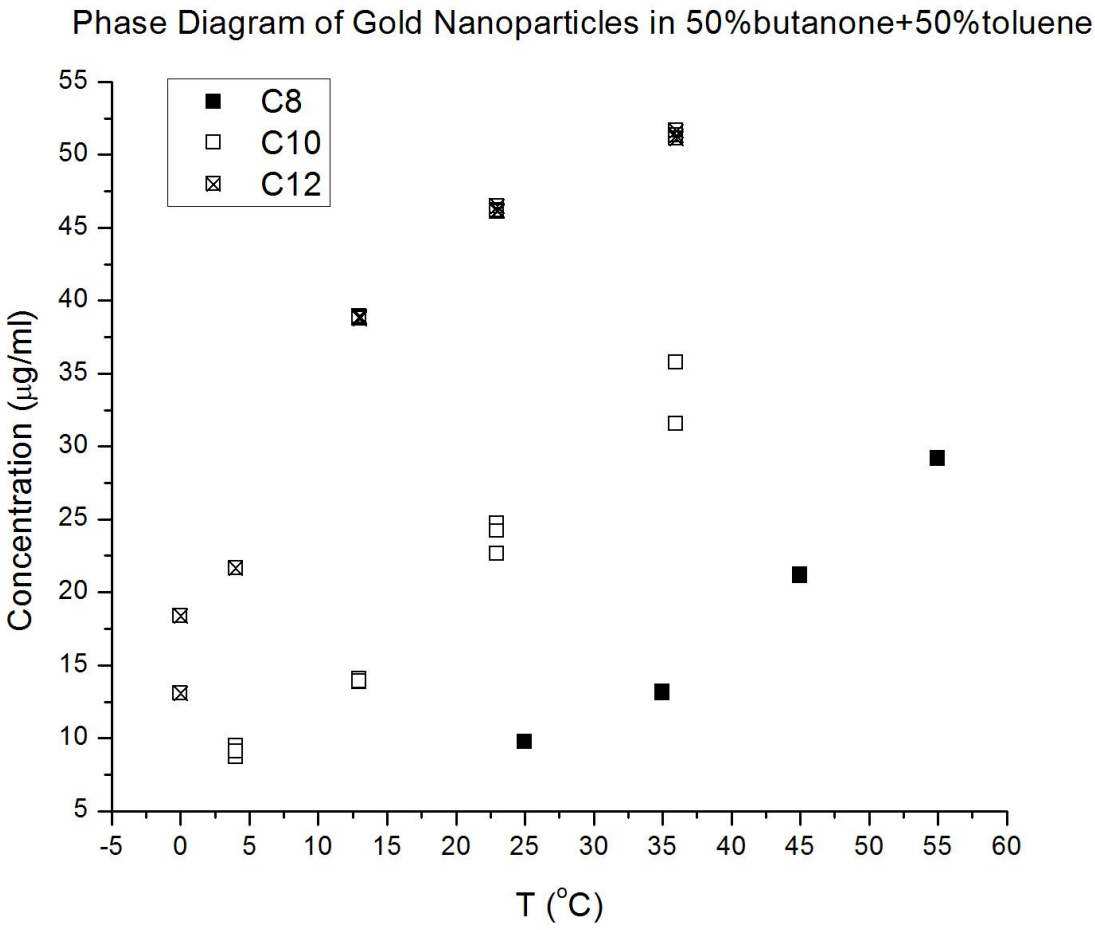

Figure 6.9 Phase diagrams of gold nanoparticles in 50% 2-butanone + 50% toluene. Legends in the figure: C8 means gold nanoparticles ligated with octanethiol, C10 means gold nanoparticles ligated with decanethiol, and C12 means gold nanoparticles ligated with dodecanethiol.

The classical ideal solution theory gives the zero-order relationship between the concentration and the temperature as equation (2.17)

$$-\ln x_1 = \frac{\Delta H_{fus}(T_m)}{RT}\left(1-\frac{T}{T_m}\right) \tag{2.17}$$

where x_1 is the concentration in molar fraction, $\Delta H_{fus}(T_m)$ is the fusion enthalpy of gold superclusters at the melting temperature T_m, R is the molar gas constant $R = 8.31 J \cdot mol^{-1} \cdot K^{-1}$, and T is the temperature in Kelvin.

From above equation we know $-\ln x_1$ is linear proportional to $1/RT$, with $\Delta H_{fus}(T_m)$ as the slope and $\Delta H_{fus}(T_m)/RT_m$ as the intercept. Therefore we can plot the phase diagrams as $-\ln x_1$ vs. $1/RT$ and fit the data with straight line. From the fitting parameters we will have the fusion enthalpy of gold superclusters.

In Figure 6.10, phase diagrams of $AuC_{12}SH$ in mixture of 2-butanone and toluene are plotted as $-\ln x_1$ vs. $1/RT$. The linearly fitted mathematical relationships from experimental data are listed in Table 6.1.

In Figure 6.11, phase diagrams of $AuC_{10}SH$ in mixture of 2-butanone and toluene are plotted as $-\ln x_1$ vs. $1/RT$. The linearly fitted mathematical relationships from experimental data are listed in Table 6.2.

In Figure 6.12, phase diagrams of AuC_8SH in mixture of 2-butanone and toluene are plotted as $-\ln x_1$ vs. $1/RT$. The linearly fitted mathematical relationships from experimental data are listed in Table 6.3.

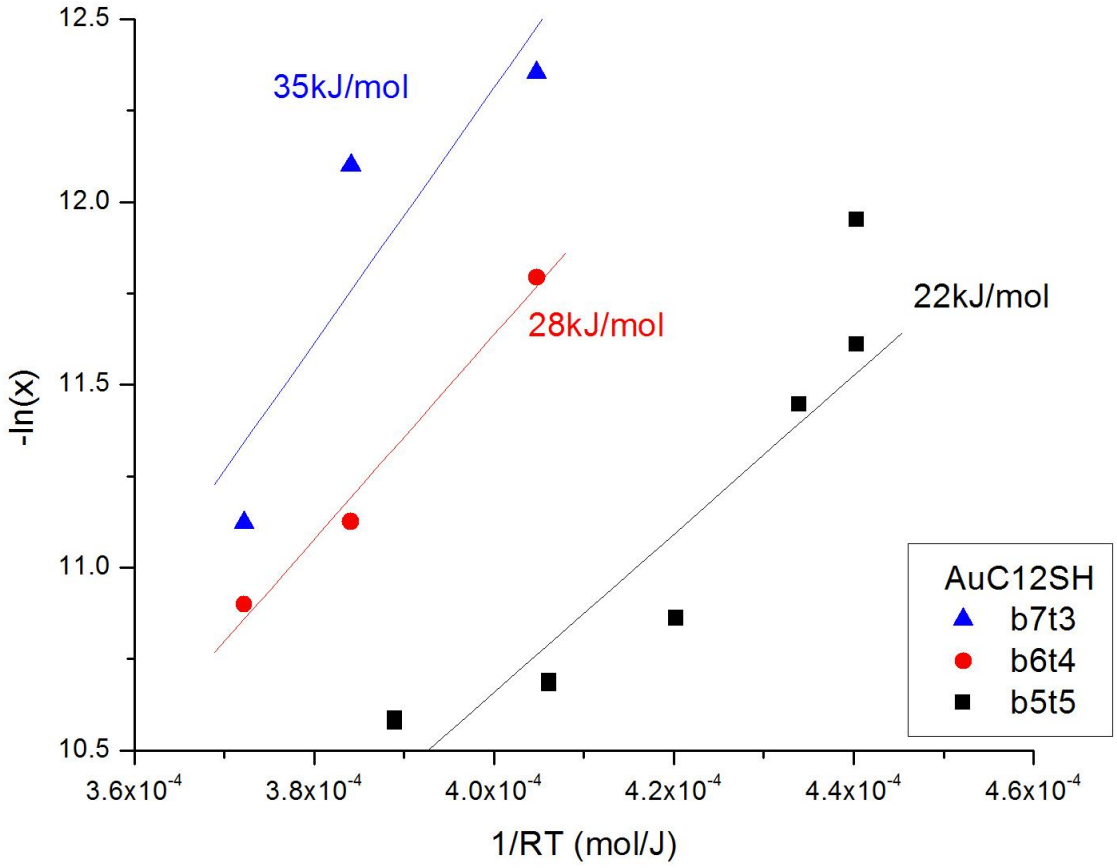

Figure 6.10 Phase diagrams of $AuC_{12}SH$ in mixture of toluene and 2-butanone. See Figure 6.6 for the legends meaning.

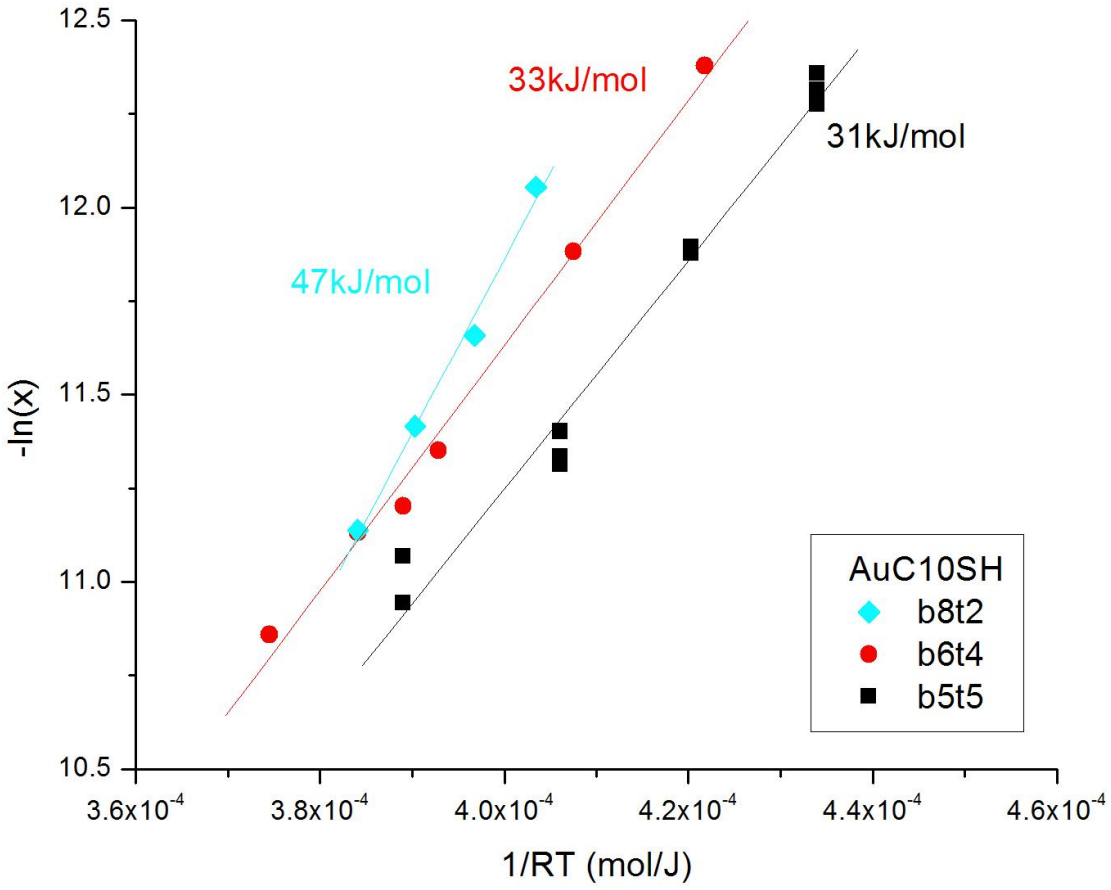

Figure 6.11 Phase diagrams of $AuC_{10}SH$ in mixture of toluene and 2-butanone. See Figure 6.6 for the legends meaning.

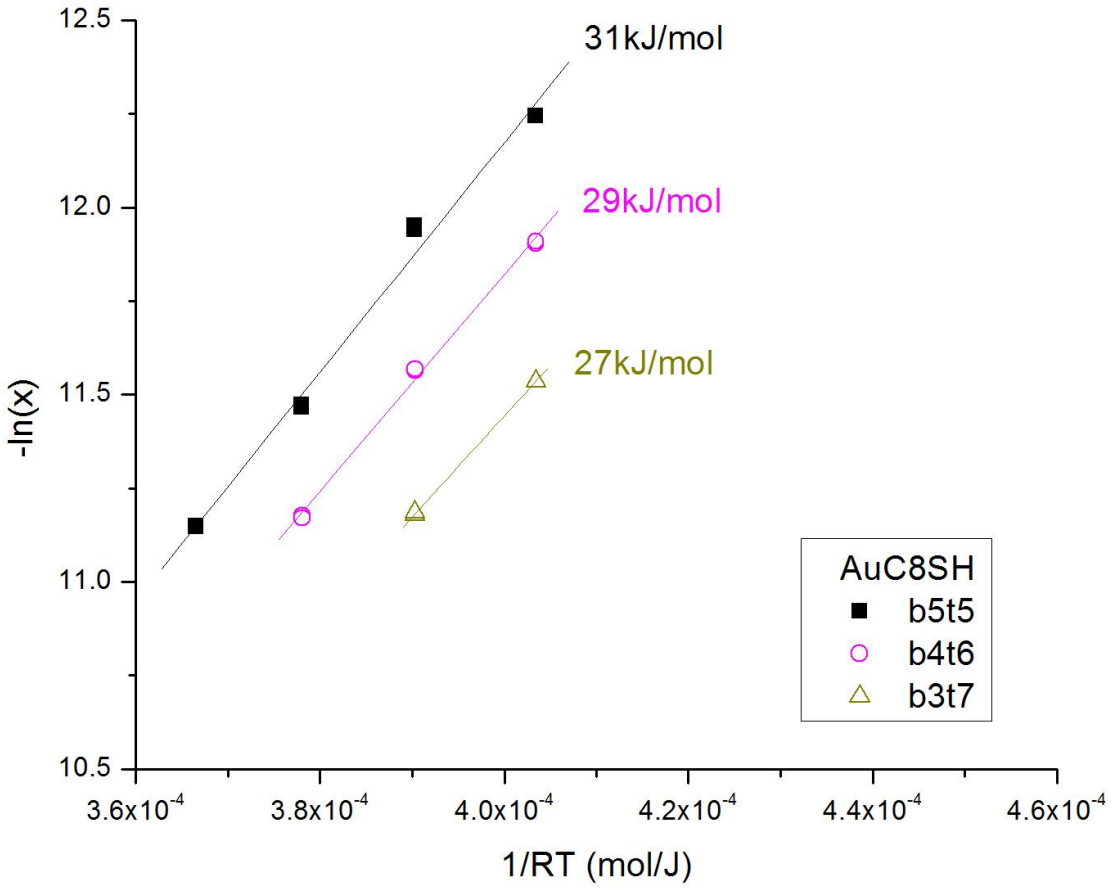

Figure 6.12 Phase diagrams of AuC_8SH in mixture of toluene and 2-butanone. See Figure 6.6 for the legends meaning.

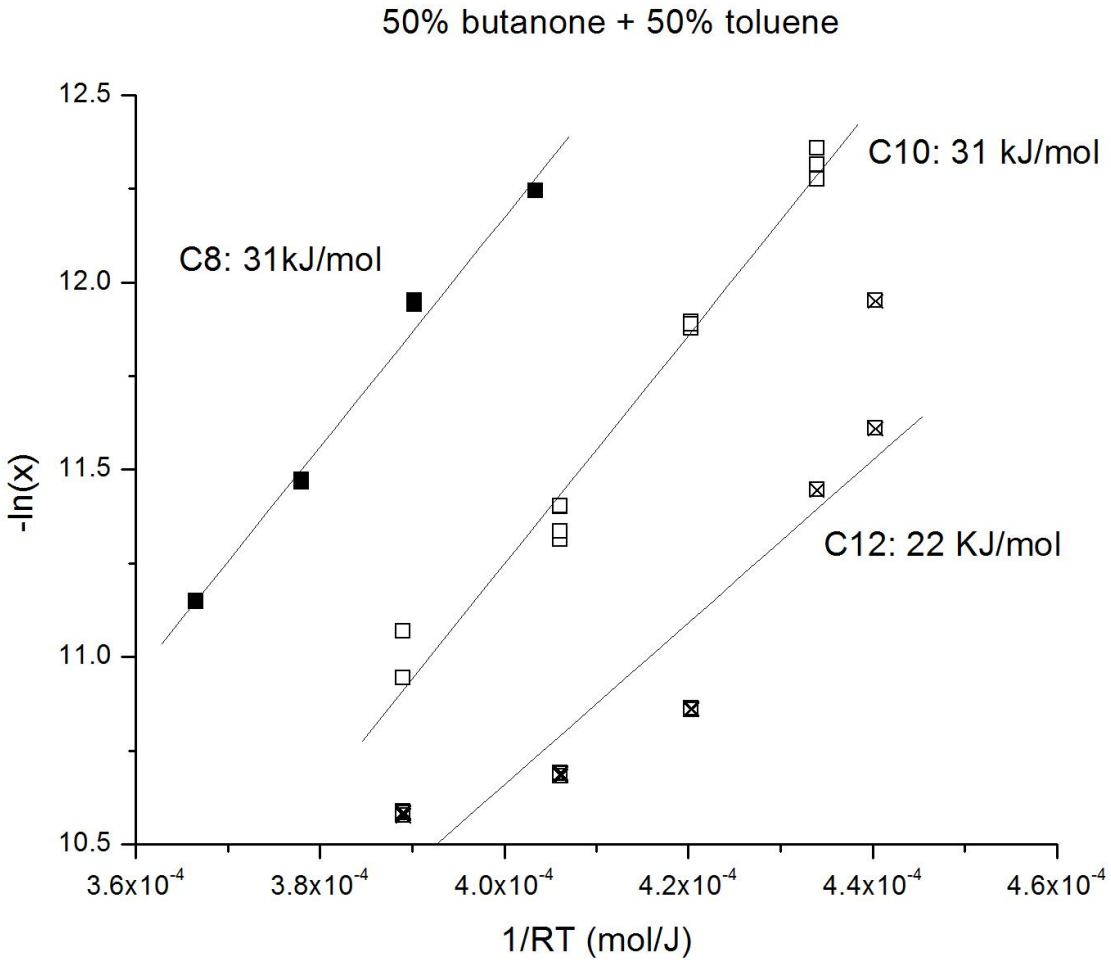

Figure 6.13 Phase diagrams of gold nanoparticles in 50% 2-butanone + 50% toluene. Legends in the figure: C8 means gold nanoparticles ligated with octanethiol, C10 means gold nanoparticles ligated with decanethiol, and C12 means gold nanoparticles ligated with dodecanethiol.

Table 6.1 Mathematical relationships of concentration and temperature of gold nanoparticles ligated with dodecanethiol in mixture of 2-butanone and toluene

Solvent	$-\ln x_1$ **vs.** $1/RT$
70%butanone+30%toluene	$-\ln x = (35 \pm 18) kJ/mol \frac{1}{RT} - (1.7 \pm 7.1)$
60%butanone+40%toluene	$-\ln x = (28 \pm 3.5) kJ/mol \frac{1}{RT} + (0.44 \pm 1.3)$
50%butanone+50%toluene	$-\ln x = (22 \pm 3.4) kJ/mol \frac{1}{RT} + (2.0 \pm 1.4)$

Table 6.2 Mathematical relationships of concentration and temperature of gold nanoparticles ligated with decanethiol in mixture of 2-butanone and toluene

Solvent	$-\ln x_1$ **vs.** $1/RT$
80%butanone+20%toluene	$-\ln x = (46 \pm 3.2) kJ/mol \frac{1}{RT} - (6.7 \pm 1.3)$
60%butanone+40%toluene	$-\ln x = (33 \pm 1.5 kJ/mol \frac{1}{RT} - (1.5 \pm 0.58)$
50%butanone+50%toluene	$-\ln x = (31 \pm 1.4) kJ/mol \frac{1}{RT} - (0.97 \pm 0.58)$

Table 6.3 Mathematical relationships of concentration and temperature of gold nanoparticles ligated with octanethiol in mixture of 2-butanone and toluene

Solvent	$-\ln x_1$ **vs.** $1/RT$
50%butanone+50%toluene	$-\ln x = (31 \pm 1.3) kJ/mol \frac{1}{RT} - (0.067 \pm 0.48)$
40%butanone+60%toluene	$-\ln x = (29 \pm 0.88) kJ/mol \frac{1}{RT} + (0.27 \pm 0.34)$
30%butanone+70%toluene	$-\ln x = (27 \pm 0.23) kJ/mol \frac{1}{RT} + (0.66 \pm 0.091)$

Assuming the gold nanoparticles colloidal solutions are ideal solutions, from the slopes of the fitted line in the phase diagrams, we obtain the fusion enthalpies of gold nanoparticle superclusters as listed in Table 6.4. The fusion enthalpies have systematic but modest changes with the solvent and the ligands. The fusion enthalpy became larger when the ligand chains became shorter. That is consistent with the fact that the interaction potential of the gold nanoparticles with shorter ligand chains is stronger.

The intercepts of the fitted line in the phase diagrams give the term $-\Delta H_{fus}(T_m)/RT_m$, which should be negative because both the fusion enthalpy and the melting temperature have positive values. From the intercepts we can find out the melting temperatures of the superclusters. However there are some positive intercepts in Table 6.1, Table 6.2 and Table 6.3. That means the intercepts we obtained could have large experimental error. But we still list the melting temperatures of superclusters calculated from those negative intercepts, as Table 6.5.

The fusion enthalpy increases when the ratio of 2-butanone is increased and the ratio of toluene is decreased. That suggests that our gold nanoparticles colloidal solutions are not so "ideal" because the fusion enthalpy of same solute should be independent of the solvent if the solutions are ideal solution. In section 2.2.3, we discussed the regular solution model as a good approximation of real solution. The regular solution gives the solubility equation in equation (2.22).

$$-\ln x_1 = \frac{\Delta H_{fus}(T_m)}{RT}\left(1-\frac{T}{T_m}\right)+\frac{V_1(\delta_1-\delta_2)^2}{RT} \qquad (2.22)$$

From the equation we know the slope of our fitted line has two terms, $\Delta H_{fus}(T_m)$ and $V_1(\delta_1 - \delta_2)^2$, where V_1 is the molar volume of the pure liquid solute, δ_1 and δ_2 are the solubility parameters of solute and solvent. The second term can not be ignored for regular solutions. The change of the solvents in regular solution affect the solubility parameter δ_2, then the slopes of the relationship of concentrations and temperatures change. The molar volume of the pure liquid solute V_1 and the solubility parameters of solute δ_1 are needed for further analysis.

Table 6.4 Fusion enthalpies of gold nanoparticle superclusters with different ligands (in kJ/mol)

	AuC_8SH	$AuC_{10}SH$	$AuC_{12}SH$
80%butanone+20%toluene		47 ± 3.2	
70%butanone+30%toluene			35 ± 18
60%butanone+40%toluene		33 ± 1.5	28 ± 3.5
50%butanone+50%toluene	31 ± 1.3	31 ± 1.4	22 ± 3.4
40%butanone+60%toluene	29 ± 0.88		
30%butanone+70%toluene	27 ± 0.23		

Table 6.5 Melting temperatures of gold nanoparticle superclusters with different ligands (in Kelvin).

	AuC_8SH	$AuC_{10}SH$	$AuC_{12}SH$
80%butanone+20%toluene		830	
70%butanone+30%toluene			2500
60%butanone+40%toluene		2600	
50%butanone+50%toluene	56000	3800	

The fusion enthalpy of a solid material is related to the interaction potential between the particles in the solid. A good example is the inert gases with the well known Lennard-Jones Potential

$$U(R) = 4\varepsilon\left[\left(\frac{\sigma}{R}\right)^{12} - \left(\frac{\sigma}{R}\right)^{6}\right] \qquad \textbf{(6.14)}$$

The potential depth parameter is $\varepsilon = 167\times10^{-16} erg$ for Ar and $\varepsilon = 320\times10^{-16} erg$ for Xe [55]. The fusion enthalpy is $\Delta H_{fus} = 1.18 kJ/mol$ for Ar crystal and $\Delta H_{fus} = 2.27 kJ/mol$ for Xe crystal [56]. From those data we get the relation between the fusion enthalpy and the interaction potential for inert gas is

$$\Delta H_{fus} \approx 1.18 N_A \varepsilon \qquad \textbf{(6.15)}$$

where N_A is Avogadro constant.

If we assume the interaction potential between our gold nanoparticles in superclusters is also Lennard-Jones Potential, the interaction potential can be estimated by using equation (6.15). For instance, the fusion enthalpy measured from AuC_8SH in 50%butanone+50%toluene is $31 kJ/mol$, thus the depth of potential well is

$$\varepsilon = \frac{\Delta H_{fus}}{1.18 N_A} = \frac{31 kJ/mol}{1.18\times6.02\times10^{23} mol^{-1}} = 4.3\times10^{-20} J \qquad \textbf{(6.16)}$$

CHAPTER 7 - Nucleation of Gold Nanoparticle Superclusters

7.1 Size Measurement with Dynamic Light Scattering

We discussed the static light scattering and dynamic light scattering theory and the experimental setup before. There are a lot of advantages to study the solubility behavior in solution with light scattering. The sample preparation is relative easy and no special treatment is needed. The measurement process does not interfere with the nature of the sample, so the measurement can reflect the real status of the particles in the solution. And the samples can be used for the subsequent UV-Vis spectroscopy experiments. The running time of dynamic light scattering can be set from few seconds to more than thirty minutes, depending on the properties of the samples. So the dynamic light scattering is an *in situ* and real-time measurement that can monitor the dynamic transition of the system. The measurable size of particles for dynamic light scattering ranges from a few nanometers to a few microns.

We measured the size of our gold nanoparticles ligated with dodecanethiol in toluene with dynamic light scattering method. The results are comparable with the results measured with TEM pictures. The size of gold nanoparticles monomers is so small that the scattered light signal is very weak. Some special techniques were used for those measurements. Firstly, $2mm \times 2mm$ square tubes, instead of the regular 10mm diameter round test tube, were used in the experiment in order to shorten the light path length and reduce the light absorption. The samples, sealed in the square tubes with Parafilm, were then centrifuged for 30 minutes at *800g* RCF to remove the impurity in the solutions. A long running time of the dynamic light scattering, 30 minutes, was set to minimize the electronic noises.

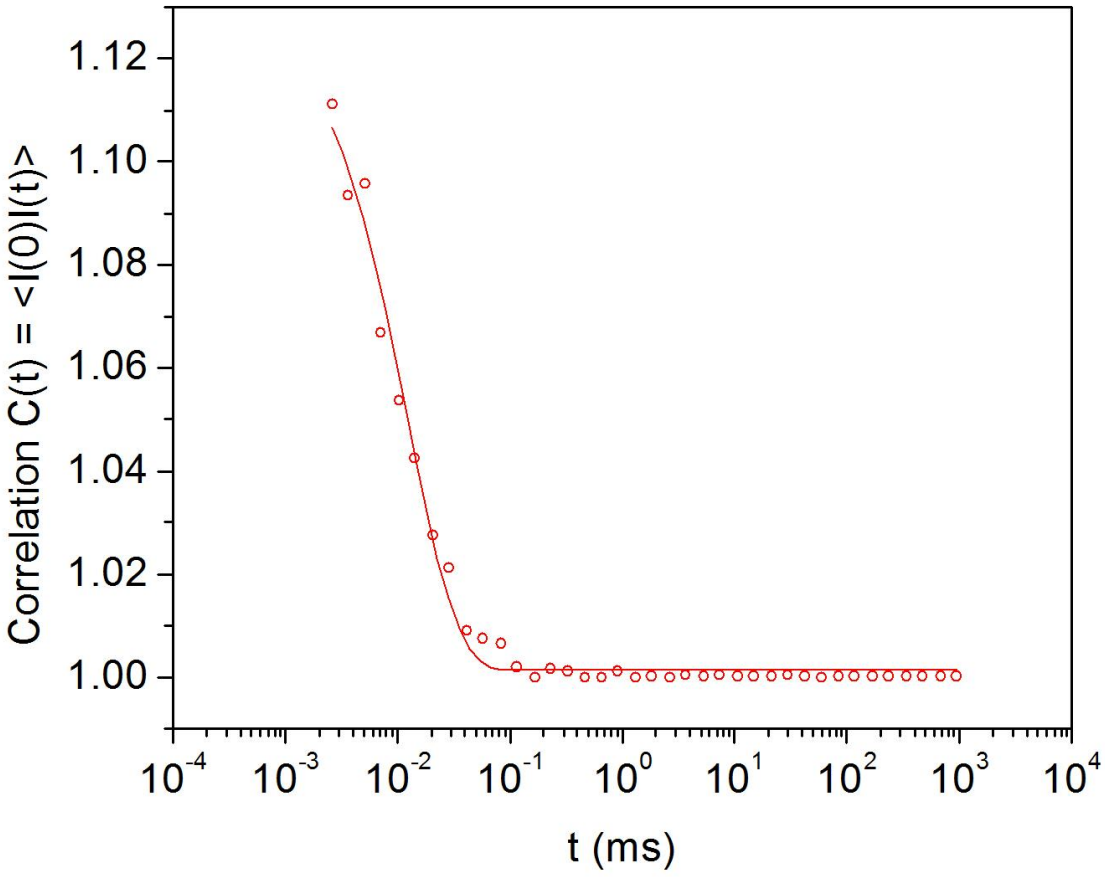

Figure 7.1 Correlation function obtained from gold nanoparticles ligated with dodecanethiol in toluene at 22°C.

Figure 7.1 shows the correlation function of $AuC_{12}SH$ monomers in toluene. Fitting the correlation function with the exponential decay equation (4.27) gave the correlation time $\tau_c = 0.0127ms$. The radius calculated with that correlation time is $a = 4.2nm$. This is in very good agreement with the TEM value when twice the ligand length is added to gold core size $4.9 \pm 0.5nm$, *viz.* $8.3 \pm 0.5nm$.

The experimental procedures for the solubility phase behaviors of gold nanoparticles in mixtures of toluene (or t-butyl toluene) and 2-butanone were described in section 6.2. Once the sample was quenched in the preset lower temperature sample holder, the light scattering measurement was started immediately. Each run of the measurement was set to finish in 10 seconds, which is much shorter than the aggregation time as described blow, in order to make the measurements relatively real-time. The scattered light intensity, the correlation function and the measuring time were recorded in a data file after each run.

7.2 Results and Discussions

Quenches from the one-phase regime into the two-phase regime caused the formation of superclusters of nanoparticles on the order of a few hundred nanometers in size. The scattered light intensity increased dramatically when the gold nanoparticles started to aggregate because of the Tyndall effect. By measuring the size of superclusters and the light intensity, we can study the aggregation kinetics of the nanoparticles and the properties of the superclusters.

7.2.1 Aggregation Kinetics

Nuclei must be formed from the gold nanoparticles in a homogeneous colloidal solution before they can grow to superclusters. In our experiments, the aggregations were often found happened rapidly, which meant the induction time was small enough. To measure the induction time more accurately, we should decrease the temperature of our samples fast enough. For one microliter solution in a 10mm diameter test tube, the characteristic time of the temperature

quench was about 100 seconds. By using a $2mm \times 2mm$ square tube as the sample container, we can reduce the characteristic time to a few seconds.

Figure 7.2 shows the intensities changed with the quench time at different quench temperatures for $AuC_{10}SH$ nanoparticles in a mixture of 60%Butanone+40%Toluene. When a sample was quenched to a much lower temperature, which is a deep quench, the light intensity increased faster then a sample was quenched to a much higher temperature, shallow quench. If we roughly choose the time when the light intensity starts to increase as the nucleation induction time, we can have the data relating the induction time and the quench temperature, as the points plotted in Figure 7.6.

After the nuclei were formed, they stared to grow to form superclusters. The superclusters became larger and larger as the aggregation is proceeding. A straightforward thought might be that the superclusters will keep growing up until they are large enough to settle down to the bottom of the sample container. However, the results of dynamic light scattering measurements showed that the size of the nanoparticle superclusters came to a constant size after a certain growth time and kept that constant size for about one hour, as seen in Figure 7.3. The scattered light intensity also stopped evolving on the same time scale to imply that the nanoparticle superclusters were not gravitationally settling. This is supported by the settling velocity calculations using the Stokes drag equation (5.8). Thus the systems were in an equilibrium state of the 5nm size nanoparticle monomer disperse phase and the constant size supercluster phase co-existing.

After several hours, the superclusters in the colloidal solution became larger and more polydisperse. The light intensity also started to decrease which implied the superclusters were gravitationally settling. The dynamic light scattering measurement was becoming difficult because of the polydispersity and the weak signal. Eventually, all the superclusters precipitated at the bottom the sample container.

7.2.2 Supercluster Equilibrium Size

Another interesting phenomenon we can find in Figure 7.3 is that the equilibrium constant size of the superclusters depends on the quench temperature. The superclusters were smaller when the system was quenched to a lower temperature, deep quench, and the superclusters were larger when the system was quenched to a higher temperature, shallow quench. This is a classic result known for both ionic and molecular solutions: deep quenches cause fine precipitates.

In order to study the phenomenon quantitatively, more quench experiments were done and a series of systematic data of the superclusters sizes versus the quench temperatures, as plotted in Figure 7.4.

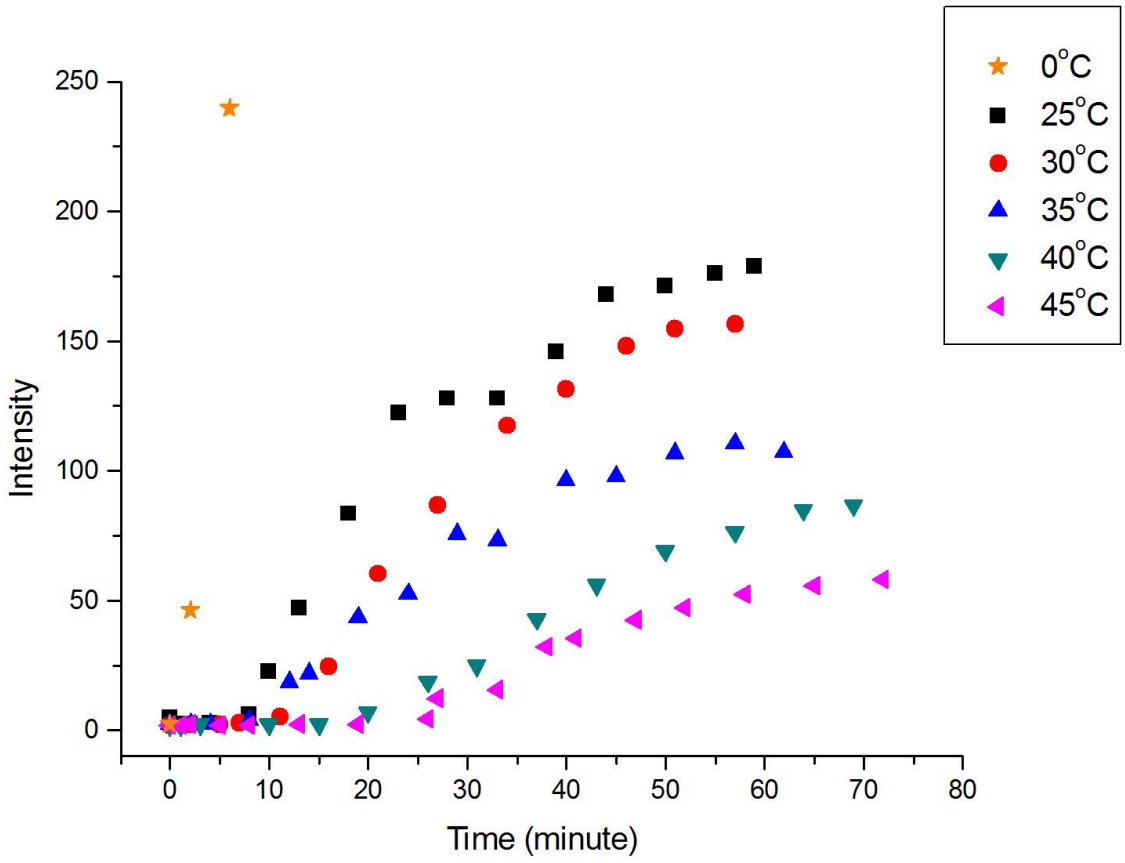

Figure 7.2 Intensity vs. quench time, which shows aggregation induction time of different quench temperatures of $AuC_{10}SH$ in 60%Butanone+40%Toluene.

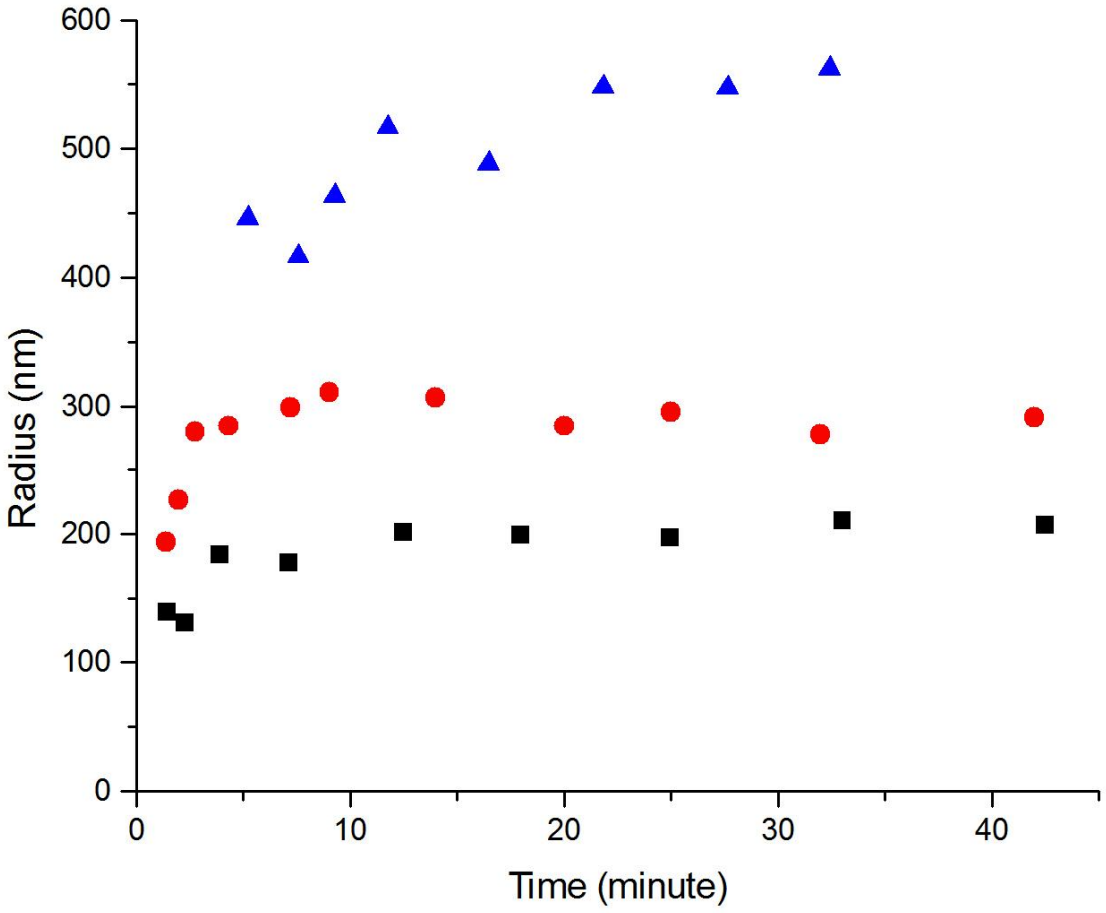

Figure 7.3 Gold nanoparticles ligated with dodecanethiol in 4% t-butyl toluene + 96% 2-butanone were quenched from 65°C (single phase) to 25°C (black square points), 35°C (red circular points) and 45°C (blue triangular points), respectively.

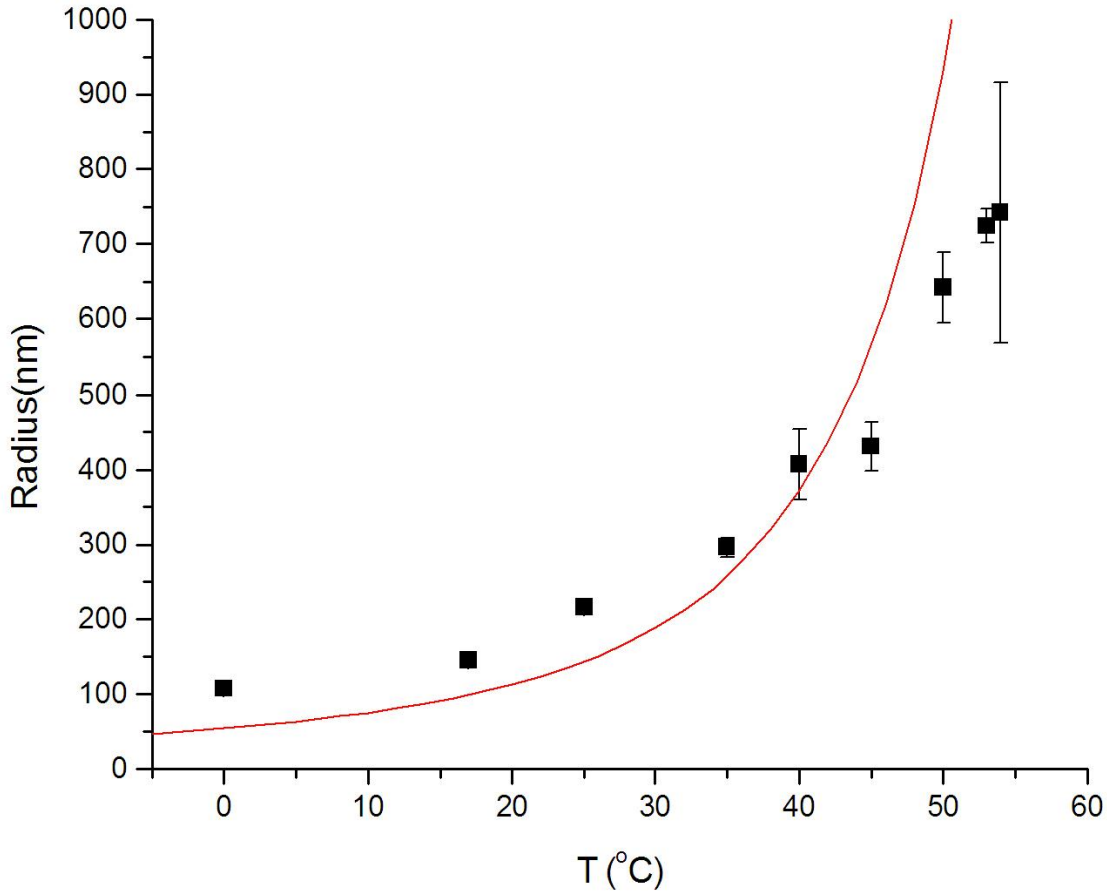

Figure 7.4 The sizes of superclusters formed with 4% t-butyl toluene + 96% 2-butanone at different quench temperatures, quenched from 65°C. The line is the best fit to the nucleation theory described in the text with a single fit variable, the interfacial tension of the solid phase with a value of $0.042\,erg/cm^2$.

7.2.3 Classical Nucleation Theory Explanation

The classical nucleation theory can be used to explain the aggregation kinetics and the supercluster equilibrium size.

The number density of nuclei n_c depends on the critical Gibbs free energy G_c as equation (2.34). With the LaMer-Dinegar model discussed in section 2.3.2, we can have the supercluster equilibrium size computed from the number density of nuclei. Figure 7.5 is a schematic of superclusters growth process explained with the LaMer-Dinegar model. Figure 7.5(A) shows the initial state of the system. The nuclei were formed in the gold nanoparticles monomers. The number density of nuclei determined the volume occupied by each nucleus, which was simply $1/n_c$, plotted as spheres with dash lines in the figure. When one nucleus was growing, only the monomers in that sphere around it would diffuse then attach on the nucleus. Figure 7.5(B) show the monomer and grown supercluster co-existing state. When the superclusters stopped to grow, the concentrations of the left monomers in the colloidal solutions were just the solubilities of the gold nanoparticle monomers in the solvent at this certain temperature. All the excess monomers, the difference between the original solution concentration C and solubility C^*, i.e., $\left(C - C^*\right)$, are exhausted. The superclusters with number density n_c have grown to their maximum size V,

$$V = \frac{4\pi}{3} R^3 = \frac{C - C^*}{n_c} \qquad \textbf{(7.1)}$$

Eventually we can have the radius of the supercluster equilibrium size as in equation (2.44).

$$\frac{4\pi}{3} R_{\max}^3 == v(1 - \frac{1}{s}) \exp\left[\frac{16\pi v^2 \gamma^3}{3k_B^3 T^3 (\ln s)^2} \right] \qquad (2.44)$$

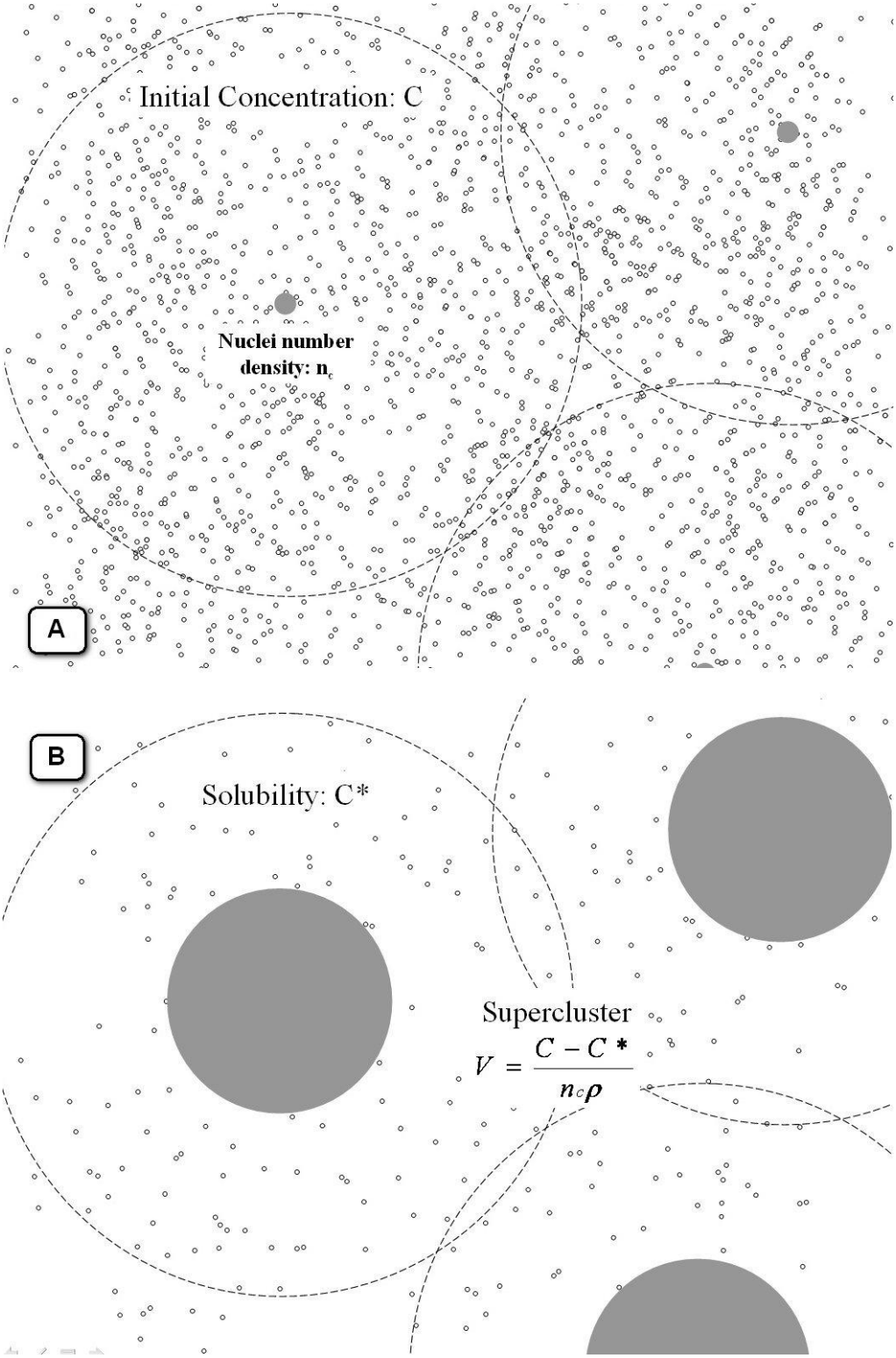

Figure 7.5 A schematic of superclusters growth by using classical nucleation theory and LaMer-Dinegar model. (A) Initial state with nuclei formed. (B) Monomer and grown supercluster co-existing state.

Let us check all the parameters in equation (2.44). For a certain quench temperature *T*, the radius of the supercluster size $R_{\max}$ is measured with dynamic light scattering as plotted in Figure 7.4. The volume of gold nanoparticle monomers *v* can be calculated from the radius of the monomers measured with dynamic light scattering and TEM pictures. The saturation ratio $s = C / C^*$ can be calculated from the initial concentrations *C* and the solubilities C^*, measured with UV-Vis spectroscopy. So the only unknown parameter in equation (2.44) is the interfacial tension γ between the supercluster and the saturated solution. The fitted line of the data in Figure 7.4 with equation (2.44) was plotted as a red curve. The fitting parameter gives the interfacial tension of $0.042 erg / cm^2$.

The fit of nucleation theory to the nanoparticle supercluster size data is successful in two aspects. First, the functionality of decreasing supercluster size with increasing quench depth is obtained. Second, the fit parameter γ represents a new quantity: the interfacial tension of a solid phase of aggregated nanoparticles, most likely a superlattice. From atomic and molecular perspectives, the value we obtain from our fit is quite small, nearly 3 orders of magnitude smaller than those found for atomic and molecular liquids and solids which are typically in the range 10 to 30 *erg/cm*^{2}. However, nanoparticle solids are new materials composed of large nanoparticle ‘‘molecules’’. The surface tension of a hard sphere condensed phase is entirely entropic, and one would expect entropy to be the dominant contribution to the surface tension for the weakly interacting nanoparticle molecules where the interactions are on the order of the thermal energy, *kT* [31]. The entropic surface tension for a close packed FCC lattice is given by [57]

$$\gamma = \frac{0.61 k_B T}{\sigma^2} \qquad \textbf{(7.2)}$$

where σ is the diameter of the ‘‘molecule’’. Above we described the monomer diameter as $8.4 \pm 1.0nm$. Then we find, at room temperature, $\gamma = 0.033 \pm 0.08 erg/cm^2$, which has surprising consistency with the fit value.

7.2.4 Induction Time

From the intensity changes in Figure 7.2, we can roughly plot the induction time vs. quench temperature as the points in Figure 7.6. The classical nucleation theory gives the relation between the induction time and the critical Gibbs free energy in equation (2.36).

$$t_{ind} = B\exp(\Delta G_c / k_B T) = B\exp\left[\frac{16\pi v^2 \gamma^3}{3k^3 T^3 (\ln s)^2}\right] \tag{2.36}$$

If we also consider the relation between the size of supercluster and the critical Gibbs free energy,

$$V = \frac{4\pi}{3} R_{\max}^3 == v(1 - \frac{1}{s})\exp\left[\frac{16\pi v^2 \gamma^3}{3k_B^3 T^3 (\ln s)^2}\right] \tag{2.44}$$

We will have the *B*-factor as

$$B = \frac{v}{V}\left(1 - \frac{C^*}{C}\right) \cdot t_{ind} \tag{7.3}$$

Since all the parameters in equation (7.3) are experimentally measurable, we can calculate the *B*-factor for our gold nanoparticle colloidal solution.

For gold nanoparticles ligated with decanethiol in 60%Butanone+40%Toluene, we measured the solubility C^* (red round data points in Figure 6.7), the nucleation induction time t_{ind} (data points in Figure 7.6) and the size of superclusters in equilibrium *R* (data points in Figure 7.7). The initial gold concentration *C* we used in the quench experiment is $48\mu g/ml$. If we

assume the diameter of that gold core is the same as the diameter of the gold core ligated with dodecanethiol, the diameter of a gold nanoparticle is the diameter of the gold core added with twice the decanethiol ligand length $d = 4.9nm + 2 \times 1.39nm = 7.68nm$. With all the data we got, we calculated and plotted *B* as a function of temperature in Figure 7.8. Its values changed from about *5ms* to almost zero with the quench temperatures increasing.

With the same procedure we used in the $AuC_{12}SH$ with 4% t-butyl toluene + 96% 2-butanone system, we can also fit the data of the supercluster size in equilibrium in the $AuC_{10}SH$ with 60%Butanone+40%Toluene system through equation (2.44). Once we obtain the fit parameter, interfacial tension of $AuC_{10}SH$ superclusters in 60%Butanone+40%Toluene, we can use it in equation (2.36) to fit the induction time data. The fit parameter we obtained is $0.06erg/cm^2$, which is still small. However, both the size fit curve and the induction time fit curve were not matching the experiment data well, shown as the red solid curves in Figure 7.6 and Figure 7.7. The reason of that is still unknown. Further experiments and theory work can be done to study the nucleation kinetics in our colloidal solution.

7.3 Recommendations for Future Work

The grown superclusters in the colloidal solution are not stable. They will keep aggregating in several hours and precipitate at the bottom of the container eventually. There are studies of the nucleation growth showed a two-stage growth process in formation of monodisperse colloids [58]. The study of kinetics of the second step of superclusters aggregation could be interesting.

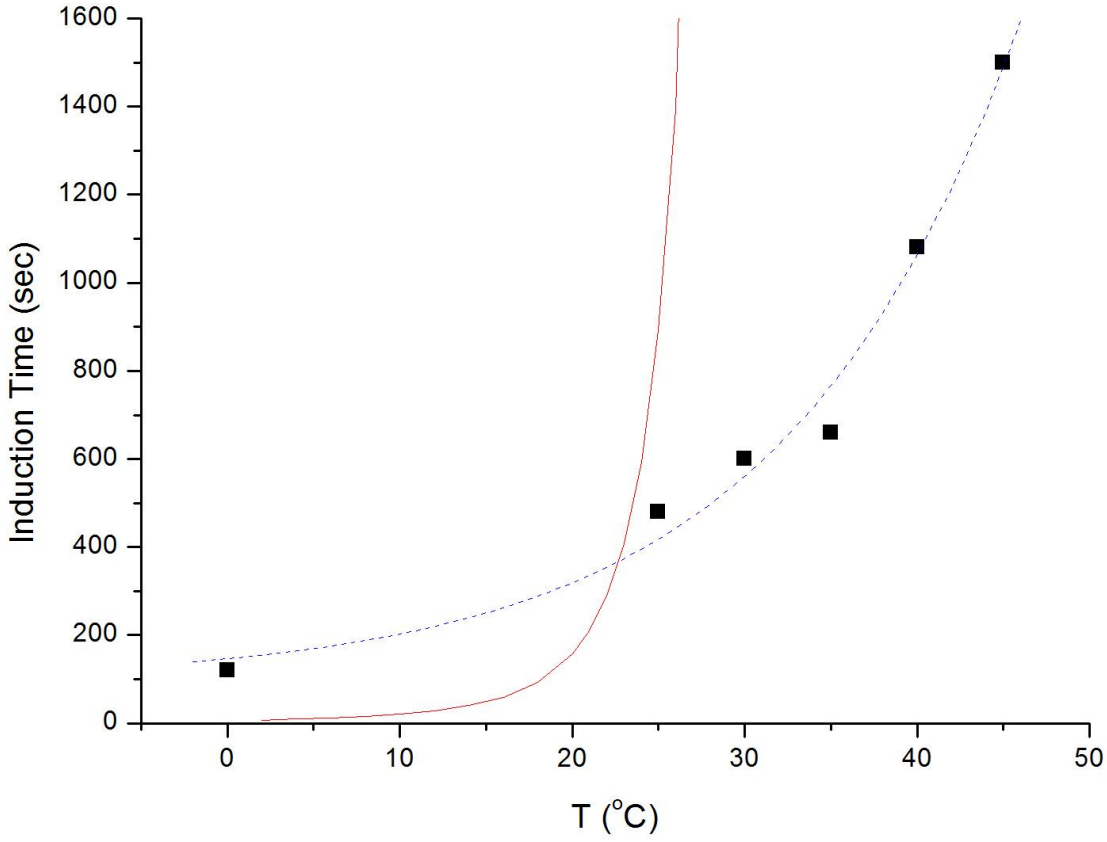

Figure 7.6 Induction time vs. quench temperature of $AuC_{10}SH$ in 60%Butanone+40%Toluene. The blue dash line is the best fitted exponential growth curve of the experimental data. The red solid curve is the best fit to the classical nucleation theory.

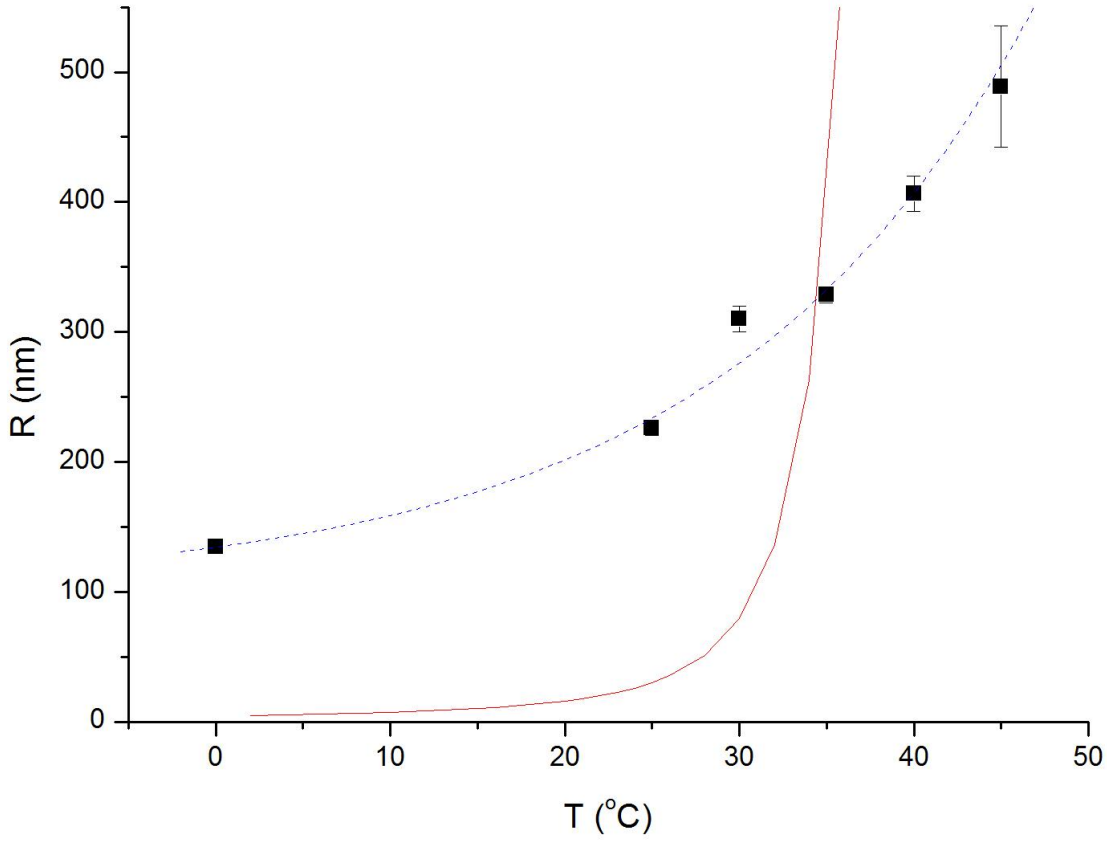

Figure 7.7 Radius of the superclusters vs. quench temperature of $AuC_{10}SH$ in 60%Butanone+ 40%Toluene. The blue dash line is the best fitted exponential growth curve of the experimental data. The red solid curve is the best fit to the classical nucleation theory. The fit paramseter gives the interfacial tension of the solid phase with a value of $0.06\, erg / cm^2$.

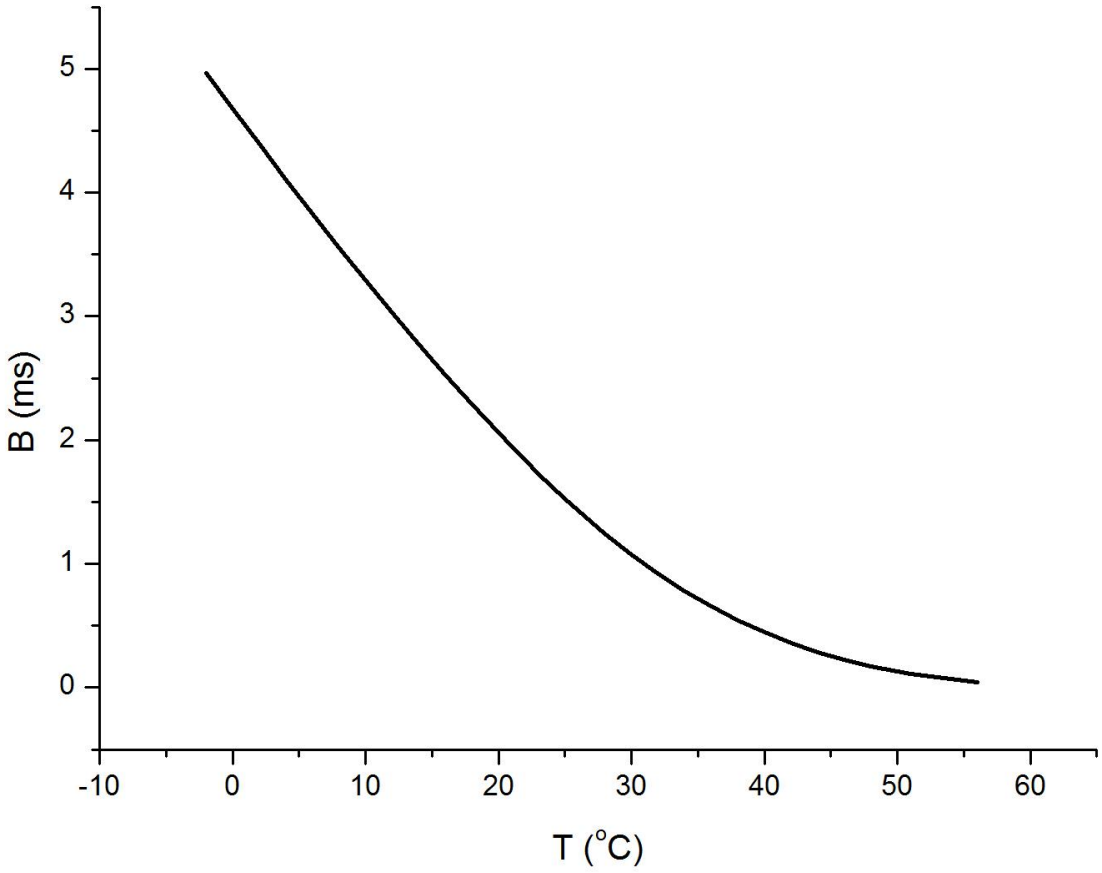

Figure 7.8 *B*-factor in the nucleation induction time of $AuC_{10}SH$ in 60%Butanone+40%Toluene.

CHAPTER 8 - Conclusion

Here we give a conclusion of our study on the solubility phase transition behavior of gold nanoparticles in colloidal solution.

Gold nanoparticles in colloidal solution had been synthesized with inverse micelle method and solvated metal atom dispersion method. The gold particles were polydisperse before they were digestive ripened. Digestive ripening is a term of the refinement process of nanoparticles in colloidal solution through heating. After the digestive ripening, nearly monodisperse gold nanoparticles were obtained. The gold nanoparticles are usually surface ligated with alkyl chains, which could be dodecanethiol, decanethiol, or octanethiol. These ligands cause colloidal solutions of the nanoparticles to be stable against irreversible aggregation. Gold nanoparticles dispersed in toluene or t-butyl toluene like large molecules at room temperature. The gold nanoparticles have a strong tendency toward superlattice formation due to the uniformity in size and shape.

The gold nanoparticle colloidal solution displays a reversible temperature dependent solubility phase transition behavior. The nanoparticles dispersed in mixtures of toluene (or t-butyl toluene) and 2-butanone at high temperature would aggregate to form superclusters when they were quenched to a lower temperature blow the phase boundary. The monomers-superclusters co-existing phase would change back to the dispersed phase when the system temperature increased across the phase boundary.

The solubility curves, i.e., the phase diagrams were obtained with UV-Vis spectroscopy concentration measurements. The solubility of gold nanoparticles varied with the ligands lengths on the particles and the polarities of the solvents. With the polarities increasing, the solubilities were getting smaller. That is consistent with the well-known "like dissolves like" guide. The shorter the ligands lengths were, the smaller the solubilities were. That can be explained with that the nanoparticles with shorter ligand chains have the stronger interaction potential. The particles tends to aggregate rather than to disperse in the colloidal solution. Classical ideal solution theory gave the fusion enthalpies of the superclusters from the solubility curves. However, more works are needed to be done because our colloidal solutions are not so "ideal". Regular solution theory could be a good approximation to be used.

Temperature quenches from the one-phase to the two-phase regime described by the solubility curve yields superclusters of the nanoparticle solid phase. The nucleation induction times were measured with different quench temperatures. Once the nuclei were formed, they started to grow from the nanoparticles monomers until their size reached an equilibrium constant size. Classical nucleation theory can describe the size of the nanoparticle superclusters as a function of quench depth. The fitting parameter with the nucleation theory gave a very small but reasonable interfacial tension for the nanoparticle supercluster phase.

In total these results show that the solubility behavior of the quasi-monodisperse nanoparticles in colloidal solutions is similar to the behavior in molecular solutions.

References

[1] R.P. Blakemore, R.B. Frankel, and A.J. Kalmijn, "South-seeking magnetotactic bacteria in the Southern Hemisphere," Nature, vol. 286, 1980, pp. 384-385.

[2] M. Valden, X. Lai, and D.W. Goodman, "Onset of Catalytic Activity of Gold Clusters on Titania with the Appearance of Nonmetallic Properties," Science, vol. 281, Sep. 1998, pp. 1647-1650.

[3] W.P. Halperin, "Quantum size effects in metal particles," Reviews of Modern Physics, vol. 58, Jul. 1986, p. 533.

[4] A.N. Goldstein, C.M. Echer, and A.P. Alivisatos, "Melting in Semiconductor Nanocrystals," Science, vol. 256, Jun. 1992, pp. 1425-1427.

[5] S.L. Lai, J.Y. Guo, V. Petrova, G. Ramanath, and L.H. Allen, "Size-Dependent Melting Properties of Small Tin Particles: Nanocalorimetric Measurements," Physical Review Letters, vol. 77, Jul. 1996, p. 99.

[6] M. Daniel and D. Astruc, "Gold nanoparticles: Assembly, supramolecular chemistry, quantum-size-related properties, and applications toward biology, catalysis, and nanotechnology," Chemical Reviews, vol. 104, Jan. 2004, pp. 293-346.

[7] V.J. Anderson and H.N.W. Lekkerkerker, "Insights into phase transition kinetics from colloid science," Nature, vol. 416, Apr. 2002, pp. 811-815.

[8] X.M. Lin, G.M. Wang, C.M. Sorensen, and K.J. Klabunde, "Formation and dissolution of gold nanocrystal superlattices in a colloidal solution," Journal of Physical Chemistry B, vol. 103, 1999, pp. 5488-5492.

[9] O.C. Compton and F.E. Osterloh, "Evolution of size and shape in the colloidal crystallization of gold nanoparticles," Journal of the American Chemical Society, vol. 129, 2007, pp. 7793-7798.

[10] B. Abecassis, F. Testard, and O. Spalla, "Gold nanoparticle superlattice crystallization probed in situ," Physical Review Letters, vol. 100, 2008, p. 115504.

[11] D.F. Evans and H. Wennerström, The Colloidal Domain: Where Physics, Chemistry, Biology, and Technology Meet, Wiley-VCH, 1999.

[12] J. Goodwin, Colloids and Interfaces with Surfactants and Polymers: An Introduction, Wiley, 2004.

[13] J.H. Hildebrand and R.L. Scott, The Solubility of Nonelectrolytes, Dover Publications, 1964.

[14] J.M. Prausnitz, R.N. Lichtenthaler, and E.G.D. Azevedo, Molecular Thermodynamics of Fluid-Phase Equilibria, Prentice Hall PTR, 1998.

[15] S.I. Sandler, Chemical and Engineering Thermodynamics, Wiley, 1998.

[16] J.H. Hildebrand, "The Term /`Regular Solution/'," Nature, vol. 168, Nov. 1951, p. 868.

[17] J. Hildebrand, J.M. Prausnitz, and R.L. Scott, Regular and Related Solutions: The Solubility of Gases, Liquids, and Solids, Krieger Publishing Company, 1970.

[18] J.W. Mullin, Crystallization, Butterworth-Heinemann, 2001.

[19] F. Meldrum and R. Sear, "Now You See Them," SCIENCE, vol. 322, Dec. 2008, pp. 1802-1803.

[20] D. Gebauer, A. Volkel, and H. Colfen, "Stable Prenucleation Calcium Carbonate Clusters," Science, vol. 322, Dec. 2008, pp. 1819-1822.

[21] A. Kulkarni and C. Zukoski, “Nanoparticle crystal nucleation: Influence of solution conditions,” Langmuir, vol. 18, Apr. 2002, pp. 3090-3099.

[22] V.K. LaMer and R.H. Dinegar, “Theory, Production and Mechanism of Formation of Monodispersed Hydrosols,” JOURNAL OF THE AMERICAN CHEMICAL SOCIETY, vol. 72, 1950, pp. 4847-4854.

[23] X.M. Lin, C.M. Sorensen, and K.J. Klabunde, “Digestive ripening, nanophase segregation and superlattice formation in gold nanocrystal colloids,” Journal of Nanoparticle Research, vol. 2, 2000, pp. 157-164.

[24] S. Stoeva, K.J. Klabunde, C.M. Sorensen, and I. Dragieva, “Gram-scale synthesis of monodisperse gold colloids by the solvated metal atom dispersion method and digestive ripening and their organization into two- and three-dimensional structures,” Journal of the American Chemical Society, vol. 124, 2002, pp. 2305-2311.

[25] A.A. Ponce, A. Smetana, S. Stoeva, K.J. Klabunde, and C.M. Sorensen, “Nanocrystal Superlattices of Copper, Silver and Gold, by Nanomachining,” Nanostructured and Advanced Materials for Applications in Sensor, Optoelectronic and Photovoltaic Technology, 2005, pp. 309-316.

[26] A.B. Smetana, K.J. Klabunde, and C.M. Sorensen, “Synthesis of spherical silver nanoparticles by digestive ripening, stabilization with various agents, and their 3-D and 2-D superlattice formation,” Journal of Colloid and Interface Science, vol. 284, 2005, pp. 521-526.

[27] O.A. El Seoud, “Reversed micelles and water-in-oil microemulsions,” Organized Assemblies in Chemical Analysis, 1994, pp. 1-37.

[28] S.I. Stoeva, "Novel Synthetic Methods, Superlattice Formation and Nanomachining of Gold Nanoparticles," PhD Thesis, Kansas State University, 2003.

[29] Sreeram Cingarapu, Unpublished picture.

[30] S.I. Stoeva, B.L. Prasad, S. Uma, P.K. Stoimenov, V. Zaikovski, C.M. Sorensen, and K.J. Klabunde, "Face-centered cubic and hexagonal closed-packed nanocrystal superlattices of gold nanoparticles prepared by different methods," Journal of Physical Chemistry B, vol. 107, 2003, pp. 7441-7448.

[31] B.L. Prasad, S.I. Stoeva, C.M. Sorensen, and K.J. Klabunde, "Digestive ripening of thiolated gold nanoparticles: The effect of alkyl chain length," Langmuir, vol. 18, 2002, pp. 7515-7520.

[32] S.J. Khan, F. Pierce, C.M. Sorensen, and A. Chakrabarti, "Self-Assembly of Ligated Gold Nanoparticles: Phenomenological Modeling and Computer Simulations†," Langmuir, vol. 25, Dec. 2009, pp. 13861-13868.

[33] C.F. Bohren and D.R. Huffman, Absorption and Scattering of Light by Small Particles, John Wiley&Sons, 1998.

[34] H.C.V.D. Hulst, Light Scattering by Small Particles, Dover Publications, 1981.

[35] J.D. Jackson, Classical Electrodynamics Third Edition, Wiley, 1998.

[36] E. Hecht, Optics, Addison Wesley, 2001.

[37] R. Finsy, "Particle sizing by quasi-elastic light scattering," Advances in colloid and interface science, vol. 52, 1994, pp. 79–143.

[38] B.J. Berne and R. Pecora, Dynamic light scattering: with applications to chemistry, biology, and physics, Dover Publications, 2000.

[39] W. Brown, Dynamic light scattering: the method and some applications, Clarendon Press Oxford, 1993.

[40] K. Schatzel, "Single-photon correlation techniques," Dynamic Light Scattering: The method and some applications, 1993, p. 76.

[41] D.E. Koppel, "Analysis of macromolecular polydispersity in intensity correlation spectroscopy: the method of cumulants," The Journal of Chemical Physics, vol. 57, 1972, p. 4814.

[42] X.M. Lin, G.M. Wang, C.M. Sorensen, and K.J. Klabunde, "Thermal blooming effect on particle sizing with photon correlation spectroscopy," Applied Optics, vol. 38, 1999, pp. 1884-1886.

[43] Z.L. Wang, Characterization of Nanophase Materials, Wiley-VCH, 2000.

[44] M. Faraday, "The Bakerian Lecture: Experimental Relations of Gold (and Other Metals) to Light," Philosophical Transactions of the Royal Society of London, vol. 147, Jan. 1857, pp. 145-181.

[45] G. Mie, "Beiträge zur Optik trüber Medien, speziell kolloidaler Metallösungen," Ann. Phys, vol. 25, 1908, pp. 377–445.

[46] K.L. Kelly, E. Coronado, L.L. Zhao, and G.C. Schatz, "The Optical Properties of Metal Nanoparticles: The Influence of Size, Shape, and Dielectric Environment," The Journal of Physical Chemistry B, vol. 107, Jan. 2003, pp. 668-677.

[47] M.P. Pileni, "Optical properties of nanosized particles dispersed in colloidal solutions or arranged in 2D or 3D superlattices," New Journal of Chemistry, vol. 22, 1998, pp. 693-702.

[48] P. Mulvaney, “Surface plasmon spectroscopy of nanosized metal particles,” Langmuir, vol. 12, Feb. 1996, pp. 788-800.

[49] H. Lamb, Hydrodynamics, Cambridge University Press, 1993.

[50] G.K. Batchelor, An Introduction to Fluid Dynamics, Cambridge University Press, 2000.

[51] S. Ramakrishnan and C.F. Zukoski, “Phase Behavior of Nanoparticle Suspensions,” Dekker Encyclopedia of Nanoscience and Nanotechnology, J.A. Schwarz, C.I. Contescu, and K. Putyera, eds., 2004.

[52] W.B. Russel, D.A. Saville, and W.R. Schowalter, Colloidal Dispersions, Cambridge University Press, 1992.

[53] B.M. Scott, “Calibration curve for absorbance and concentration,” Unpublished data.

[54] W. Mar and M.L. Klein, “Molecular dynamics study of the self-assembled monolayer composed of S(CH2)14CH3 molecules using an all-atoms model,” Langmuir, vol. 10, Jan. 1994, pp. 188-196.

[55] C. Kittel, Introduction to Solid State Physics, Wiley, 2004.

[56] “NIST Chemistry WebBook,” http://webbook.nist.gov/chemistry/.

[57] B.B. Laird, “The solid-liquid interfacial free energy of close-packed metals:,” Journal Of Chemical Physics, vol. 115, 2001, p. 2887.

[58] J. Park, V. Privman, and E. Matijevic, “Model of formation of monodispersed colloids,” Journal of Physical Chemistry B, vol. 105, 2001, pp. 11630-11635.